Spectroscopic Ellipsometry of Iridium Oxides and Iron Pnictides

Von der Fakultät Mathematik und Physik der Universität Stuttgart
zur Erlangung der Würde eines Doktors der Naturwissenschaften
(Dr. rer. nat.) genehmigte Abhandlung

vorgelegt von

Daniel Christopher Pröpper

aus Bad Waldsee

Hauptberichter:	Prof. Dr. Bernhard Keimer
Mitberichter:	Prof. Dr. Tilman Pfau
Tag der mündlichen Prüfung:	30. Juli 2014

Max-Planck-Institut für Festkörperforschung
Stuttgart 2014

One never notices what has been done;
one can only see what remains to be done.
— Marie Curie

Contents

Abbreviations

AFM	Antiferromagnetic
ARPES	Angle resolved photo emission spectroscopy
DFT	Density functional theory
DMFT	Dynamical mean field theory
EDX	energy dispersive x-ray diffraction
FIR	Far infrared
KK	Kramers-Kronig
MIR	Mid infrared
NIR	Near infrared
NMR	Nuclear magnetic resonance
SDW	Spin-density wave
SOC	Spin-orbit coupling
STS	Scanning tunneling spectroscopy
SW	Spectral weight
UV	Ultraviolet

Zusammenfassung

Vielteilchen-Effekte gehören zu den faszinierendsten Erscheinungen der Physik und spielen auf allen Längenskalen eine wichtige Rolle in der Beschreibung physikalischer Zusammenhänge. Die Schwierigkeit hierbei besteht nicht so sehr in der großen Zahl der Teilchen sondern in der Berücksichtigung der relevanten Wechselwirkungen zwischen ihnen. Stark korrelierte Elektronensysteme bieten die Möglichkeit ein solches Zusammenspiel einer ganzen Reihe von Wechselwirkungen zu studieren. Ein kollektives, stark korreliertes Verhalten der Elektronen kann zu neuen, nicht vorhersehbaren Eigenschaften führen.

Überangsmetalloxide haben sich auf diesem Gebiet als besonders ergiebig erwiesen. Hochtemperatur-Supraleitung in Kupferoxiden, kolossaler Magnetwiderstand in Manganaten oder Spin- und Orbitalordnungsphänomene in Vanadium und Titanoxiden sind nur einige Beispiele [1]. Diesen Effekten ist gemein, dass sich die zugrunde liegenden Materialien nahe eines Metall-Isolator-Übergangs befinden. Der sog. Mott-isolierende Zustand lässt sich nicht im Rahmen eines einfachen Modells partiell bzw. vollständig gefüllter elektronischer Bänder erklären – viel mehr die Wechselwirkung zwischen den Elektronen, typischerweise ist hierbei die langreichweitige Coulomb-Abstoßung von besonderer Bedeutung, lokalisiert die Valenzelektronen um die zugehörigen Atomrümpfe und erzeugt so das isolierende Verhalten. Durch die Änderung passender Parameter, wie zum Beispiel Ladungsträgerdotierung oder externer Druck, können diese Systeme vom isolierenden in den metallischen Zustand übergehen und umgekehrt. Der Übergang wird dabei von dem genauen Wechselspiel aller relevanten Wechselwirkungen bestimmt - Korrelationen und Quanten-Fluktuationen bezüglich ihrer Ladungsdichte, Spin-Orientierung, orbitaler Besetzung oder Wechselwirkung mit dem Ionengitter sind nahe des Phasenübergangs von besonderer Bedeutung.

Die oben beschriebenen Materialien basieren auf Übergangsmetallen der vierten Periode, besitzen also $3d$ Valenzelektronen. Diese Systeme sind durch eine starke Coulomb-Wechselwirkung U und geringe elektronische Bandbreiten W charakterisiert. Beim Wechsel von $3d$ über $4d$ hin zu $5d$ Übergangsmetallen nimmt die räumliche Ausdehnung, die Delokalisierung, der Wellenfunktionen der Valenzelektronen stetig zu, was die Wechselwirkungen zwischen den Elektronen insbesondere die Coulomb-Abstoßung durch Abschirmung aufgrund der anderen Elektronen verringert. Durch die starke Zunahme der Kernladungszahl Z hin zu den $5d$ Elementen gewinnt gleichzeitig eine weitere Wechsel-

wirkung an Bedeutung: die Spin-Bahn-Kopplung, die näherungsweise mit Z^4 skaliert. In Iridiumoxid-Verbindungen mit $5d$ Valenzelektronen schließlich erreichen die Energieskalen für die Coulomb-Wechselwirkung U und die Spin-Bahn-Kopplung eine ähnliche Größenordnung und "konkurrieren" daher um den Einfluss auf die Elektronen. Dies führt im Falle der prototypischen Verbindung Sr_2IrO_4 zu einem neuen Grundzustand der durch einen Isospin $J_{\text{eff}} = 1/2$ charakterisiert ist, also einem Zustand, in dem Spin- und Orbitalbeiträge eng verwoben sind [2] Dieser Grundzustand scheint sich auch in anderen Iridiumoxidverbindungen mit Perovskit-artiger Kristallstruktur als hilfreich in der Beschreibung zu erweisen. Spielt sich das ganze nun noch auf einer komplexeren Kristallstruktur, wie zum Beispiel einem honigwaben-ähnlichen Hexagonalgitter, einem Kagomegitter, oder sogar deren Analogae in drei Dimensionen ab, werden neuartige physikalische Eigenschaften erwartet, wie zum Beispiel die Realisierung von Spin-Flüssigkeiten [3]

Eines der faszinierendsten Vielteilchen-Phänomene der Festkörperphysik ist die Supraleitung. Während die metallischen elementaren Supraleiter und einfachen supraleitenden Legierungen durch die mikroskopische Theorie von Bardeen, Cooper und Schrieffer [4] gut erklärt werden, ist der Mechanismus der unkonventionellen Hochtemperatur-Supraleitung, wie sie den Kupferoxid basierten keramischen Stoffen auftritt noch nicht umfassend verstanden, wobei sich aus den jüngsten Forschungsergebnissen ein kohärentes Bild zu festigen scheint. Darin spielen Elektron-Elektron-Wechselwirkungen eine tragende Rolle – vor allem magnetische Spin-Fluktuationen werden in den Kupferoxid basierten Supraleitern als Vermittler der attraktiven Wechselwirkung zwischen den Elektronen, die für die Cooper-Paar-Bindung notwendig ist, favorisiert. Ausgehend von einem Mott-Isolator-Zustand tritt die Hochtemperatur-Supraleitung erst auf, wenn durch Dotierung zusätzliche Ladungsträger eingebracht werden - dies ist aber gleichzeitig mit einem "Aufweichen" der starken Korrelationen verbunden. Erst wenn das Verhältnis stimmt, tritt auch die Supraleitung zu Tage und konsequenter Weise führt eine Überdotierung zu deren Verschwinden.

Ähnliches gilt auch für die kürzlich entdeckte, neue Klasse der Eisenpniktid-Supraleiter. Diese weisen in mancher Hinsicht große Ähnlichkeit mit den Kupraten auf, wie zum Beispiel eine stark anisotrope, lagen-artige Kristallstruktur oder ein sehr ähnliches Dotierungsphasendiagram, in anderen Aspekten jedoch auch signifikante Unterschiede, wie einen metallischen Grundzustand der nichtsupraleitenden Wirtsverbindungen. Die Eisenpniktide schließen nicht nur die Lücke zwischen den Cupraten und den konventionellen Supraleitern, sonder ermöglichen auch einen eigenen, neuen Zugang zur Hochtemperatur-Supraleitung, der nicht auf starke Korrelationen angewiesen ist, sondern schon vor dem Hintergrund moderater Wechselwirkungen entstehen kann. Spin-Fluktuationen gelten aber auch hier als wahrscheinlichster Kandidat für den Cooper-Paar-"Klebstoff".

Die vorliegende Arbeit ist daher Materialien mit reduzierten Elektronen-Korrelationen und der Frage nach der Charakterisierung eben jener Korrelationen gewidmet. Elektron-Elektron-Korrelationen spiegeln sich unmittelbar in den optischen Eigenschaften, der dielektrischen Funktion eines Materials wider. Optische Spektroskopie, insbesondere breitbandige spektroskopische Ellipsometrie, ist daher besonders geeignet den Auswirkungen der Korrelationen nachzugehen. Verbindungen aus den beiden zuvor angesprochenen Materialklassen sind Gegenstand der Untersuchung: Iridiumoxidverbindungen und Eisenpniktide. Nach einer Aufbereitung der relevanten theoretischen und experimentellen Grundlagen der optischen Spektroskopie, im speziellen der spektroskopischen Ellipsometrie, und geeigneter Parametrisierungen der dielektrischen Funktion durch Modell-Funktionen, werden wir anhand der vorhandenen Literatur die grundlegenden Eigenschaften der untersuchten Materialien darstellen um dann unsere experimentellen Ergebnisse zu präsentieren. Als sehr wertvoll für das tiefere Verständnis erweist sich hierbei der Vergleich mit *ab-initio* Dichtefunktional-Rechnungen der Bandstruktur und der daraus abgeleiteten optischen Leitfähigkeit. Dies erlaubt unter anderem eine nähere Bestimmung der Ausgangs- und Endzustände der optischen Übergänge.

Wir beginnen mit den Iridiumoxiden, im Speziellen mit Sr_2IrO_4, dem Prototypen dieser Materialklasse. Wir bestimmen die Komponenten des uniaxial anisotropen dielektrischen Tensors in einem breiten Frequenzbereich von 12 meV bis 6.5 eV. Die dabei entdeckte optische Anisotropie bei Energien unterhalb 2 eV – eine starke Unterdrückung der charakteristischen Interbandübergänge zwischen den t_{2g} Zuständen, die in der dielektrischen Funktion entlang der ab-Ebenen beobachtet werden – ist im Rahmen von Dichtefunktional-Rechnungen mit dem $J_{\text{eff}} = 1/2$ Grundzustand konsistent. Unterhalb der fundamentalen, nahezu isotropen Absorptionskante bei ca. 2 eV finden wir für die ab-Ebenen eine direkte Bandlücke von 0.43 eV und entlang der c-Achse eine indirekte Bandlücke von ca. 0.1 eV. Im Ferninfrarot-Spektralbereich bestimmen wir das ebenso anisotrope Phononenspektrum und dessen Temperaturabhängigkeit mit zehn der nach gruppensymmetrischer Betrachtung und Gitter-Dynamik-Rechnungen zu erwartenden zwölf Moden entlang der ab-Ebenen und vier Moden entlang der c-Achse.

Trotz ihrer Bedeutung in Verbindungen mit $3d$ Valenzelektronen wurde der Elektron-Phonon-Wechselwirkung in $5d$-Verbindungen bisher keine besondere Aufmerksamkeit geschenkt. Wir zeigen, dass in $Na_3Ir_3O_8$ Fano-Resonanzen, die quantenmechanische Interferenz diskreter Übergänge mit einem Anregungskontinuum, auftreten. $Na_3Ir_3O_8$ ist ein semi-metallischer Verwandter der Verbindung $Na_4Ir_3O_8$, das durch geometrische Frustration der magnetischen Momente auf seinem Hyperkagome-Kristallgitter ein vielversprechender Kandidat zur Realisierung einer Spin-Flüssigkeit in drei Dimensionen ist. Ein nicht verschwindendes Dipolmoment der Phononen, wie zum Beispiel zuvor in Sr_2IrO_4

beobachtet, gepaart mit einer starken Asymmetrie der Linienform, legen eine nicht zu vernachlässigende Elektron-Phonon-Wechselwirkung nahe. Durch Vergleich mit *ab-initio* Bandstruktur-Rechnungen lässt sich der Ursprung des Anregungskontinuums, nämlich optische Übergänge zwischen Bändern nahe des Fermi-Niveaus, die eine Rashba-artige, quasi-lineare Dispersion aufweisen und damit stark der Bandstruktur von mehrlagigem Graphen ähneln, bestimmen. Das Fehlen eines Inversionszentrums in der Kristallstruktur im Zusammenhang mit der starken Spin-Bahn-Kopplung erweisen sich als die entscheidenden Faktoren für die Realisierung der Fano-Interferenzen.

Eine präzise Kontrolle der Elektron-Elektron-Korrelationen spielen auch in den Eisenpniktidverbindungen bei der Realisierung der Supraleitung eine entscheidende Rolle. Spin-Fluktuationen, als wahrscheinlichster Vermittler in der Cooper-Paar-Bildung zeigen die Bedeutung der antiferromagnetischen Phase. Ein eingehendes Verständnis des Antiferromagnetismus ist daher eine wichtige Voraussetzung für die Klärung der mikroskopischen Prozesse, die zur Supraleitung führen. Wir verfolgen deshalb zwei Routen: Zuerst untersuchen wir die Auswirkungen der isovalenten Substitution von Eisen ($3d$) durch Ruthenium ($4d$) in $Ba(Fe_{1-x}Ru_x)_2As_2$ über einen weiten Substitutionsbereich ($0 \leq x \leq 0.74$), der alle relevanten Phasen bis hin zur starken Überdotierung abdeckt. Die Entwicklung der optischen Eigenschaften lässt sich in zwei Dotier-Bereiche einteilen, die eine Korrelation mit dem zugrundeliegenden Phasendiagramm zeigen. Während unterhalb der optimalen Dotierung ($x \approx 0.35$) die Plasmafrequenz der Leitungselektronen nahezu konstant ist, steigt diese bei Überdotierung stark an. Ein ähnliches, jedoch gegenläufiges Verhalten zeigt die Polarisierbarkeit, die im wesentlichen durch Interbandübergänge im mittleren Infrarotbereich gegeben ist. Nahezu konstant bis zur optimalen Dotierung, fällt die Polarisierbarkeit bei weiterer Dotierung rapide ab, aber sogar dann bleiben die Werte relativ groß. Die Stärke der Korrelationen lässt sich durch einen Vergleich mit Rechnungen im Rahmen der Dichtefunktional-Theorie in der Lokalen Dichtenäherung abschätzen, wobei letztere die Elektron-Elektron-Wechselwirkungen nicht vollständig berücksichtigen kann. Die so ermittelte relative Stärke der Korrelationen zeigt eine deutliche Abnahme mit steigender Ru Konzentration.

Anstelle des Eisens lässt sich auch das zwischengelagerte Erd-Alkali-Kation ersetzen. In der Serie der Wirtsverbindungen der 122-Familie, AFe_2As_2 (A = Ca, Sr, Ba), hat der zunehmende Ionenradius der Erd-Alkali-Kationen ($4s \rightarrow 5s \rightarrow 6s$) maßgeblichen Einfluss auf die Kristallstruktur und die Wechselwirkung zwischen benachbarten FeAs-Ebenen. Detaillierte Vermessung der Temperaturabhängigkeit der optischen Leitfähigkeit erlaubt es uns jeweils zwei gekoppelte Untersysteme der Spin-Dichtewelle (SDW) zu identifizieren. Die Kopplungsstärke dieser Subsysteme wandelt sich systematisch von schwach im Falle von Ca zu stark in der Ba-Verbindung, wobei die Ca-Verbindung eine deut-

lich stärkere Korrelation innerhalb der einzelnen Subsysteme zeigt, was sich am Verhältnis der optischen SDW-Lücke zur Néel-Temperatur T_N zeigt. Die Temperaturabhängigkeit der Phonon-Parameter schon oberhalb T_N weist auf die viel diskutierte nematische Phase in diesem Bereich des Phasendiagrams hin. Die Unterdrückung zweier Interbandübergänge bei Eintreten der SDW-Instabilität, deren Energien die Energieskala der magnetischen Wechselwirkung deutlich übersteigt, legen eine Umverteilung der Ladungsträger zwischen den verschiedenen Leitungsbändern beim Phasenübergang nahe. Ein Vergleich der experimentell bestimmten und der berechneten Plasmafrequenzen zeigt die systematische Abschwächung der Elektron-Korrelationen von der Ba- hin zur Ca-Verbindung. Unsere Ergebnisse zeigen für $CaFe_2As_2$ mit zwei schwach gekoppelten jedoch überaus metallischen Subsystemen eine herausgehobene Stellung innerhalb der 122-Eisenpniktide auf. Da in allen drei Materialien auf verschiedene Weise Supraleitung induziert werden kann, können unsere Ergebnisse als Grundlage für weitere Erkenntnisse bezüglich der verwandten Supraleiter dienen.

1 Introduction

When many individuals come together new, collective and often unforeseen behavior may arise – be it schools of fish that try to avoid their predators in a spectacular fashion or collective motion or nanometer-scale particles that order in self-organized regular patterns. The actions that individuals take within the group can be completely different, even opposite to what one would expect from the individuals on their own and might be entirely dominated by the influence of the others. Upon changing an external parameter such systems may show interesting ordering phenomena as the units simultaneously change their behavior to a common pattern. Akin to these and many more examples from the living and non-living world, when many electrons are brought close together as realized in a solid material in most cases they cannot be treated as individuals anymore but have to be discussed as an entity and from the interaction of the electrons with each other new, fascinating physical phenomena and novel material properties emerge.

While elemental metals and many insulators are successfully described within the nearly free electron model in terms of partially and fully occupied electronic bands, as put forward by Bloch [5] and Wilson [6], as early as 1937 Peierls [7] pointed out that the unexpected insulating behavior of many transition metal oxides with half-filled d-bands, such as NiO, requires also taking into account electron-electron interactions. He suggested the electrostatic Coulomb repulsion of electrons to be the driving force for localizing the electrons to their respective atomic sites, hindering their ability to move around in the crystal and thus leading to the observed insulating behavior. Based on follow-up work by Mott [8, 9], which was inspired by this conclusion, such insulating phases due to strong Coulomb repulsion are called Mott insulators. Even more intriguing than the Mott insulating phase itself is its transition into a metallic phase when the electronic correlations are weakened, for example by introducing additional charges via doping or applying external pressure to change the inter-atomic distances. In NiO a metal-to-insulator transition has indeed been observed recently at $p \sim 240\,\mathrm{GPa}$ [10]. The strange metallic phase close to such a metal-to-insulator transition may develop new physical properties since fluctuations of spin, charge, and orbital interactions are already strong and compete with each other.

Transition metal oxides, especially those with $3d$ valence electrons, have been in the focus of solid state research for several decades now exactly for these

reasons. New phenomena such as high-temperature superconductivity in the cuprates [11], colossal negative magneto-resistance in the manganites [12] or spin and orbital ordering in vanadates and titanates emerge from the Mott phase on the verge of a metal-to-insulator transition [1] and strong electronic correlations are believed to be at the heart of these effects. All of these phenomena show a high sensitivity to the detailed interplay of different interactions according to their charge, orbital, spin and lattice degrees of freedom and hence are also prone to changes in external control parameters, such as temperature, pressure, magnetic field, or chemical substitution.

One way to directly influence the electronic correlations in a specific compound is to introduce atoms with different valence orbital character. The transition from elements with $3d$ over $4d$ to $5d$ outer orbitals progressively enlarges the spatial extent of the valence states. This delocalization of the valence and/or conduction electrons, the itinerancy, is generally considered to reduce the correlations between the charge carriers accompanied by an increase in the single particle band width W. The new phenomena and properties emerge from the competition of various interactions, typically Coulomb repulsion U, single particle band width W, exchange interactions from virtual hopping, crystal field effects (Jahn-Teller) and, since electrons also carry a spin, magnetic interactions J. The properties of $3d$ transition metal oxides are typically characterized by a small band width W and strong Coulomb repulsion U.

In the realm of $5d$ materials, however, due to their large atomic numbers Z a new player enters the field: spin-orbit coupling (SOC). The entanglement of spin and orbital degrees of freedom follows directly from the relativistic Dirac equation and thus can be considered as one of the few examples where the two domains of quantum physics and Einstein's theory of relativity, which usually find their application on entirely different length scales – the former mostly concerned with atoms and sub-atomic particles, the latter in astronomical affairs – come together on the laboratory table. This new competitor adds another degree of freedom which is particularly interesting, since SOC inherently intermixes the spin and orbital character of the quasi-particles. One consequence of spin-orbit coupling in presence of a gradient in the potential energy V, for example due to the sample surface or a non-centrosymmetric crystal lattice, is the Rashba-Dresselhaus effect. SOC lifts the spin-degeneracy of the electronic bands allowing e.g. for spin-polarized current transport or (quantum) spin-Hall effect [13, 14]. The research field of spintronics makes widely use of this ability to control spins via charge and vice versa and spintronic-based devices are expected to have several advantages compared to their purely electronic counterparts. Thus, systems driven by spin-orbit interactions are not only interesting for fundamental research but also inspiring technological progress.

From the multitude of $5d$ transition metal oxides the iridium-based compounds have come into focus recently. Due to the $5d$ nature of the valence states

the relevant energy scales of an increasing electronic band width, enhanced spin-orbit-coupling and strongly reduced electrostatic Coulomb interaction merge which leads to strong competition between itinerancy and charge localization. A novel Mott-insulating ground state characterized by a $J_{\text{eff}} = 1/2$ isospin has been proposed to be realized in the prime member of the class, Sr_2IrO_4. Its structural and electronic similarities to the first copper-oxide parent compound La_2CuO_4 has raised significant attention for the $5d$ iridium oxides in general. The implications of spin-orbit entanglement becomes even more pronounced when acting on geometrically frustrated crystal lattices – spin liquid ground states in three dimensions or possible realization of the Kitaev model are intensively discussed [3, 15, 16].

One of the most fascinating many-body phenomena in condensed matter physics is superconductivity. Although discovered more than a hundred years ago in elemental metals by Kamerlingh Onnes [17], thought to be resolved phenomenologically by Ginzburg and Landau [18] and shortly after even in a microscopic theory by Bardeen, Cooper and Schrieffer [4, 19] (apart from some minor issues), was brought back to the forefront of research by the discovery of its high-temperature variant in the copper-oxide based materials [11]. Despite tremendous research efforts from both theoretical and experimental points of view the underlying mechanisms active in the Cooper-pairing of electrons are not fully understood yet and new aspects of their phase diagrams, such as spin- and charge-density-wave orders have been discovered recently [20]. The discovery of superconductivity in a new class of iron-pnictide-based superconductors [21] in 2008 came again as a surprise. On one hand these new compounds are advertised as cousins to the cuprates due to several striking similarities as their layered structure and proximity to an antiferromagnetic phase, on the other hand there are several distinct differences, such as a metallic ground state in the non-superconducting parent compounds, showing that high-temperature superconductivity can not only emerge in single band materials with strong electron-electron interactions but also in multi-band materials with reduced correlations. Thus iron-pnictides are believed not only to bridge the gap between conventional (phonon mediated) and high-T_c superconductors but also to offer a new, own route to superconductivity. Although a Mott-transition has not been observed in the main families of iron-pnictide compound – apart from the special case of intrinsically phase separated 245-iron-chalcogenides, where the insulating parent phase is discussed as a Mott-phase – again, the competition of itinerancy and localization is believed to be essential in establishing superconductivity [22].

Already the early example of NiO outlines that a fruitful collaboration of condensed matter theory and experiment is inevitable for unraveling the underlying mechanisms of the novel physical properties in strongly correlated electron systems. Since information on the interplay of the various interactions is directly

encoded in the frequency dependent complex dielectric function $\varepsilon(\omega)$ of a material correlations can directly be assessed by optical spectroscopy[1]. Spectroscopy with electromagnetic waves in a broad energy range from microwaves to deep UV light allows one to examine all essential energy scales of correlations and excitations of single particles as well as collective modes in a solid. Our current understanding of (only weakly correlated) semiconductors and Fermi liquids has been greatly enhanced by the insights gained from optical spectroscopy experiments [23]. Essentially going back to Isaac Newton, who studied the refraction of (sun)light and coined the term "spectrum" in his groundbreaking work *Opticks* for the first time, this technique is arguably one of the oldest in the toolbox of contemporary solid-state spectroscopy, yet still one of the first tools applied in the characterization of new materials. After great efforts by many leading scientists of their times in exploring the nature of light and its interaction with matter, which eventually culminated in a concise description in the form of Maxwell's equations, it was Gustav Kirchhoff and Robert Bunsen at the end of the 19th century who brought the investigation of material properties by probing them with light – in their cases light emitted from salts burned in a gas flame – to a quantitative level when linking spectral lines to the constituent elements. While the most straightforward choice to perform optical spectroscopy is to measure the normal incidence reflectivity of a specific material with respect to a reference[2], the observation of (partial) polarization of light upon reflection at grazing incidence led to the development of so-called spectroscopic ellipsometry initiated by Paul Drude in order to study bulk metals and metallic thin films [24, 25]. Ellipsometry determines both the real and imaginary parts of the complex dielectric function independently without relying on reference measurements, an extrapolation into the spectral range not accessed by the experiment, or complementary data-sets, such as from transmission or dc transport experiments. Initially restricted to the visible part of the electromagnetic spectrum, the conceptual and technological progress over the years, e.g. the development of the Fourier-transform spectrometer, the ever growing computational power and the availability of synchrotron light sources, the limits has been pushed deep into the far-infrared even terahertz regime as well as the deep ultraviolet (UV) spectral range. This makes spectroscopic ellipsometry a powerful tool to elucidate the relevant interactions in strongly correlated electron systems.

[1] By "optical spectroscopy" we refer to spectroscopy with electromagnetic waves which started for natural reasons from the spectral range of visible light and was successively extended into both the (far-)infrared and ultraviolet spectral ranges.

[2] Nowadays a thin gold film evaporated onto the sample surface is typically used as a reference.

1.1 Scope of the thesis

In this thesis we apply broad band spectroscopic ellipsometry to study compounds from two material families both characterized by their enhanced electronic correlations, which have drawn much attention by the scientific community recently - the iridium oxides and the iron pnictides. Electronic correlations are directly encoded in the materials' dielectric function and can therefore be assessed by means of optical spectroscopy. Although many features and their respective energy scales are already extractable from the raw data,the insight into these complex materials is appreciably enhanced by comparing the experimental spectra with results from electronic structure calculations. All of the calculations presented within this work were performed by A. N. Yaresko, Max-Planck-Institute for Solid State Research.

In chapter 2 we introduce a basic model description of a material's dielectric response in terms of the Drude-Lorentz approach. We also review a Kramers-Kronig consistent description of asymmetric Fano line shapes. With the optical response at hand we discuss the methodological basis of spectroscopic ellipsometry and the subsequent data processing and analysis required to retrieve physically meaningful information about the materials from the ellipsometric raw data - the ellipsometric angles Ψ and Δ. One subsection is devoted to the spectroscopic ellipsometry setups employed in this work.

The results and their discussion are laid out in two chapters, 3 and 4, each concerned with one of the two material classes. In chapter 3 we will review the main characteristics of the iridium oxides on the basis of their prime example, Sr_2IrO_4, in particular the proposed $J_{\text{eff}} = 1/2$ ground state, which is believed to capture most of the essential properties in the family of iridium-oxides with perovskite structure. We present the full anisotropic complex dielectric function of Sr_2IrO_4 in a wide spectral range from 12 meV to 6.5 eV. The reported spectrum of infrared active phonons is compared to lattice dynamical calculations. Based on *ab-initio* band structure calculations we are able to reconcile the strong optical anisotropy, which we detect below ~ 2 eV in the c-axis dielectric response, to be consistent with the $J_{\text{eff}} = 1/2$ ground state and thus support its validity. With our enhanced knowledge of the $J_{\text{eff}} = 1/2$ ground state we turn to a novel compound, single crystalline $Na_3Ir_3O_8$. This is a semi-metallic counterpart of the geometrically frustrated hyperkagome compound $Na_4Ir_3O_8$, which is believed to host a three-dimensional spin liquid ground state. From the the dielectric response in the far-infrared spectral range we show that the conditions for Fano resonances – a fundamental quantum mechanical interference of a discrete state with an excitation continuum – are met in the infrared phonon spectrum of this material. All observable phonon resonances exhibit strongly asymmetric line shapes and a strongly temperature dependent amplitude which follows the strong temperature dependence of the electronic back-

ground. Comparing to fully relativistic band structure calculations within the local density approximation (LDA) of density functional theory (DFT) we are able to identify the low energy interband transitions which constitute the electronic background for the Fano interference. They arise from a low energy band structure where the lack of inversion symmetry in the lattice in combination with SOC leads to bands with almost linear dispersion, which are reminiscent of few-layer graphene. In contrast to case of graphene, where the observed amplitude of the phonon resonance is entirely due to the interference with the electronic background, the reasonable assumption of a considerable intrinsic electric dipole moment associated with the lattice vibrations is suggestive of a substantial electron-phonon coupling in $Na_3Ir_3O_8$.

In chapter 4 we turn to the 3*d* iron pnictides which provide the ability to modify effectively the strength of their electronic correlations and induce superconductivity by a variety of schemes – charge doping, external pressure and isovalent substitution – in this aspect clearly distinct from the cuprates. The latter of these is believed to affect primarily the structural properties due to the different extent of valence orbitals of the interchanged ions, e.g. 4*d* Ru replaces 3*d* Fe, but the natural question of how this impacts the electronic correlations arises immediately. Therefore we follow two routes to address this issue.

First we focus on the normal state properties of $Ba(Fe_{1-x}Ru_x)_2As_2$, where iron is substituted by ruthenium, and report the complex dielectric function over a broad doping range ($0 \leq x \leq 0.74$) covering all relevant phases: spin-density-wave, superconductivity and paramagnetic metallic regime. By means of a detailed dispersion analysis we uncover two separate regimes around optimal doping ($x \approx 0.35$). The characteristic optical parameters, the unscreened plasma frequency of the itinerant charge carriers ω_{pl} and the contribution of the MIR interband transitions to the static permittivity $\Delta\varepsilon_{\mathrm{MIR}}$, hardly change for $x < 0.35$ but are rapidly modified for larger x. Gauging ω_{pl} with the value estimated from LDA calculations reveals a progressive weakening of the electronic correlations due to Ru substitution.

In contrast to Ru substitution, which happens in the Fe-planes, the series of parent compounds AFe_2As_2 (A = Ca, Sr , Ba) could be considered as "isovalent" substitution in between the Fe-layers. Based on a detailed study of temperature dependence of the optical conductivity we are able to track all essential characteristics both in the normal and spin-density-wave state. We identify consistently two spin-density-wave gaps and associate them with two subsystems whose coupling evolves from weak (Ca) to strong (Ba) with the increasing ionic radius of the intercalant. Suppression of two optical interband transitions along with spectral weight redistribution at high energies induced by the spin-density-wave transition might originate from redistribution of the band populations at the transition. Systematic enhancement of the plasma frequency from Ba to Ca intercalation when compared to LDA results suggest a reduction

of electronic correlations in line with an increasing three-dimensionality in the system.

The final chapter 5 briefly summarizes our results.

2 Experimental and theoretical principles

As electronic correlations are directly encoded in the optical response of a specific material in this chapter we will outline how we can describe the optical response of a material through appropriate model functions and how to assess it experimentally by means of spectroscopic ellipsometry.

2.1 Optical response

The optical response of a linear, nonmagnetic[1] material is fully described by its complex electric susceptibility $\chi_{\mathrm{el}}(\omega)$, which relates the induced polarization $P(\omega) = \chi_{\mathrm{el}}(\omega)E(\omega)$ to the incident electric field $E(\omega)$ oscillating at frequency ω. In this chapter we use cgs units for convenience. In its most general form of an anisotropic material the susceptibility $\chi_{\mathrm{el}}(\omega)$ is given as a complex-valued symmetric second rank tensor $\chi_{ij}(\omega)$, $i, j \in [x, y, z]$, which in the case of an isotropic material reduces to a scalar function $\chi_{\mathrm{el}}(\omega) = \chi_1(\omega) + \mathrm{i}\chi_2(\omega)$ [26]. According to the constitutive relations to Maxwell's equations the electric susceptibility is directly linked to both the dielectric function $\varepsilon(\omega) = 1 + 4\pi\chi_{\mathrm{el}}(\omega)$ and the optical conductivity $\sigma(\omega) = -\mathrm{i}\omega\chi_{\mathrm{el}}(\omega)$, which therefore are complex-valued functions as well and can conveniently be combined into one quantity:

$$\varepsilon(\omega) = 1 + \frac{4\pi\mathrm{i}\sigma(\omega)}{\omega} \quad . \tag{2.1}$$

The frequency dependence of these response functions are solely determined by the spectral characteristics of the excitations in the material which add incoherently to the total dielectric function:

$$\varepsilon_{\mathrm{tot}} = \varepsilon_\infty + \varepsilon_{\mathrm{itinerant}} + \varepsilon_{\mathrm{interband}} + \varepsilon_{\mathrm{phonon}} + \dots$$

To disentangle the different contributions from excitations from core states $\varepsilon_{\mathrm{tot}}$, itinerant charge carriers $\varepsilon_{\mathrm{it}}$, interband transitions or phonons, to name the most prominent, it is highly desirable to develop a set of model dielectric functions to describe the optical spectra. However, the dielectric susceptibility being a physical response function has immediate consequences on its intrinsic, model-independent properties.

[1] Since magnetic moments respond more slowly to magnetic fields than charges do to electric fields, the magnetic response described by the permeability is safely set to $\mu = 1$ at infrared and optical frequencies.

2.1.1 Kramers–Kronig dispersion relations

Any physical response function has to obey the causality principle, which states that at time t the response of the system cannot precede the stimulus that acts at time t'. In other words, $\chi(t-t')=0$ for $t<t'$, which makes its Fourier transform $\chi(\omega)$ and equivalently the optical conductivity $\sigma(\omega)$ an analytical function in the upper half plane, when ω is continued to the complex frequency domain. The direct consequence is that the real and imaginary parts $\sigma_1(\omega)$ and $\sigma_2(\omega)$, respectively, are not independent but rather connected to each other:

$$\sigma_1(\omega)=\frac{1}{\pi}\mathcal{P}\int_{-\infty}^{\infty}\frac{\sigma_2(\Omega)}{\Omega-\omega}\mathrm{d}\Omega \tag{2.2a}$$

$$\sigma_2(\omega)=-\frac{1}{\pi}\mathcal{P}\int_{-\infty}^{\infty}\frac{\sigma_1(\Omega)}{\Omega-\omega}\mathrm{d}\Omega \tag{2.2b}$$

where $\mathcal{P}$ denotes the Cauchy Principal value of the integral which takes care of the singularity of the integrand at ω. These are the so-called Kramers–Kronig (KK) relations. Hence, the entire spectral information is already contained in the frequency dependance of either of the two components and the respective other can be obtained by integration over the entire frequency range. From the experimental point of view, however, Eqs. 2.2 are rather inconvenient to use since one has to know the response function also at negative frequencies ω. Fortunately, causality implies in addition that the real and imaginary parts of σ are even and odd functions in frequency, respectively, i.e. $\sigma(-\omega)=\sigma^*(\omega)$, where * denotes complex conjugation, and hence we can restrict the integrals in Eq. 2.2 to the positive frequency domain by expanding the fraction with $\Omega+\omega$ and integrating out the odd parts of the integrands:

$$\sigma_1(\omega)=\frac{2}{\pi}\mathcal{P}\int_{0}^{\infty}\frac{\Omega\sigma_2(\Omega)}{\Omega^2-\omega^2}\mathrm{d}\Omega \tag{2.3a}$$

$$\sigma_2(\omega)=-\frac{2\omega}{\pi}\mathcal{P}\int_{0}^{\infty}\frac{\sigma_1(\Omega)}{\Omega^2-\omega^2}\mathrm{d}\Omega \tag{2.3b}$$

Of course the dielectric function ε or to be more precise $\varepsilon-1=\chi_{\mathrm{el}}/4\pi$ is a response function, too, and hence equivalent relations are found for ε_1 and ε_2.

Inserting Eq. 2.1 into 2.3 we arrive at:

$$\varepsilon_1(\omega) - 1 = \frac{2}{\pi}\mathcal{P}\int_0^\infty \frac{\Omega\varepsilon_2(\Omega)}{\Omega^2 - \omega^2}\mathrm{d}\Omega \tag{2.4a}$$

$$\varepsilon_2(\omega) = -\frac{2\omega}{\pi}\mathcal{P}\int_0^\infty \frac{\varepsilon_1(\Omega) - 1}{\Omega^2 - \omega^2}\mathrm{d}\Omega \tag{2.4b}$$

These relations are of tremendous value in the analysis of optical data and we will come back to this later in section 2.1.3.

2.1.2 Model dielectric functions

Since full *ab initio* calculations of the dielectric functions are still difficult in complex systems, model dielectric functions are a useful tool to map the rich features often observed in the optical response onto a small set of parameters.

Drude-Lorentz formalism

Already more than a hundred years ago, long before the advent of quantum mechanics, Drude developed an astonishingly simple model to successfully describe the electronic properties of metals. Drude made essentially two assumptions, that the electrons move freely and independent of each other through the material, only disturbed from time to time by random collisions with the atomic cores.

Later on Lorentz extended this model to account also for electrons still bound to their atomic cores, forced to oscillate when excited by an electric field. Even though the Drude-Lorentz formula is an entirely classical approach, a rigorous quantum mechanical treatment by considering the applied electric field as a first order time-dependent perturbation to the Hamiltonian arrives qualitatively concerning the spectral dependence at the same expressions. For example the influence of the underlying periodic potential of the ionic cores, which leads to the description of the solid in terms of the electronic band structure as introduced by Bloch, can be to a large extent conveniently treated by replacing the free electron mass m_e by the band mass m_b, which is given by the curvature of the conduction band at the Fermi level. Since Drude's formula can be easily deduced afterwards from the Lorentz oscillator model in considering the zero-frequency limit of the resonance frequency ($\omega_0 \to 0$) we will start from the latter.

According to Newton's second law, the equation of motion for an electron with charge $-e$ and mass m that is bound to the positively charged nucleus

and experiences an time-dependent electric field $E(t)$ reads:

$$m\ddot{x}(t) = -eE(t) - m\gamma\dot{x}(t) - m\omega_0^2 x(t) \tag{2.5}$$

where the friction term $-m\gamma\dot{x}(t)$ accounts for dissipative losses in the system due to interactions with other atoms. The third term describes the restoring force according to Hooke's law, essentially a first order approximation of the atomic binding potential, with the resonance frequency ω_0. Assuming a monochromatic plane wave $E(\omega, t) = E_0 \cdot \exp(-\mathrm{i}\omega t)$ we can solve Eq. 2.5 by Fourier transformation and arrive at the amplitude $x_0(\omega)$ as a function of frequency:

$$x_0(\omega) = \frac{-eE_0}{m} \frac{1}{\omega_0^2 - \omega^2 - \mathrm{i}\gamma\omega}. \tag{2.6}$$

To get the dielectric response $\varepsilon(\omega)$ we look at the induced dipole moment $p = -ex_0$ which results in a macroscopic polarization P of N atoms per unit volume as $P = N\langle p\rangle = \chi_{\mathrm{el}} E$. From the dielectric susceptibility $\chi_{\mathrm{el}}(\omega) = 4\pi(\varepsilon(\omega) - 1)$ we get the frequency dependent dielectric function $\varepsilon(\omega) = 1 + \varepsilon_{\mathrm{Lorentz}}(\omega)$ with:

$$\varepsilon_{\mathrm{Lorentz}}(\omega) = \frac{\Delta\varepsilon\omega_0^2}{\omega_0^2 - \omega^2 - \mathrm{i}\omega\gamma} \tag{2.7a}$$

$$= \frac{\Delta\varepsilon\omega_0^2(\omega_0^2 - \omega^2)}{(\omega_0^2 - \omega^2)^2 + (\omega\gamma)^2} + \mathrm{i}\frac{\Delta\varepsilon\omega_0^2(\gamma\omega)}{(\omega_0^2 - \omega^2)^2 + (\omega\gamma)^2} \tag{2.7b}$$

where we have introduced the amplitude $\Delta\varepsilon\omega_0^2 = 4\pi Ne^2/m$ in which $\Delta\varepsilon$ describes the contribution of this oscillator to the static dielectric function $\varepsilon_s = \varepsilon(0)$. In the language of quantum mechanics $\Delta\varepsilon$ this is proportional to the oscillator strength $f \propto \Delta\varepsilon$, the probability that an specific oscillator, i.e. an electric dipole transition, is actually excited.

Now, to consider the response from the nearly free conduction electrons with carrier density N_{f} and mass m_{b} we just neglect the restoring force term in the equation of motion (2.5) and accordingly the Drude contribution to the complex dielectric function $\varepsilon(\omega)$ reads:

$$\varepsilon_{\mathrm{Drude}}(\omega) = -\frac{\omega_{\mathrm{pl}}^2}{\omega^2 + \mathrm{i}\omega\Gamma} \tag{2.8a}$$

$$= -\frac{\omega_{\mathrm{pl}}^2}{\omega^2 + \Gamma^2} + \frac{\mathrm{i}}{\omega}\frac{\omega_{\mathrm{pl}}^2\Gamma}{\omega^2 + \Gamma^2} \tag{2.8b}$$

where we have introduced the plasma frequency $\omega_{\mathrm{pl}} = \sqrt{4\pi N_{\mathrm{f}} e^2/m_{\mathrm{b}}}$ of the itinerant charge carriers and their scattering rate Γ. This is directly related to the dc conductivity by $\sigma_{\mathrm{dc}} = \sigma_1(0) = \omega_{\mathrm{pl}}^2/4\pi\Gamma$. At the plasma frequency all

itinerant charge carriers undertake a collective oscillation against the lattice of ionic cores comparable to a real plasma. However, this oscillation is longitudinal in nature and can therefore not be excited by light directly but shows up for example in electron loss spectroscopy experiments. The imaginary part of the corresponding response function $\mathrm{Im}[1/\varepsilon(\omega)]$ peaks at the plasma resonance, where also $\varepsilon_1(\omega) = 0$ holds.

In a real system the nonzero scattering rate Γ and partial screening from the core electrons and corresponding interband transitions are typically not negligible. They give rise to a nonzero contribution to the real part of the dielectric function at low frequencies, which for the sake of clarity shall here be subsumed in ε_∞. As a consequence the bare plasma frequency gets renormalized to the screened plasma frequency $\omega_{\mathrm{pl}}^{\mathrm{scr}}$, which we again derive from the condition $\varepsilon(\omega) = 0$:

$$\omega_{\mathrm{pl}}^{\mathrm{scr}} = \sqrt{\frac{\omega_{\mathrm{pl}}^2}{\varepsilon_\infty} - \Gamma^2} \tag{2.9}$$

Fig. 2.1 depicts examples for the Lorentzian and Drude terms as a function of photon energy, with the relevant parameters denoted. Especially the Lorentz term, because it is deduced from a very general harmonic oscillator model, has proven very successful in reproducing and parameterizing characteristic features in the dielectric function, such as interband transitions or phonon resonances.

Fano resonances: the generalized oscillator model

So far we have treated all contributions to the dielectric function independently. That means if two interaction channels for the photon, e.g. two different phonons or one phonon and an electronic excitation, are independent of each other they will just add incoherently to the total response $\varepsilon_{\mathrm{tot}} = \sum_j \varepsilon_j$ according two their respective oscillator strength – in full analogy to coupled classical harmonic oscillators. If, however, these channels are coupled by a coherent interaction V constructive and destructive interference will take place and distort the line shapes in the spectra from their regular Lorentzian form as described above. Depending on the interaction V the absorption on one side of the resonance will decrease while on the other it will increase resulting in a line shape asymmetric with respect to the resonance frequency ω_0. This is usually referred to as the Fano effect. In his original work Fano [27] has worked out theoretically the quantum-mechanical interference effect of one (or several) discrete states with a continuum of states and applied this description to the absorption spectra in electron scattering experiments on helium atoms, where the line shapes are affected by auto-ionization processes [27]. This concept of interference is not limited to Fano's atomic absorption spectra. Asymmetric line shapes as a manifestation of fundamental quantum mechanical interactions

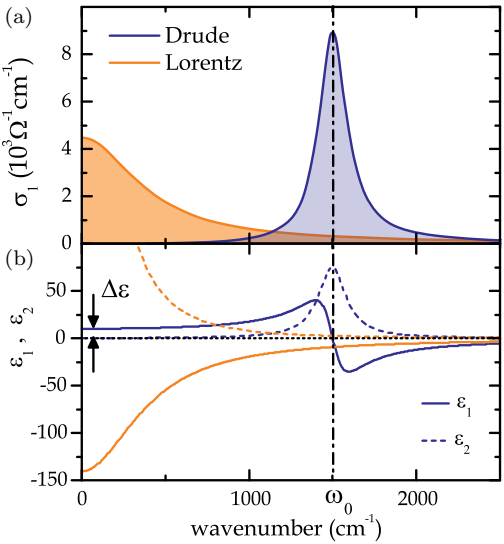

Figure 2.1: (a) The real part of the optical conductivity $\sigma_1(\omega)$ and (b) the real [$\varepsilon_1(\omega)$, solid lines] and imaginary [$\varepsilon_2(\omega)$, dotted lines] parts of the dielectric function for the Drude- (orange) and Lorentz-model (blue), respectively, as a function of wavenumbers. The integrated spectral weight SW (shaded area enclosed by σ_1) is identical for both models.

have indeed been observed in several different physical systems, especially nano-sized optical structures [for a review see Ref. 28 and references therein] and the formula given by Fano has been applied to describe, i.e. qualify, and even quantify the strength of the interaction V. One very recent example in the realm of optical spectroscopy are infrared phonons in few-layer graphene [29–31].

Following Fano [27], after subtraction of the background the asymmetric resonance in the real part of the optical conductivity $\sigma_{1,\mathrm{Fano}}$ is described by the real part of the following expression [32]:

$$\sigma_{\mathrm{Fano}}(\omega) = \mathrm{i}\sigma_0 \frac{(q-\mathrm{i})^2}{\epsilon+\mathrm{i}} \tag{2.10a}$$

$$= \sigma_0 \left[\frac{q^2-1+2q\epsilon}{\epsilon^2+1} + \mathrm{i}\frac{\epsilon(q^2-1)-2q}{\epsilon^2+1} \right] \tag{2.10b}$$

where σ_0 is the amplitude, $\epsilon = 2(\omega-\Omega)/\Gamma$ the dimensionless reduced frequency parameter with Ω and Γ the resonance frequency and the observable

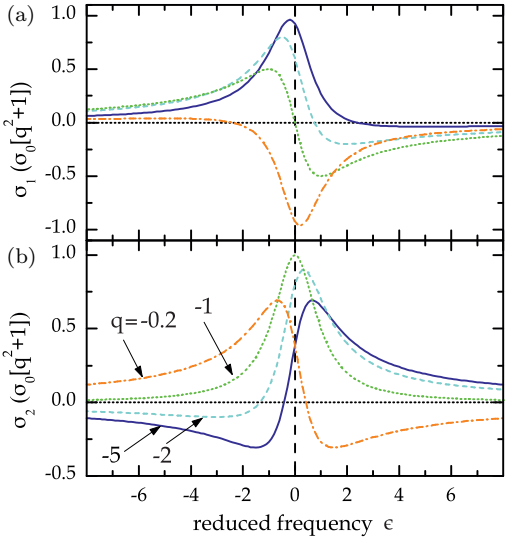

Figure 2.2: Asymmetric Fano line shapes in the (a) real and (b) imaginary part of the optical conductivity σ for different values of the Fano asymmetry parameter $q = -5, -2, -1, -0.2$ as a function of the reduced frequency $\epsilon = 2(\omega - \Omega)/\Gamma$ according to Eq. 2.10. For positive values of q the profiles in σ_1 are inverted with respect to $\epsilon = 0$ and $|q| \to \infty$ recovers the symmetric Lorentz curve profile.

line width, respectively. The Fano parameter q accounts for the asymmetry. The corresponding imaginary part $\sigma_{2,\mathrm{Fano}}$ is the Hilbert transform of $\sigma_{1,\mathrm{Fano}}$ or equivalently can be extracted from the *unconstrained* Kramers-Kronig relations as given in Eq. 2.2. The amplitude σ_0 is also often called the electronic background, since in Fano's original work the absolute resonance amplitude σ_0 is directly given by the absolute value of the continuum which forms the background. However, in most of the cases when the formula is used to fit arbitrary asymmetric line shapes on top of a smooth background, σ_0 is just used as a phenomenological scaling parameter of the resonance amplitude.

To recall the influence of the asymmetry parameter q on the line shape different situations are depicted in Figure 2.2. In the limit of $q \to \infty$ the regular Lorentz curve is recovered[2] around the resonance $\omega \approx \Omega$ (note the linear frequency dependence in the denominator which is equivalent to Eq. 2.7 only in the vicinity of the resonance Ω), while $|q| = 1$ describes the case of "maximal asymmetry", i.e. σ_1 has an dispersive character, and the bare resonance and

[2] Assuming appropriate scaling of the amplitude $\sigma_0(q \to \infty) = \Delta\varepsilon\Omega^2/[4\pi\Gamma q^2]$.

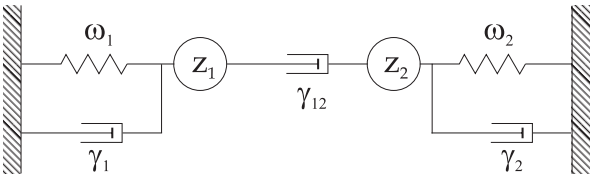

Figure 2.3: Mechanical analogon of two optic mode oscillators with the interaction damping realized by a dashpot γ_{12}. After Ref. 33.

the continuum contribute equally to the interference process. Finally, for $q = 0$ the resonance appears as an perfectly inverted Lorentzian in σ_1 which means perfectly destructive interference.

If we want to make full use of the inherent Kramers-Kronig consistency of the ellipsometric data in our experiments, i.e. expressing the real and imaginary part of the dielectric function independently in an analytical form, it is helpful to build up the model dielectric function from intrinsically KK-consistent constituents such as the Drude (2.8) and Lorentz (2.7) terms. Since Eq. 2.10 is not KK-consistent when restricted to the positive frequency domain we will turn to different approaches available in literature to cover this caveat. As a suitable fitting function the model should meet the following two conditions: in the limit of vanishing coupling the model has to recover the incoherent additive nature of the dielectric response for a linear medium. When we switch on the coupling the line shape around the resonance shall resemble the asymmetric shape of the Fano resonance as given in Eq. 2.10.

The classical analog of two coupled harmonic oscillators shall serve as the starting point for the subsequent considerations. Following Barker and Hopfield [33], on the lowest level the coupling can be introduced into the system in two different, but from the mathematical point of view entirely equivalent ways. We can either think of the oscillators connected by a spring providing harmonic force coupling or a dashpot, which provides an additional damping to the system. The latter is depicted in Fig. 2.3. Both examples can be converted into each other by a unitary transformation and therefore the solution will hold for both and even intermixed cases with both types of couplings present if the appropriate identifications of the parameters are done. As pointed out by the authors both forms have their own advantages in identifying certain properties of and connections between the participating oscillators. Without losing generality we choose the model with a dissipative interaction as also discussed by Humlíček *et al.* [34].

Therefore in analogy to the single Lorentz oscillator the coupled equations

of motion read:

$$\ddot{x}_1 + \gamma_1\dot{x}_1 + \gamma_{12}(\dot{x}_1 - \dot{x}_2) + \omega_1^2 x_1 = z_1 E \tag{2.11a}$$

$$\ddot{x}_2 + \gamma_1\dot{x}_2 + \gamma_{12}(\dot{x}_2 - \dot{x}_1) + \omega_2^2 x_2 = z_2 E \tag{2.11b}$$

where x_j, γ_j and ω_j $(j = 1, 2)$ are the displacements of the particles with effective charge z_j and their damping coefficients and resonance frequencies, respectively, driven by the stimulus E. To simplify the notation the particle mass m is absorbed into the effective charge and damping coefficients. The parameter γ_{12} represents the losses due to damping forces from the coupling dashpot proportional to the relative difference in velocity of the particles. Assuming again a plane wave of the form $E(t) \propto \exp[-\mathrm{i}\omega t]$ we find the solution for the mode amplitude x_{0j} by Fourier transformation and diagonalization. Calculating right away the polarization as $P = \sum_j z_j x_{0j} = (\sum_j \tilde{\varepsilon}_j - 1)E/4\pi$ we obtain the contributions to the complex dielectric function $\tilde{\varepsilon}_j$:

$$\tilde{\varepsilon}_1 = \frac{4\pi z_1^2 - \mathrm{i}\frac{4\pi z_1 z_2 \omega\gamma_{12}}{\omega_2^2 - \omega^2 - \mathrm{i}\omega(\gamma_2+\gamma_{12})}}{\omega_1^2 - \omega^2 - \mathrm{i}\omega(\gamma_1+\gamma_{12}) + \frac{\omega^2\gamma_{12}^2}{\omega_2^2 - \omega^2 - \mathrm{i}\omega(\gamma_2+\gamma_{12})}} \tag{2.12}$$

and $\tilde{\varepsilon}_2$ for interchanged indices $(1 \leftrightarrow 2)$ since we have introduced the coupling in a symmetric way. The line shape of both resonances gets progressively altered with increasing coupling strength γ_{12}. We can re-sort the terms in the numerator and denominator in Eq. 2.12 in order to establish the link to the symmetric Lorentz oscillator. In order to carve out the structure in the formula more clearly we define the following complex term:

$$R_{1,r} + \mathrm{i}R_{1,i} := \frac{1}{\omega_2^2 - \omega^2 - \mathrm{i}\omega(\gamma_2+\gamma_{12})} \tag{2.13}$$

which is essentially describes the frequency dependence of the other oscillator. Inserting this into Eq. 2.12 and separating the real and imaginary parts we arrive at:

$$\tilde{\varepsilon}_1 = \frac{\left[4\pi z_1^2 - 4\pi z_1 z_2 \omega\gamma_{12} R_r(\omega)\right] + \mathrm{i}4\pi z_1 z_2 \omega\gamma_{12} R_i(\omega)}{[\omega_1^2 + \omega^2\gamma_{12}^2 R_r] - \omega^2 - \mathrm{i}\omega[\gamma_1 + \gamma_{12} + \omega^2\gamma_{12}^2 R_i]} \tag{2.14}$$

We can rewrite this as:

$$\tilde{\varepsilon}_1 = \frac{S_1\left[\Omega_1^2 - \mathrm{i}\omega\beta_1\right]}{\Omega_1^2 - \omega^2 - \mathrm{i}\omega\Gamma_1} \tag{2.15}$$

where we have defined the renormalized resonance frequency Ω_1, amplitude S_1,

damping coefficient Γ_1 and asymmetry parameter β_1:

$$\Omega_1^2(\omega) := \omega_1^2 \left[1 + \frac{\omega^2 \gamma_{12}^2 R_r(\omega)}{\omega_1^2}\right] \tag{2.16a}$$

$$S_1(\omega) := \frac{4\pi z_1^2 (1 - \frac{z_1}{z_2}\omega\gamma_{12} R_r(\omega))}{\Omega_j^2} \tag{2.16b}$$

$$\Gamma_1(\omega) := \gamma_1 + \gamma_{12} - \omega\gamma_{12}^2 R_i(\omega) \tag{2.16c}$$

$$\beta_1(\omega) := \frac{z_1}{z_2}\gamma_{12} R_i \Omega_1^2 \quad . \tag{2.16d}$$

Again, interchanging all indices ($1 \leftrightarrow 2$) gives the corresponding terms of the second oscillator. This term has the form of a Lorentz resonance with a complex amplitude, which intermixes its real and imaginary parts. The degree of intermixing is given by the relative weight of the real and imaginary parts of the second oscillator at the resonance ω_1 of the first one. The way the second oscillator enters in these weights in this intermixing depends on the details of the underlying mechanical model. From Eq. 2.15 we can establish the link to Fano's original proposal (Eq. 2.10) making the following identifications. In the vicinity of the resonance $\omega \approx \omega_1$ we can approximate the background due to the second oscillator by $R(\omega) \approx R(\Omega_1)$ and the reduced photon energy ϵ reads accordingly:

$$\epsilon = \frac{\omega^2 - \Omega_1^2}{\omega\gamma} \approx \frac{2(\omega - \Omega_1)}{\gamma}$$

in analogy to Eq. 2.10. This constriction to parameters around the resonance demands an additional condition to maintain Kramers-Kronig- consistency. The full dielectric function ε has to vanish faster that $1/\omega$ for $\omega \to \infty$ and the hence the the sum of the additional asymmetry terms has to vanish [34]:

$$\sum_j S_j \beta_j \tag{2.17}$$

which is per definition fulfilled in the case of only two coupled oscillators, but becomes important for three and more. In the vicinity of the resonance frequency Ω_j we can also link both asymmetry parameters β_j and q_j:

$$\beta_j \approx \frac{2 q_j \Omega_j}{(q_j^2 - 1)} \tag{2.18}$$

One has to keep in mind, that within this approach not only β_j but also S_j becomes an independent fit parameter and can even take negative values $S_j \propto (q_j^2 - 1)$ for $q < 1$. Hence at $q = 1$ where β_j diverges, at the same time S_j vanishes and the total amplitude becomes purely imaginary. Along the same

line since the amplitude and hence the integrated spectral weight vanishes at $q = 1$ the "strength" of the resonance can instead be gauged by the strength parameter p [30]:

$$p_j = \frac{S_j \omega_j}{8} \frac{q_j^2 + 1}{q_j^2 - 1} \tag{2.19}$$

which accounts for both real and imaginary parts of the asymmetric resonance.

As pointed out by Humlíček *et al.* [34] this approach can easily be extended to an arbitrary number of coupled oscillators. To handle the cumbersome mathematics in a more efficient way we can employ a Green's function formalism [35, 36]. Let us consider K phonon modes coupled to an electronic excitation with individual strength V_j. Their bare functional frequency dependence is characterized by Green's functions G_j for the jth phonon and G_e for the electronic band analogous to Eq. 2.7:

$$G_j = \frac{\omega}{\omega_j^2 - \omega^2 - \mathrm{i}\gamma_j} \quad \text{and} \quad G_\mathrm{e} = \frac{\omega}{\omega_e^2 - \omega^2 - \mathrm{i}\gamma_e} \tag{2.20}$$

The Dyson equation

$$G = G_0 + G_0 V G \tag{2.21}$$

for the coupled excitation states (described by G) gives a system of coupled equations in G_j and G_e. Solving for G the Green's function matrix can be written as [35]

$$G^{-1} = \begin{pmatrix} G_1^{-1} & 0 & \dots & V_1 \\ 0 & G_2^{-1} & \dots & V_2 \\ \vdots & \vdots & \ddots & \vdots \\ V_1 & V_2 & \dots & G_e^{-1} \end{pmatrix} \tag{2.22}$$

and the optical conductivity σ given by the T-matrix via the optical theorem $\sigma_1 = -\frac{1}{\pi}\Im[T]$ (see e.g. [37]) reads:

$$\sigma(\omega) = 4\pi\mathrm{i}\,(A \cdot G \cdot A) \quad \text{with} \quad A = (A_1, A_2 \dots, A_e) \tag{2.23}$$

where the matrix elements A_j and A_e for the optical transitions determine the oscillator strengths A_j^2 and A_e^2 of the phonon modes and the electronic band, respectively. In this description we have considered just linear coupling V_j between the phonons and the electronic band.

The models presented above obey the Kramers-Kronig relations Eq. 2.3 even if restricted to the positive frequency domain and therefore are suitable tools in the analysis of asymmetric line shapes on top of arbitrarily shaped electronic backgrounds in the dielectric function as obtained by spectroscopic ellipsometry.

2.1.3 Sum rules and electronic correlations

The Kramers-Kronig relations 2.3 in combination with the gauge invariance of the electromagnetic field, which implies conservation of the total electric charge, lead to a set of integral formulas, which relate the frequency dependent optical response with the underlying physical absorption processes [38]. One of the most frequently used is the so-called oscillator strength sum-rule, or f-sum rule, for the real part of the optical conductivity $\sigma_1(\omega)$:

$$\int_0^\infty \sigma_1(\omega) d\omega = \frac{\pi N e^2}{2m_\mathrm{e}} \tag{2.24}$$

which connects the dissipation in the system represented by the spectral weight, i.e. the area enclosed by $\sigma_1(\omega)$, with the total density N and bare mass m_e of the excited particles. In a solid this gives a exact total count of all electrons present, both bound to the ionic cores and itinerant ones. It is worth noting that this result is independent of any model restrictions or boundary conditions. This formula proves very helpful when the system undergoes a phase transition, since the total spectral weight must be conserved at all times and redistribution in the spectral weight can be tracked.

Due to its generality Eq. 2.24 is also helpful in the task of disentangling the different contributions to the dielectric response and finds its application even more often in a restricted or truncated version. For example considering only the optical conductivity due to itinerant charge carriers $\sigma_{1,it}(\omega)$, which in the case of a Fermi liquid as we have seen above is well described by the Drude formula [Eq. 2.8], we arrive at [22, 39]:

$$SW_\mathrm{it} = \int_0^\infty \sigma_{1,\mathrm{it}}(\omega) d\omega = \frac{\omega_\mathrm{pl}^2}{8} = \frac{\pi N_\mathrm{it} e^2}{2m_\mathrm{b}} = \frac{2\pi e^2}{N\hbar^2} \sum_k \frac{\partial^2 \epsilon_k}{\partial k^2} n_k \quad . \tag{2.25}$$

where N_it is the itinerant charge carrier density and m_b denotes the electronic band mass averaged over the Brillouin zone as the inverse second derivative (band curvature) according to the last equality. n_k denotes the electron momentum distribution function. The plasma frequency $\omega_\mathrm{pl} = \sqrt{4\pi N_\mathrm{it} e^2/m_\mathrm{b}}$ is defined in analogy to the Drude term (2.8). In a tight binding approach with only nearest neighbor interaction the spectral weight SW_it (or plasma frequency ω_pl^2) from Eq. 2.25 is proportional to the kinetic energy K, which is defined as $K = 2/N \sum_k \epsilon_k n_k$ and accordingly reads:

$$K = \frac{\pi e^2}{4\hbar^2} \omega_\mathrm{pl}^2 \quad . \tag{2.26}$$

While in weakly correlated systems the band mass m_b is well described by

band structure calculations within the framework of DFT, high energy strong electronic correlations such as Coulomb repulsion will effectively increase the band mass m_b. In case of the latter since the total spectral weight has to be conserved [Eq. 2.24] spectral weight from the itinerant response is transferred to higher energies into the spectral range of the interband transitions. Since these electronic correlations are not very well captured in the DFT calculations within the local density approximation the plasma frequency extracted from these calculations ω_{pl}^{LDA} is typically overestimated with respect to the experimental values. Therefore we can actually use this caveat of LDA to our advantage and gauge the strength of the electronic correlations by the ratio $(\omega_{pl}^{exp}/\omega_{p}^{LDA})^2$ or within the tight binding model by the kinetic energy ratio K_{exp}/K_{LDA}. Weakly correlated systems (Fermi liquids), like elemental metals, show values of this ratio close to unity, strongly correlated materials, such as lightly doped cuprate high-T_c superconductors, exhibit a ratio close to zero.

Coupling of the electrons to additional bosons, such as phonons or spin-excitations, characterized by a frequency dependent coupling strength $\lambda(\omega)$, leads to a further increase of the then also frequency dependent effective mass $m^*(\omega) = m_b(1 + \lambda(\omega))$ at energies below the characteristic frequency of the respective boson Ω_0 [40]. It is important to note that these low energy modifications of m^*, while for example very helpful in identifying the characteristic energy of the coupling boson in the Cooper-pair formation in superconductors, typically do not affect the plasma frequency or kinetic energy as defined above, unless it is extremely strong [22]. For example both the phonon-mediated superconductor MgB_2 and metallic Cr, which is prone to a spin-density-wave instability, show $K_{exp}/K_{LDA} \approx 0.8$ [41].

Since a real optical spectroscopy experiment is always restricted to a finite frequency range, we can consider the spectral weight up to certain cut-off frequency Ω and define an effective number of electrons $N_{eff}(\Omega)$ that contribute to the electromagnetic absorption at frequencies below Ω [22]:

$$N_{eff}(\Omega) = \frac{2m_e}{\pi e^2}\int_0^{\Omega}\sigma_1(\omega)d\omega = \frac{2m_e}{\pi e^2}\frac{(\omega_{pl}^{exp})^2}{8} \tag{2.27}$$

If the dielectric response from the itinerant charge carriers is well separated in energy from the interband transitions by choosing the cut-off Ω just in between, as in the ideal case to account for all itinerant but none of the interband contributions to the dielectric function, the experimental plasma frequency ω_{pl}^{exp} associated with the itinerant charge carriers can be estimated. However, as we will see in chapter 4 this becomes difficult when intra- and interband transitions strongly overlap in energy in addition to the inevitably limited frequency range accessible in the experiments. In this case spectroscopic ellipsometry provides additional information since both real and imaginary parts of the dielectric

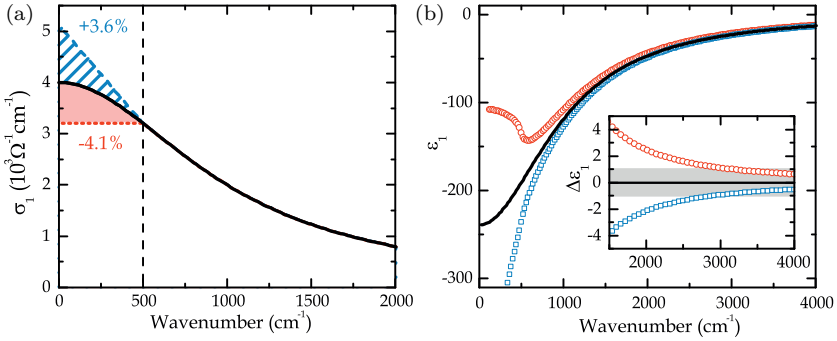

Figure 2.4: Kramers-Kronig consistency analysis. (a) Real part of the optical conductivity according due a Drude term with $\sigma_0 = 4000\,\Omega^{-1}\mathrm{cm}^{-1}$ and $\Gamma = 1000\,\mathrm{cm}^{-1}$ and two deviating extrapolations below $\Omega_c \leq 500\,\mathrm{cm}^{-1}$. (b) Real part of the dielectric function as obtained by Kramers-Kronig transformation from the spectra in (a). Inset: deviation of the two different extrapolations with less and excess spectral weight, respectively. The shaded area denotes the typical noise level of $\delta\varepsilon_1 = \pm 1$ in this spectral range.

function are obtained independently and the KK relations [Eq. 2.4] can still be applied to estimate the spectral weight outside the experimentally accessible range.

Kramers-Kronig consistency analysis

The Kramers-Kronig relations (Eq. 2.3 and 2.4) require integration over the entire frequency range. This is of course not available in an experiment and the frequency range has naturally a lower and upper cut-off. Nevertheless in a combined approach of dispersion analysis and applying the KK relations we can still estimate the spectral weight outside the experimental range, if the low energy range which hosts the itinerant charge carrier response is of high interest for us. The procedure consists of two steps. First, we model the high energy interband transitions consistently with a set of Lorentz oscillators. After subtracting these we extrapolate the remainder to zero frequency to account for the low energy spectral weight. The integrated spectral weight in the extrapolation region can be estimated by calculating the real part of the dielectric function $\varepsilon_1^{\mathrm{calc}}(\omega_i)$ from the extrapolated imaginary part at certain frequencies ω_i within the experimental using Eq. 2.4a spectral range and compare these calculated values with the experimental ones, $\varepsilon_1^{\mathrm{exp}}(\omega_i)$. We illustrate this procedure in Fig. 2.4 on the basis of a simple Drude term (Eq. 2.8), which models the free charge carrier response after subtracting the high energy interband

contributions. Panel (a) of Fig. 2.4 shows the Drude term with parameters of $\sigma_{\mathrm{dc}} = 4000\,\Omega^{-1}\mathrm{cm}^{-1}$ and $\Gamma = 1000\,\mathrm{cm}^{-1}$ typical values for the normal state properties of the iron based superconductors. The Drude term is truncated at a rather high value of $\Omega_c = 500\,\mathrm{cm}^{-1}$ for the low energy experimental cut-off. Below Ω_c we assume three different possible extrapolations, constant, linear and as a reference the analytical continuation of the Drude term. The constant extrapolation accounts for $\sim 4\%$ less, the linear extrapolation for $\sim 3.6\%$ more spectral weight than the original Drude term. The corresponding calculated spectra of $\varepsilon_1^{\mathrm{calc}}(\omega_i)$ at frequencies ω_i for all three extrapolations are shown in panel (b) and the difference with respect to the analytical Drude term in panel (c). The difference is small but clearly detectable above a typical noise level not larger than $\delta\varepsilon_1 = \pm 1$ in this spectral range when the deviation is averaged over a finite frequency range, e.g. $2000\,\mathrm{cm}^{-1} < \omega < 4000\,\mathrm{cm}^{-1}$. Since only the integrated spectral weight in the extrapolation region is determined some uncertainty remains about the influence of the actual spectral weight distribution in the extrapolation region on this analysis. According to Charnukha *et al.* [42] we can estimate the maximum uncertainty introduced by the unknown shape from the two extreme configurations: all extrapolated SW_{ext} at $\omega = 0$ or $\omega = \Omega_c$. Then the uncertainty at frequency ω introduced by the relative shape change scales with $(\Omega_c/\omega)^2$ with respect to the SW_{ext} in the extrapolation region. For the rather extreme value $\Omega_c = 500\,\mathrm{cm}^{-1}$ the *relative* uncertainty amounts to only $\sim 6\%$ at $\omega = 2000\,\mathrm{cm}^{-1}$ which is certainly negligible in our analysis. This procedure becomes even more valuable when applied to difference spectra of different temperatures, for example just above and below a phase transition. Interband transitions at very high photon energies (UV spectral range) are usually almost temperature independent since phase transitions typically involve states near the Fermi level. Therefore it often is well justified to assume that the difference in the optical conductivity at high frequencies is vanishing and the spectral weight has to be conserved in the spectral range below. This for example allows one to determine precisely the spectral weight transfer to the superconducting condensate according to the related Ferrell-Glover-Tinkham sum-rule [43].

2.2 Spectroscopic Ellipsometry

After having laid out the intrinsic properties of the optical response and how to model it in terms of analytic expressions for the dielectric function we can turn now to the question, how to assess this quantity experimentally.

As discussed above it is sufficient to measure only one of the components of the dielectric function and obtain the other by applying the respective KK relations. In the case of absorbing materials this can be done by means of

normal incidence reflectivity which still has to be carried out over the entire frequency range or extrapolated where not measured. Although in its long history the technique has been constantly improved and the spectral range covered today extends from about 3 meV in the terahertz regime to several eV in the UV range the task is still cumbersome. An alternative approach is offered by spectroscopic ellipsometry. The measurement principle of ellipsometry is based on the observation that mutually orthogonal electric field components of polarized light that is reflected from an interface of two optically different media experience a well defined relative phase shift and relative attenuation of their amplitudes. In the following we will show how we can make use of this fundamental observation to extract the full complex dielectric function over a limited spectral range without having to refer neither to Kramers-Kronig relations nor extrapolation beyond the experimentally assessed spectral range. To work out the relevant relations it is instructive to start from the reflection of light from a planar surface. A comprehensive treatise of the important aspects of ellipsometry from both theoretical and technical point of view can be found in the compendia R.M.A. Azzam and N.M. Bashara [44] or more recently H. G. Tompkins and E. A. Irene [45].

2.2.1 Light reflection from a planar interface

The Fresnel equations

The general situation of light reflection from an interface is laid out in Fig. 2.5. For the sake of simplicity, the first medium is to be vacuum and the second, the actual material under study is to be homogenous, non-magnetic and linear in its optical response. As discussed above in this case the optical properties are fully characterized by scalar, yet complex refractive index $N = n + \mathrm{i}\kappa$, for vacuum of course $N = 1$ holds, or equivalently by their dielectric function $\varepsilon = \varepsilon_1 + \mathrm{i}\varepsilon_2 = (n + \mathrm{i}\kappa)^2$; hence $\varepsilon_1 = n^2 - \kappa^2$ and $\varepsilon_2 = 2n\kappa$. For the sake of convenience in notation throughout this discussion we will use the refractive index $N = \sqrt{\varepsilon}$. Moreover, the general case of a different ambient can always be recovered by replacing N with the ratio of N_2/N_1 everywhere.

Now let us analyze the light reflection as sketched in Fig.2.5. A monochromatic ray of (not necessarily linearly) polarized light hits the interface at an angle θ_i with respect to the surface normal. The wave is partially reflected back at the same angle $\theta_\mathrm{r} = \theta_\mathrm{i}$, while the remaining is refracted at an angle θ_t into the material. At the interface we have to match the electric and magnetic field components of the incident and reflected beam on one side with the ones for the refracted beam on the other. To do so it is favorable to consider the electric field vectors E of the beams as a superposition of two components E_s perpendicular and E_p parallel to the plane of incidence, respectively, which

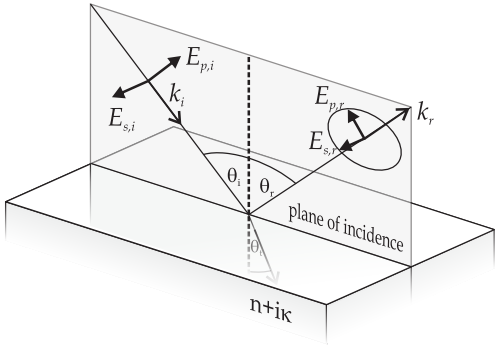

Figure 2.5: Reflection and transmission of a plane wave at an planar interface of a material with complex refractive index $n + i\kappa$. The plane of incidence is defined by the k-vectors of the in- and out-going rays with their electric field components $E_{\mathrm{p,i}}$, $E_{\mathrm{s,i}}$ and $E_{\mathrm{p,r}}$, $E_{\mathrm{s,r}}$, respectively. Part of the beam is refracted into the sample at the angle θ_{t}.

is defined by the propagation vectors k_{i} and k_{r} of the in- and outgoing rays. The field components before ($E_{\mathrm{s,i}}$, $E_{\mathrm{p,i}}$) and after the reflection ($E_{\mathrm{s,r}}$, $E_{\mathrm{p,r}}$) are linked by the respective reflection coefficients r_{s} and r_{p},

$$E_{\mathrm{s,r}} = r_{\mathrm{s}} E_{\mathrm{s,i}} \quad \text{and} \quad E_{\mathrm{p,r}} = r_{\mathrm{p}} E_{\mathrm{p,i}} \quad . \tag{2.28}$$

Following the proper boundary conditions for the vector components of the electric and magnetic fields and the constitutive relations for a linear medium leads to Fresnel's equations for reflection:

$$r_{\mathrm{s}} = \frac{E_{\mathrm{s,r}}}{E_{\mathrm{s,i}}} = \frac{\cos\theta - \sqrt{N^2 - \sin^2\theta}}{\cos\theta + \sqrt{N^2 - \sin^2\theta}} = |r_{\mathrm{s}}|\, e^{\mathrm{i}\delta_{\mathrm{s}}} \tag{2.29a}$$

$$r_{\mathrm{p}} = \frac{E_{\mathrm{p,r}}}{E_{\mathrm{p,i}}} = \frac{N^2\cos\theta - \sqrt{N^2 - \sin^2\theta}}{N^2\cos\theta + \sqrt{N^2 - \sin^2\theta}} = |r_{\mathrm{p}}|\, e^{\mathrm{i}\delta_{\mathrm{p}}} \tag{2.29b}$$

where we have expressed the complex numbers r_{s} (r_{p}) through their amplitudes $|r_{\mathrm{s}}|$ ($|r_{\mathrm{p}}|$) and complex phase δ_{s} (δ_{p}). We can define their complex ratio ρ:

$$\rho = \frac{r_{\mathrm{p}}}{r_{\mathrm{s}}} = \tan\Psi e^{\mathrm{i}\Delta} \tag{2.30}$$

where Δ denotes the relative phase shift $\Delta = \delta_{\mathrm{p}} - \delta_{\mathrm{s}}$ between the p- and s-polarized components and $\tan\Psi = |r_{\mathrm{p}}| / |r_{\mathrm{s}}|$ the relative attenuation of the dielectric field amplitudes upon reflection at the interface. Ψ and Δ are known

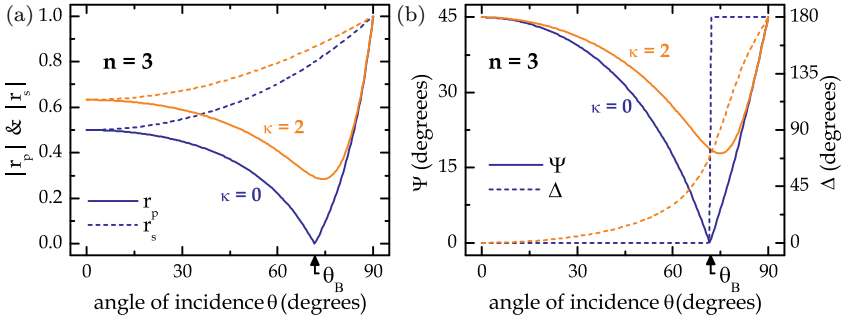

Figure 2.6: (a) The reflectivity coefficients r_p and r_s and (b) the ellipsometric angles Ψ and Δ as a function of the angle of incidence θ for $n = 3$ and various $\kappa = 0$ and $\kappa = 2$. θ_B denotes the Brewster angle for $\kappa = 0$.

as the ellipsometric angles and are solely determined by the dielectric function of the material and the angle of incidence θ. It is worth having a look how these parameters, r_s, r_p, Ψ and Δ, depend on the angle of incidence θ. This is illustrated in the Figures 2.6(a) and (b) for two sets of optical constants, i.e. a transparent ($\kappa = 0$) and an strongly absorbing material ($\kappa = 2$) with the same real part of the refractive index $n = 3$. As expected the amplitudes of r_p and r_s are the same at normal incidence since the different directions along the interface become indistinguishable[3]. While the amplitude $|r_\mathrm{s}|$ is growing monotonously with increasing θ, $|r_\mathrm{p}|$ is going through a minimum before both reach unity at gracing incidence ($\theta = 90°$). For $\kappa = 0$ r_p and thus Ψ go to zero at the Brewster angle θ_B. In the case of monochromatic, purely p-polarized incident light the reflected beam disappears. At the Brewster angle Δ changes abruptly from 0 to 180°. With increasing κ values this behavior gets "rounded". Ψ does not reach zero anymore but still exhibits a minimum at the principal angle θ_P, where also $\Delta = 90°$ holds. θ_B and θ_P coincide for a transparent material ($\kappa = 0$) and are still fairly close to each other for finite κ.

We can see right away, that this angle dependence of Ψ and Δ has immediate consequences for the actual ellipsometric measurements. Since Ψ and Δ change strongly around the principal angle θ_P and are almost independent of the refractive index $\tilde{n}+\mathrm{i}\kappa$ around the extremes of normal and gracing incidence, ellipsometric measurements are usually performed with an angle of incidence close to θ_P. For transparent materials ($\kappa = 0$) the Brewster angle is given by

[3]The opposite sign for r_p and r_s as given in Eq.2.29 is due to the sign convention adopted when deducing Fresnel's equations. We have chosen the so-called Verdet convention where the reference coordinate system is always attached to the direction of propagation rather than fixed to the interface. For a detailed discussion see Ref. 46.

$\tan\theta_B = N$, i.e. $\theta_B \geq 45°$ for $N \geq 1$, and keeps growing for absorptive materials approaching 90° for strongly metallic materials. Hence typical angles of incidence lie between 65° and 80° sometimes up to 85°.

Now, with Eq. 2.29 and 2.30 at hand we can define the so-called *pseudo-dielectric function* $\langle\varepsilon\rangle$, which is simply a direct inversion of Eq. 2.30:

$$\langle\varepsilon\rangle = (\sin\theta)^2 + (\sin\theta\tan\theta)^2 \left(\frac{1+\tan\Psi e^{i\Delta}}{1-\tan\Psi e^{i\Delta}}\right)^2 \tag{2.31}$$

In the case of an ideally flat interface of an isotropic material as discussed just now $\langle\varepsilon\rangle$ is already equal to the true dielectric function ε. More complex materials, may it be a layered systems, e.g. thin films on top of a substrate, or materials with an anisotropic dielectric function due to a non-cubic crystal symmetry, require an optical model to extract the individual components of the dielectric tensor or true dielectric functions of the separate constituents. Fortunately, for bulk materials with only moderate optical anisotropy the pseudo-dielectric function $\langle\varepsilon\rangle$ is often very close to the real ε with only minor corrections to absolute values of ε, which for example do not alter characteristic signatures in the spectra. Therefore already the pseudo-dielectric function can be a valuable tool in the analysis of optical spectra – sometimes it might even be the only quantity available. However, care must be taken for low crystal symmetry since in this case the pseudo-dielectric function does not necessarily obey the KK relations anymore and might show unphysical behavior. In this case a disentanglement of the dielectric tensor components is indispensable [47].

Uniaxial anisotropy

So far we have focused on the simplest case of isotropic materials, where the optical response at a certain wavelength ω is fully characterized by a single complex quantity, $\rho(\omega)$. For arbitrarily anisotropic, non-magnetic materials the dielectric response is no longer a scalar but described by a symmetric second rank tensor $\hat{\varepsilon}$. In principal the the electric field $\vec{E}$ and the electric displacement field $\vec{D} = \hat{\varepsilon}\vec{E}$ and will not be collinear anymore. It is possible to describe the reflection from such a sample surface in the framework of the Jones formalism, where ρ becomes a 2×2-matrix:

$$\begin{pmatrix} E_{p,r} \\ E_{s,r} \end{pmatrix} = \begin{pmatrix} r_{pp} & r_{ps} \\ r_{sp} & r_{ss} \end{pmatrix} \begin{pmatrix} E_{p,i} \\ E_{s,i} \end{pmatrix} \tag{2.32}$$

where $E_{p/s,i}$ and $E_{p/s,i}$ denote again the electric field amplitudes before and after the reflection as in Eq. 2.29. The off-diagonal elements r_{ps} and r_{sp} account for the possible transformation from s- into p-polarization and vice versa.

Uniaxial anisotropic materials have one distinct crystallographic direction–

the optical axis. Their dielectric tensor $\hat{\varepsilon}$ has to respect the crystal symmetry and hence has only two different eigenvalues, ε_o and ε_eo, which characterize the propagation of the ordinary and extraordinary beams, respectively, e.g. well known from birefringent crystals like calcite. For a more detailed discussion on arbitrary anisotropy we refer to Ref.44.

In an ellipsometry measurement the actual orientation of the sample is one the experimentally accessible parameters. Thus when we consider the orientation of the optical axis with respect to the sample surface and the plane of incidence there are three high symmetry configurations which are of special interest.

1. The optical axis is normal to the interface:

$$r_\mathrm{ss} = \frac{\cos\theta - \sqrt{N_\mathrm{o}^2 - \sin^2\theta}}{\cos\theta + \sqrt{N_\mathrm{o}^2 - \sin^2\theta}} \tag{2.33a}$$

$$r_\mathrm{pp} = -\frac{N_\mathrm{o}N_\mathrm{e}\cos\theta - \sqrt{N_\mathrm{e}^2 - \sin^2\theta}}{N_\mathrm{o}N_\mathrm{e}\cos\theta + \sqrt{N_\mathrm{e}^2 - \sin^2\theta}} \tag{2.33b}$$

2. The optical axis is parallel both to the surface and plane of incidence:

$$r_\mathrm{ss} = \frac{\cos\theta - \sqrt{N_\mathrm{o}^2 - \sin^2\theta}}{\cos\theta + \sqrt{N_\mathrm{o}^2 - \sin^2\theta}} \tag{2.34a}$$

$$r_\mathrm{pp} = -\frac{N_\mathrm{o}N_\mathrm{e}\cos\theta - \sqrt{N_\mathrm{o}^2 - \sin^2\theta}}{N_\mathrm{o}N_\mathrm{e}\cos\theta + \sqrt{N_\mathrm{o}^2 - \sin^2\theta}} \tag{2.34b}$$

3. The optical axis is parallel to the surface but perpendicular to the plane of incidence:

$$r_\mathrm{ss} = \frac{\cos\theta - \sqrt{N_\mathrm{e}^2 - \sin^2\theta}}{\cos\theta + \sqrt{N_\mathrm{e}^2 - \sin^2\theta}} \tag{2.35a}$$

$$r_\mathrm{pp} = -\frac{N_\mathrm{o}^2\cos\theta - \sqrt{N_\mathrm{o}^2 - \sin^2\theta}}{N_\mathrm{o}^2\cos\theta + \sqrt{N_\mathrm{o}^2 - \sin^2\theta}} \tag{2.35b}$$

For these high symmetry cases the off-diagonal elements r_ps and r_sp vanish irrespective of the angle of incidence θ and we can again define Ψ and Δ equivalently to Eq. 2.29 for each specific experimental configuration as $\rho = r_\mathrm{pp}/r_\mathrm{ss}$.

By collecting data sets from different faces of a single crystal or rotating the sample about its surface normal if the optical axis resides in the sample

surface plane and fitting to an appropriate optical model which accounts for the anisotropy, we can disentangle the tensor components ε_{o} and $\varepsilon_{\mathrm{eo}}$, respectively. When analyzing the dependence of Ψ and Δ on the orientation of the optical axis with respect to the sample surface in more detail, one finds that the optical response is grossly governed by the projection of the dielectric tensor $\hat{\varepsilon}$ onto the intersection of the plane of incidence with the sample surface. This can be very valuable as an experimental rule of thumb[4]. Therefore, when studying uniaxial materials the cases (1) and (2) shown above are the most relevant ones. We will discuss the procedure in more detail when applied in chapter 4.

[4]This is mainly due to the fact that r_{pp} is more sensitive to the angle of incidence than r_{ss}, especially around the principal angle θ_{P}.

2.3 Ellipsometer designs and measurement protocol

The experimental task of measuring the two ellipsometric angles $\Psi(\omega, \theta)$ and $\Delta(\omega, \theta)$, in order to retrieve the optical properties of the material under investigation, has now been tackled for more than a century. Since the time of Drude's hand-operated single wavelength "null ellipsometer" many different designs have been realized culminating nowadays in fully automated broad band spectroscopic setups, a lot of them commercially available. A thorough overview of different designs, optical components and suitable measurement protocols can be found in Ref. 45. In the following after discussing general aspects of the data acquisition process and common design features of the setups we employed, we will outline specific features and implementations of the respective setups.

A typical spectroscopic ellipsometer consists of the following components, which are partially sketched in Fig. 2.7: a light source with a broad spectral range followed by a monochromator unit (not shown), a first rotatable linear polarizer defining the initial polarization state, a retarder (optional) introducing an additional phase shift, the sample stage, typically a cryostat, the second rotatable linear polarizer, called analyzer, and the detector. First, we will have a look at the signal detection and how we can retrieve two quantities Ψ and Δ from measuring the reflected light intensity only. Light propagation through the

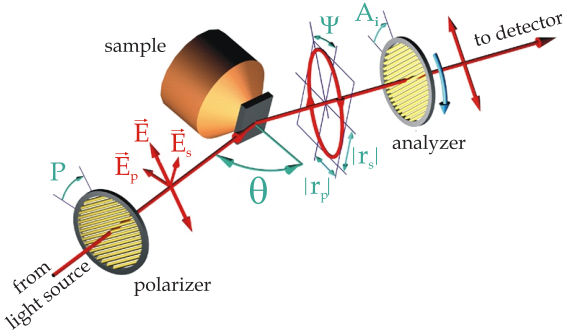

Figure 2.7: Basic rotating analyzer ellipsometry layout: light from the source is linearly polarized at an angle P with respect to the plane of incidence and reflected from the sample at an angle θ. Thereby the two electric field components E_p and E_s experience a relative phase shift Δ and relative attenuation Ψ upon reflection causing in general elliptical polarization, which is analyzed by a second linear polarizer at different azimuth angles A_i. Courtesy of A. V. Boris.

system can be conveniently treated in the framework of the Jones formalism[5], where the polarization state of light is described by a two-component vector, representing two orthogonal polarization states, and each optical component in the beam path is represented by a 2×2 matrix [45].

To deduce the detector signal we consider the simple case of an isotropic material only. In this case the Jones matrix for the sample becomes diagonal and the diagonal components r_p and r_s are given as in Eq. 2.29. For the respective electric field components E_p and E_s after the sample we arrive at

$$\begin{pmatrix} E_\mathrm{p} \\ E_\mathrm{s} \end{pmatrix} = E_0 r_\mathrm{s} \begin{pmatrix} \rho & 0 \\ 0 & 1 \end{pmatrix} \begin{pmatrix} \cos P \\ \sin P \end{pmatrix}. \tag{2.36}$$

where E_0 denotes the electric field strength of the unpolarized light passing through the first polarizer set at azimuth P with respect to the plane of incidence. We have introduced $\rho = r_\mathrm{p}/r_\mathrm{s}$ as given in Eq. 2.30. Since the detector is sensitive to light intensities $I = \langle E^* E \rangle$ only, after passing the analyzer set at azimuth A the normalized intensity $I(A)/I_0$ reads Tompkins and Haber [45]:

$$\frac{I(A)}{I_0} = 1 + \alpha \cos(2A) + \beta \sin(2A) \tag{2.37}$$

with

$$\alpha = \frac{\tan^2 \Psi - \tan^2 P}{\tan^2 \Psi + \tan^2 P} \quad , \quad \beta = \frac{2 \tan P \tan \Psi \cos \Delta}{\tan^2 \Psi + \tan^2 P}$$

being the normalized second order cosine and sine and $I_0 = |E_0|^2 |r_\mathrm{s}|^2$ the zeroth order Fourier coefficients. From the signal $I(A)$ measured at a set of (at least four) different analyzer azimuth angles A we extract α and β by numerical discrete Fast-Fourier-Transformation and thereby gain the ellipsometric angles $\Psi(\omega)$ and $\Delta(\omega)$ at each frequency ω:

$$\tan \Psi = \sqrt{\frac{1+\alpha}{1-\alpha}} |\tan P| \qquad \text{and} \qquad \cos \Delta = \frac{\beta}{\sqrt{1-\alpha^2}} \frac{\tan P}{|\tan P|} \tag{2.38}$$

These equations form the basis of the ellipsometric measurements using the rotating analyzer scheme (RAE). In complete analogy the same can be achieved by rotating the polarizer and keeping the analyzer azimuth fixed at an intermediate value. Then the formulae above hold if P and A are interchanged.

From Eqs. 2.38 we see that in an ellipsometric measurement we actually do not determine Ψ and Δ directly but rather $\tan \Psi$ and $\cos \Delta$. This has the caveat that Δ obtained from RAE is only defined in the range 0° to 180°, i.e. we cannot detect the rotational direction of the polarization ellipse, and even

[5] A full description also taking into account depolarization effects is given by the Müller-matrix formalism [44].

more important the uncertainty increases for $\cos|\Delta| \approx 1$ since small deviations in $\cos\Delta$ will lead to large changes in Δ. Here comes the retarder into play which introduces an additional phase shift Δ_c. The detected Δ' is shifted to $\Delta' = \Delta + \Delta_c \approx 90°$, we regain sensitivity and Δ can be determined in its entire range $-180°$ to $180°$.

The large spectral range we want to cover – three orders of magnitude in photon energy from the far-infrared (FIR) of a few meV to the ultraviolet (UV) up to 6.5 eV – demands a series of setups ideally with overlapping spectral ranges. Each spectral range requires its own set of optical components. Particular care must be taken when choosing the polarizers, since the entire measurement scheme strongly relies on a precisely known state of initial polarization.

All experiments presented in this work have been performed on two different types of setups: In the visible and UV spectral range dispersive spectrometers are still successfully employed, where diffraction gratings are utilized to obtain quasi-monochromatic radiation from a lamp with continuous spectrum. In the infrared, however, following a proposal by Roeseler [48], Fourier transform spectrometers show superior performance and are almost exclusively used in infrared spectroscopy today. The advantages of using a FT spectrometer are typically categorized as: i) a larger throughput, i.e. higher intensity is reaching the detector, also called Jaquinot advantage, ii) all frequencies being measured at the same time, the multiplex advantage, and iii) due to the HeNe-Laser as a reference for the mirror position the wavenumbers are determined much more accurately. These benefits improve significantly the signal-to-noise ratio, increase the spectral resolution and/or make the measurement simply fast enough to make ellipsometric measurements in the infrared feasible.

Now, we will describe the setups employed in this work in more detail, especially with respect to their properties specifically adjusted and optimized for the respective spectral range.

Fourier Transform Spectroscopy in the Infrared

Measurements in the infrared spectral range were performed on three different setups, two of them located at synchrotron radiation facilities – the IR1 beam line at the ANKA synchrotron of the Karlsruhe Institute of Technology, Germany, and the U4IR beam line of the NSLS synchrotron at the Brookhaven National Laboratory, USA. Detailed description of these setups are given by Bernhard *et al.* [49] and Stanislavchuk *et al.* [50], respectively. Schematic outlines of these far-infrared setups are depicted in Fig. 2.8(a) and (b).

As outlined above, in the infrared (IR) region - covering the range from 10 meV up to 1 eV - the setups employ Fourier transform spectrometers[6] (FTS)

[6] Bruker IFS 66v/S and Vertex 80v.

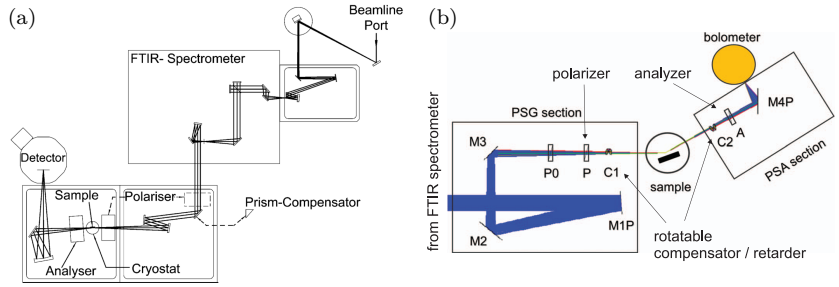

Figure 2.8: Synchrotron-based far-infrared ellipsometry setups (a) at the ANKA facility, Karlsruhe, Germany [49] and (b) at the NSLS, Brookhaven National Laboratory, USA [50]. Both setups employ Fourier-Transform Michelson-interferometers as wave length differentiating devices.

of the Michelson-interferometer geometry as the wavelength differentiating device, which are attached to home-built photometric ellipsometer arrangements, embodying the optical components for setting and analyzing the polarization state of the light. The radiation is typically detected by a helium-cooled bolometer system.

To cover a broad spectral range, we use different light sources. A tungsten filament is used in the near-infrared (NIR) region, a standard glowbar (SiC spiral) in the mid-infrared (MIR) and in the far-infrared (FIR) spectral range typically synchrotron radiation is preferred over the standard FTS mercury arc lamp. Synchrotron radiation provides high brilliance about 1000 times higher than the internal glowbar source making measurements on small single crystals, i.e. lateral dimensions below 1 mm possible.

The radiation from the light source enters the Michelson interferometer, its intensity is modulated due the interference of the two beams coming from the two arms of the interferometer depending on the current position of the moving mirror and then enters the ellipsometer unit. The polarization state is set and analyzed by either an wire grid polarizer, i.e. a mesh of thin metallic stripes evaporated onto on a suitable substrate, or a Glan-Taylor-prism polarizer made of YVO_3 (NIR range). In the FIR (10 meV to 90 meV) the metallic strips are evaporated onto a thin Mylar-foil, while in the MIR range (60 meV to 450 meV) a solid KRS-5 crystal is used as a substrate. Since the degree of polarization is extremely crucial for the precision of the measurement, in the MIR range we use "tandems" of the latter to achieve a sufficient extinction ratio of unwanted polarization better than 10^{-4}. The polarizers are mounted with the metal wire grid facing the sample to avoid possible depolarization effects when the light passes through the substrate. As described above and depicted in Fig. 2.8(a)

in the far-infrared spectral range an additional compensator can be introduced. Internal reflection in a single crystalline silicon prism induces a phase shift of about 85° to 95°.

The employment of FT-IR spectrometers requires a modified data acquisition procedure, a step-scan mode rather than a continuously rotating analyzer. Both polarizer and analyzer azimuth P and A are fixed and an entire interferogram is measured. Then, the analyzer is turned by a certain amount and the next interferogram is recorded, typically we performed 20 steps of 18° for the azimuth A. To compensate for finite offsets in the actual physical angle reading from the polarizer rotation stages we apply the calibration procedure described in detail in Ref. 51.

Variable Angle Spectroscopic Ellipsometer in the Visible and UV

We cover the spectral range extending from the NIR into the deep UV range (0.5 eV to 6.5 eV) with an Woollam Variable Angle Spectroscopic Ellipsometer (VASE). In contrast to the IR range, the spectrum is measured in the frequency domain, i.e. the desired wavelength is chosen by a set of diffraction gratings. A high-intensity xenon arc lamp works as the broad band light source in this spectral range. The quasi-monochromatic beam is transferred from the lamp housing to the ellipsometer via a fiber optical cable. Suitable linear polarizers (calcite Glan-Thompson prisms) and a rotatable retarder (a MgF_2 Berek waveplate) in between the polarizer and the sample make it possible to determine the ellipsometric angles Ψ and Δ in their full range from 0 to 90° and $-180°$ to 180°, respectively. In particular there is no lack in accuracy for Δ at its extreme values. The detector system consists of a photomultiplier tube for the UV range and a combined silicon and InGaAs photodiode system in the NIR and visible range. While the latter provide excellent performance in terms of linear response and insensitivity to polarization, the photomultiplier suffers to some extend in these respects but its sensitivity, which is required in the UV range, outclasses any other detector system.

The setup is equipped with a cold finger continuous-He-flow cryostat. The base pressure at low temperature is about $p \approx 10^{-10}$ mbar. This is required to slow down the unavoidable condensation of residual molecules, in particular water, on the sample surface at low temperatures. Ellipsometry in the UV range is susceptible to contamination of already a few atomic layers.

The crucial step of calibrating all optical components, i.e. determining the physical offsets from the reading on the scales, is done by measuring a reference sample - a doped silicon-substrate with a thermally grown SiO_2-layer (thickness $\approx$ 25 nm) on top. Since the optical properties of silicon and the oxide are precisely known all offsets and perturbations like additional phase shifts

introduced by the cryostat windows can be determined and hence corrected in the data.

Since spectra are measured in a wavelength-by-wavelength mode there is the opportunity to do dynamic scans, i.e. fixing the wavelength and recording the ellipsometric parameters as a function of an external parameter, e.g. the sample temperature, over time. For example by cycling the temperature up and down through the superconducting transition temperature T_c several times Charnukha *et al.* [42] were able to resolve relative changes in the dielectric function ε with an unprecedented precision of $\delta\varepsilon/\varepsilon \approx 10^{-4}$.

3 Iridium Oxides

3.1 Introduction: the $J_{\text{eff}} = 1/2$ ground state

Transition metal oxides (TMOs) with layered perovskite structures have been in the focus of condensed matter research for about three decades now due to their exotic physical properties, such as high-T_c superconductivity in cuprates [11], colosal magnetoresistance in manganites [12, 52], and spin and orbital ordering and fluctuations in titanates and vanadates [1]. In TMOs with $3d$ valence electrons these phenomena originate from various interactions, most important on-site Coulomb repulsion U between electrons that occupy the same orbital, hopping between different lattice sites, electron-phonon interaction, and spin-orbit coupling (SOC) which mediate among the different degrees of freedom – spin, charge, orbitals and the crystal lattice [12].

In their $5d$ counterparts, however, the electronic states near the Fermi energy exhibit larger single-electron bandwidths $W$and reduced on-site Coulomb correlations U due to the spatially more extended nature of the $5d$ orbitals [53]. Enhanced relativistic SOC, scaling in strength with the atomic number Z^4, becomes important since its energy scale (0.2 eV to 1 eV [54] compared to about 20 meV in $3d$ compounds [55]) is comparable to the reduced on-site interaction U (0.5 eV to 2 eV in $5d$ compounds [56]). The convergence and therefore competition of these energy scales in the $5d$ systems has been proposed to give rise to novel electronic phases. These include relativistic Mott insulators with an antiferromagnetic ground state, such as Sr_2IrO_4 [2, 57, 58], or two and three-dimensional spin liquids on geometrically frustrated lattices, such as A_2IrO_3 (A = Li, Na) [59–63] and $Na_4Ir_3O_8$ [3], respectively, to name just a few.

Transition metal oxides based on the $5d$ element iridium and in particular the Ruddlesden-Popper series of $Sr_{n+1}Ir_nO_{3n+1}$, where two-dimensional perovskite layers of $SrIrO_3$ are interleaved with cations, might be seen as one of the prime examples for $5d$ TMOs, since they express directly the competition of different interaction channels. Its unexpected exotic insulating ground state and striking resemblance of the high-T_c parent compound La_2CuO_4 with respect to its structural and magnetic properties has brought Sr_2IrO_4 to the forefront of current research in the field. Thus for the time being we will take Sr_2IrO_4 as an instructive example to work out the origin of its insulating ground state.

In the layered perovskite structure [64] of Sr_2IrO_4 iridium has an Ir^{4+} oxidation state, i.e. Ir adopts a $5d^5$ valence configuration. In a simplified picture of a

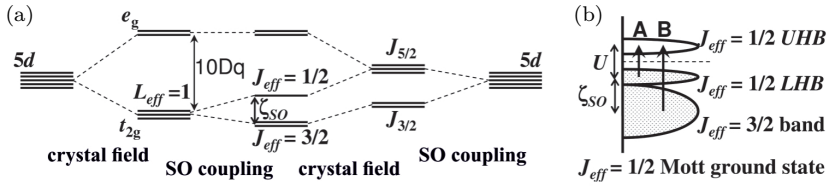

Figure 3.1: (a) Band splitting of the five $5d$ states in Sr_2IrO_4 due to crystal fields ($\sim Dq$) and spin-orbit coupling ($\sim \zeta_{\mathrm{SO}}$). (b) Even small on-site Coulomb repulsion U is sufficient to split the narrow $J_{\mathrm{eff}} = 1/2$ into upper (UHB) and lower Hubbard band (LHB) creating a Mott insulating ground state and allowing for optical interband transitions α and β. After Ref. 2.

half-filled band neglecting all electronic interactions one would expect strongly metallic behavior. This case is depicted at both ends of a schematic of the $5d$ energy levels in Fig. 3.1(a) which will serve as starting points as we elaborate on the electronic interactions at play.

In the next step we want to add electronic interactions to our considerations but already here our options which interaction to consider first are twofold. On one hand even for cubic symmetry the surrounding oxygen atoms arranged in a octahedron will energetically disfavor the two d-orbitals pointing in their direction ($d_{x^2-y^2}$, d_{z^2}). This splits the five d orbitals (actually ten due to the spin degree of freedom) in two sets, triply degenerate $t_{2g}(d_{xy}, d_{yz}, d_{zx})$ and doubly degenerate $e_g(d_{x^2-y^2}, d_{z^2})$ orbitals (left branch of Fig. 3.1(a)). The crystal field effects are typically of the order of several eV and hence the leading correction term. On the other hand, approaching the situation from the opposite site, in $5d$ systems the energy scale of the relativistic SOC is strongly enhanced to have comparable strength. SOC stems from the coupling of angular momentum L and spin S (which follows naturally from Dirac's equation) and contributes as

$$H_{\mathrm{SOC}} = \zeta_{\mathrm{SO}}\, L \cdot S \tag{3.1}$$

to the Hamiltonian of the system [65]. The parameter ζ_{SO} accounts for the SO coupling strength.

As long as ζ_{SO} is small (e.g. in $3d$ TMOs) the angular momentum l and spin s as well as their projections m_l and m_s can still be considered as good quantum numbers – the respective corresponding operators commute with the full Hamiltonian H – and SOC can be treated as a small perturbation. In the strong SOC limit, however, where ζ_{SO} is sufficiently large this description breaks down. Fortunately, we can define a total angular momentum $J = L + S$ with new good quantum numbers j and m_j. Since this is a vector sum, j can take the values $|l - s|$ to $|l + s|$ [65]. In our case the d states ($l = 2$) consequently

split into two sets, a $j = 5/2$ sextet and four with $j = 3/2$, where the latter are energetically favored [right branch of Fig. 3.1(a)].

Now, we can merge both approaches and consider the respectively other interaction in addition. We arrive at the situation shown in the center of Fig. 3.1(a). Coming from the crystal field splitting scenario, while the e_g states are basically not affected, apart from a small shift in energy, the t_{2g} bands split into two sets according to their new effective magnetic moments, a $J_{\text{eff}} = 1/2$ doublet and $J_{\text{eff}} = 3/2$ quartet. The $J_{\text{eff}} = 1/2$ state is higher in energy since it formally descends from the $j = 5/2$ sextet of the purely SOC picture. Projecting the J_{eff} states back onto their $j = 5/2$ and $j = 3/2$ ancestors due to symmetry considerations one finds $J_{\text{eff}} = 1/2$ to be of pure $j = 5/2$ origin, while for the others a small intermixing of $j = 5/2$ and $j = 3/2$ can occur. The degree of mixing depends ultimately on the spin-orbit coupling strength ζ_{SO} relative to possible crystal field assymetries, such as a tetragonal distortion of the cubic symmetry.

With the $5d^5$ electron configuration in Ir the $J_{\text{eff}} = 3/2$ subset is fully occupied leaving a single electron in the $J_{\text{eff}} = 1/2$ band. The system is accordingly reduced to an effective $J_{\text{eff}} = 1/2$ single band but still metallic due to the $m_{j,\text{eff}} = \pm 1/2$ degeneracy. The $J_{\text{eff}} = 1/2$ wavefunction to describe this state comprises of equal contributions from all three ionic t_{2g} bands [2]:

$$\left| J_{\text{eff}} = \frac{1}{2}, m_{J_{\text{eff}}} = \pm\frac{1}{2} \right\rangle = \frac{1}{\sqrt{3}} \left(|yz, \pm\sigma\rangle \mp \mathrm{i}\, |zx, \pm\sigma\rangle \mp |xy, \mp\sigma\rangle \right) \tag{3.2}$$

where σ denotes the electronic spin state. Not only are the equal contributions from all three t_{2g} states intertwined by a certain phase complex relation but also the mixing of both up and down spin states suggests emergence of unusual properties.

At this point the on-site Coulomb repulsion U comes into play. Since the $J_{\text{eff}} = 1/2$ state has a small bandwidth already a small value of U is sufficient to lift the degeneracy and open up a Mott gap at the Fermi level which splits the $J_{\text{eff}} = 1/2$ band into the upper and lower Hubbard band [Fig. 3.1(b)]. We finally arrive at the insulating state as confirmed by *dc* transport measurements and optical spectroscopy [64, 66, 67].

The Ruddlesden-Poppper series of $Sr_{n+1}Ir_nO_{3n+1}$ illustrates how the crystal structure itself can influence this interplay of interactions with comparable energy scales. Figure 3.2(a) depicts the crystal structures for different family members where n denotes the number of $SrIrO_3$ layers per unit cell between extra layers of SrO stacked along the crystallographic c-axis. The immediate consequences of this alteration in the stacking sequence on the low energy band structure are qualitatively outlined in Fig. 3.2(b). As discussed above, in $Sr_2IrO_4$the on-site Coulomb repulsion U is sufficiently strong and the half-filled

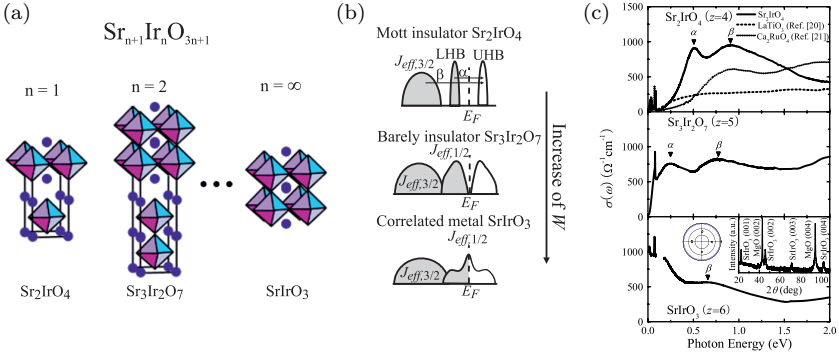

Figure 3.2: Ruddlesden-Popper series $Sr_{n+1}I_nO_{3n+1}$. (a) The crystal structure, (b) schematic band structure of the t_{2g}-bands with $5d^5$ configuration and (c) optical in-plane conductivity σ_1 of the most prominent members of the series $n = 1$, 2 and ∞. With increasing band width W the Hubbard-gap present in Sr_2IrO_4 closes and the system becomes metallic ($SrIrO_3$). α and β denote optical transitions from the lower Hubbard band and the $J_{\text{eff}} = 3/2$ into the upper Hubbard band, respectively. Panel (a) adapted from Ref. [68] and panels (b,c) from Ref. [67].

$J_{\text{eff}} = 1/2$ band is well separated into the upper and lower Hubbard band, giving rise to a direct optical gap of about 0.4 eV [67]. With increasing n the uniaxial anisotropy reduces and the bandwidth W in the $J_{\text{eff}} = 1/2$ band increases. While $Sr_3Ir_2O_7$ is still insulating the Mott gap eventually closes leading to a metallic response in $SrIrO_3$ as seen by optical spectroscopy [Fig. 3.2(c)] [67]. The interband transitions into the upper Hubbard band from the $J_{\text{eff}} = 3/2$ states (β) and the lower Hubbard band (α), respectively, can be detected and traced in the optical conductivity as a function of n. As the bandwidth W increases the peak-energies of the two transitions continuously shift to lower energies where α merges with the metallic Drude-like response.

As evidence from this discussion the evolution of anisotropy in the series of $Sr_{n+1}I_nO_{3n+1}$ plays a crucial role in the metal-to-insulator transition and evolution of the novel $J_{\text{eff}} = 1/2$ electronic ground state. Since optical spectroscopy directly assesses the low energy electronic band structure ellipsometry can be a versatile tool to gain more insight on the effects and evolution of the anisotropy. Along this line in the following section 3.2 we take the first step and determine both the full ab-plane and c-axis optical response in Sr_2IrO_4 in particular the full spectrum of infrared active phonons. Thereby we observe a strong uniaxial optical anisotropy which we are able to reconcile in the framework of fully relativistic LSDA+U electronic band structure calculations in terms of vanishing dipole matrix elements for light polarization along the c-axis.

With our enhanced understanding of the electronic structure from Fig. 3.1

we go on and explore the applicability of the $J_{\text{eff}} = 1/2$ model on even more complex $5d$ systems, e.g. those that show geometrical frustration of their magnetic moments. The recent availability of single crystals of $Na_3Ir_3O_8$ [69], a semi-metallic counterpart of Mott-insulating $Na_4Ir_3O_8$, one of the best candidates for a three-dimensional (3D) spin-liquid ground state [3, 70] due to its geometrically frustrated lattice architecture, has opened up the opportunity to discuss the issue of the metal-to-insulator transition in these materials from a new perspective. Despite the prominent role of the electron-phonon interaction in the physics of their $3d$-electron analogues, its influence on the electronic properties of the $5d$-electron compounds has not yet been addressed. In section 3.3 we provide evidence that conditions favorable for Fano interference are met in $Na_3Ir_3O_8$, which suggest a non-negligible electron-phonon coupling in this system.

3.2 Sr_2IrO_4

3.2.1 Physical properties

Within the family of $5d$ transition metal oxides Sr_2IrO_4 is perhaps the most prominent and hence best studied compound. As worked out above the interplay or competition of spin-orbit coupling and the crystal field effects leads to formation of a narrow electronic band characterized by its isospin $J_{\text{eff}} = 1/2$ which splits under the influence of a moderate on-site Coulomb-repulsion U into the upper and lower Hubbard band [see Fig. 3.1]. The $5d^5$ configuration of Ir entails a fully occupied low lying $J_{\text{eff}} = 3/2$ quartet and occupied lower Hubbard band and the ground state is described by Eq. 3.2 [2]. Despite finite distortions of the oxygen octahedra (e.g. tetragonal) which in principal lift the degeneracy among the three t_{2g} orbitals, the $J_{\text{eff}} = 1/2$ wave function has been found to describe the resonant x-ray scattering (RXS) spectra of Sr_2IrO_4 quite well [57]. The resonantly enhanced x-ray scattering amplitude at the Ir L_3 edge ($2p \rightarrow 5d$) contains not only information on the orbital character but also additional phase information on the composition of the constituent t_{2g}orbitals [57]. In their recent study combining DFT with dynamical mean field theory (DMFT) Zhang *et al.* [71] estimated the orbital anisotropy due to tetragonal distortion to be less than 2 %.

Beside the insulating behavior the novel $J_{\text{eff}} = 1/2$ ground state gives rise to unusual magnetic properties. The inherent intermixing of spin-up and spin-down states in the $J_{\text{eff}} = 1/2$ wave function results in a dominating orbital contribution to the localized magnetic moments in contrast to spin-only moments in $3d$ compounds [2]. The moments are coupled antiferromagnetically to their nearest neighbors leading to a checkerboard type arrangement with an ordering temperature of $T_{\text{N}} = 240\,\text{K}$. The underlying crystal structure as well as the magnetic ordering pattern of Sr_2IrO_4 are depicted in Fig. 3.3 where the red arrows denote the $J_{\text{eff}} = 1/2$ magnetic moments. Sr_2IrO_4 crystallizes in the K_2NiF_4 structure with lattice parameters $a \approx 5.49\,\text{Å}$ and $c \approx 25.83\,\text{Å}$ [64]. The structure is similar to the first cuprate superconductor $(La,Ba)_2CuO_4$ and their $4d$ counterpart Sr_2RuO_4 [72, 73]. The space-group symmetry, however, is reduced from $I4/mmm$, which is realized in Sr_2RuO_4, to $I4_1/acd$ due to a rotation of the IrO_6 octahedra about the c-axis by about $\theta = 11°$ [72]. This expands the tetragonal unit cell by a factor of $\sqrt{2}\times\sqrt{2}$ in-plane and doubles along the c-axis compared to the high symmetry structure $I4/mmm$. The magnetic moments follow closely the canting of the oxygen octahedra [57, 74, 75]. This results in a finite net in-plane magnetic moment which stacks along the c-axis in an "up-down-down-up" pattern as illustrated in Fig. 3.3(b) by the blue arrows. The correlation of octahedra rotation and canted moments indicates a strong magneto-elastic coupling which was also suggested from dc transport and mag-

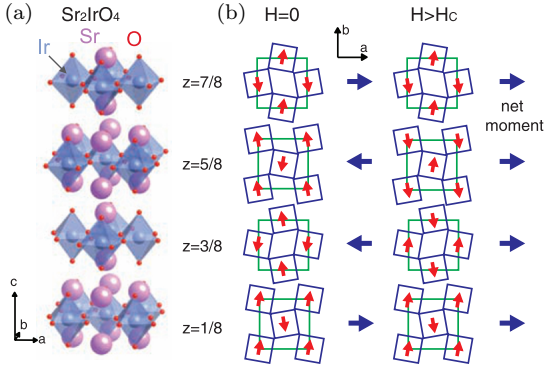

Figure 3.3: Magnetic ordering pattern of Sr_2IrO_4. (a) Layered crystal structure and (b) canted antiferromagnetic ordering of the $J_{\text{eff}} = 1/2$ magnetic moments (red arrows) of the Ir ions in different IrO_2 planes of the magnetic unit cell. Blue arrows denote the net in-plane moment of each layer, which get co-aligned in magnetic fields above the critical field $H > H_c$. Adapted from Ref. 57

netic susceptibility measurements [56, 76]. Above a critical magnetic field H_c the effective in-plane moments align along the field giving rise to the observed weak ferromagnetism [57, 64]. Two recent neutron diffraction studies [74, 75] have pinpointed the value of the ordered magnetic moment to the range of 0.2 to 0.36 μ_B consistent with various calculations [71, 77] and is drastically reduced from 1 μ_B expected in the atomic limit. This reflects the itinerancy of the Ir $5d$ states [71, 77, 78]. Moreover, the presence of additional, symmetry forbidden reflections in the neutron diffraction spectrum suggests a small orthorhombic distortion which persists well above T_N possibly providing a seed pattern for equally populated magnetic twin domains [74]. Against the background of the canted antiferromagnetism recent scanning tunneling spectroscopy (STS) [79] and time-resolved reflectivity experiments [80] supported by theoretical studies [81] have risen the question if the $J_{\text{eff}} = 1/2$ state should be described in terms of a Slater insulator (gap formation is driven by magnetic ordering) rather than a Mott insulator (driven by Coulomb interactions). Another STS study by Dai *et al.* [82], however, argues in favor of a weak Mott insulator with an increased gap size of about 0.6 eV, also showing the sensitivity of the observed spectra to various surface defects and possible contamination of the STS spectra from impurity in-gap states.

3.2.2 Experimental details

Single crystals of Sr_2IrO_4 were grown in a self flux method in the group of H. Takagi, MPI-FKF, in accordance with Ref. 64. The plate-like crystals mechanically extracted from the crucible had lateral dimensions of about $1.5 \times 2\,\mathrm{mm}^2$ in the ab-plane and a thickness less than 100 µm in c-direction. In order to gain a thickness along the c-axis that is sufficient to perform optical spectroscopy we used the following procedure. About 15 single crystals were aligned according to their crystallographic orientations using the Laue back scattering technique and were glued tightly on top of each other with a minimal amount of Ge-varnish. One side of this crystal stack was carefully polished using dry polishing papers with consecutively smaller grain size down to 0.3 µm resulting in a shiny surface. Whether this procedure was indeed successful in providing reliable access to the c-axis optical response can directly be assessed from the in- and out-of-plane phonon spectra in the far-infrared spectral range.

For an insulating material such as Sr_2IrO_4 the far-infrared optical response is dominated by the infrared active phonon resonances. The layered tetragonal structure of Sr_2IrO_4 implies an anisotropic in- and out-of-plane phonon spectrum. In case of strong anisotropy due to the grazing incidence of light the ellipsometric angles (Ψ, Δ) obtained from a certain crystal face may contain a mixture of the different tensor components – ε_a and ε_c for uniaxial materials – and a direct inversion to derive the dielectric function following Eq. 2.31 might fail. This issue becomes particularly serious wherever either component of the dielectric tensor is close or even equal to zero, e.g. at frequencies of longitudinal optical phonons in insulating materials or the (screened) plasma frequency in poor metals. For bulk materials even if strongly anisotropic the pseudo-dielectric function $\langle\varepsilon\rangle$ depends only weakly on the angle of incidence despite the usual high sensitivity of Ψ and Δ to the angle of incidence. Therefore spectra from different crystallographic faces are required from which the true dielectric functions can be extracted through a regression analysis. The reflectivity at grazing incidence in an ellipsometric measurement is mostly governed by the projection of the dielectric tensor $\hat{\varepsilon}$ onto the intersection of the plane of incidence with the sample surface. Hence in the case of uniaxial anisotropy the most advantageous crystal faces are the ones parallel to the ab-plane and ac-plane, where the former has the c-axis pointing along the aforementioned intersection of sample surface and plane of incidence. Having the spectra of the ellipsometric angles $[\Psi_j^{\mathrm{exp}}(\omega),\ \Delta_j^{\mathrm{exp}}(\omega)]$ at hand at each wavelength the figure of merit or reduced mean square error

$$\chi^2(\omega) = \sum_{j\in\text{data set}} \left(\frac{\Psi_j^{\mathrm{exp}}(\omega) - \Psi_j^{\mathrm{calc}}(\hat{\varepsilon})}{\delta\Psi_j^{\mathrm{exp}}}(\omega) \right)^2 + \left(\frac{\Delta_j^{\mathrm{exp}}(\omega) - \Delta_j^{\mathrm{calc}}(\hat{\varepsilon})}{\delta\Delta_j^{\mathrm{exp}}(\omega)} \right)^2 \quad (3.3)$$

is minimized as a function of the true dielectric tensor $\hat{\varepsilon}$. The sum over j includes all data sets from different sample faces or geometrical configurations. $\Psi^{\mathrm{calc}}(\hat{\varepsilon})$ and $\Delta^{\mathrm{calc}}(\hat{\varepsilon})$ are calculated from the appropriate Fresnel equations (2.33 to 2.35) for the anisotropic case.

3.2.3 Phonon spectra

The far-infrared spectral range (12 meV to 90 meV) for both ab-plane and c-axis response at various temperatures ranging from 10 K to 300 K is shown in Fig. 3.4(a-d). The data has been corrected for uniaxial anisotropy according to the procedure described above.

We detect sharp peak features in both the ab-plane and c-axis dielectric response, which we address to IR active phonons. First of all we note that we do not detect traces of in-plane phonon features in the out-of-plane response - particularly clearly visible around 660 cm^{-1} at the frequency of the strongest in-plane resonance. This provides evidence that the stacking approach for the ac-plane sample face was successful and that there is no significant "contamination" from the in-plane into the out-of-plane response due to misalignment of the single crystals. Correspondingly, we detect a dip or "anti-resonance" structure in the in-plane pseudo-dielectric function at 200 cm^{-1} which, as we will see later, is inherent to the uniaxial anisotropy in the dielectric response and consistent with the sharp low energy c-axis phonon at 190 cm^{-1}.

We unambiguously distinguish eight resonances in the in-plane and four in the out-of-plane dielectric response. In addition in the in-plane response another double peak structure located at 322 cm^{-1} and 337 cm^{-1} develops at low temperatures, which might be related to two additional phonons. In accordance with that in the low temperature reflectivity data reported by Moon *et al.* [83] two peaks at the same frequencies are clearly visible, but are not discussed. The inset in Fig. 3.4(a) shows a zoom in on the spectral range from 205 cm^{-1} to 280 cm^{-1} of the in-plane optical conductivity. While the two modes at 213 and 269 cm^{-1} evolve monotonously with decreasing temperature a broad hump peaking at 245 cm^{-1} rises quickly between $T = 100$ K and 50 K from a almost flat background. Due to its enhanced width and unusual temperature dependence it is unlikely to be a phonon resonance. Ge *et al.* [56] indeed observe kinks around 85 K in their magnetization and dc transport data and discuss a scenario where the magnetic moments acquire an out-of-plane component at low temperatures and might even form a spiral structure along the c-axis. However, if the peak observed here is in any way related to the magnetic structure remains so far unresolved and requires more experiments.

In order to extract the characteristic phonon parameters we fit at each resonance both real and imaginary part of the dielectric function simultaneously with a Lorentzian line shape as given in Eq. 2.7. Table 3.1 summarizes the best

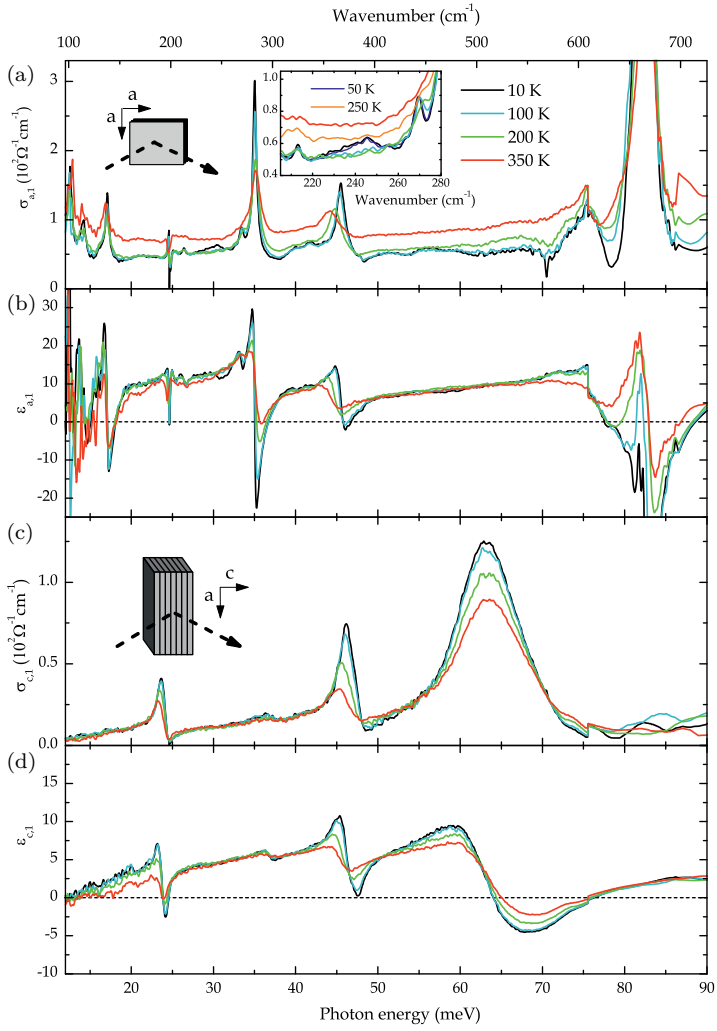

Figure 3.4: Far-infrared phonon spectra of Sr_2IrO_4. Real parts of the optical conductivity σ_1 and permittivity ε_1 for (a,b) the ab-plane and (c,d) c-axis response at various temperatures. The inset in (a): Enlarged section of the in-plane optical conductivity. The peak at 245 cm^{-1} rapidly develops only below $T = 100$ K.

Table 3.1: Best fit results for the phonon resonances in the far IR spectral range of Sr_2IrO_4 at $T = 10\,K$ with ω_j, $\Delta\varepsilon_j$, γ_j being the contribution to the static permittivity resonance frequency and line width, respectively, according to the Lorentz oscillator model. Last column shows the results from Ref. 83.

j	ω_j (cm^{-1})	$\Delta\varepsilon_j$	γ_j (cm^{-1})	ω_j (cm^{-1}) [Ref. 83]
		ab-plane		
1	101.6(1)	2.6(4)	4.4(6)	102
2	113.9(1)	2.5(4)	9.0(8)	116
3	137.7(1)	1.2(1)	4.2(2)	137
4	212.9(1)	0.05(1)	3.7(4)	
5	269.1(1)	0.08(1)	3.9(4)	
6	282.3(1)	0.72(1)	3.9(1)	284
7	322.1(2)	0.03(1)	6(1)	322
8	336.8(2)	0.10(2)	18(2)	338
9	366.9(1)	0.47(1)	10.2(2)	366
10	664(1)	1.2(3)	6(2)	663
		c-axis		
1	190.7(1)	0.49(4)	8.2(5)	
2	296(3)	0.08(5)	14(11)	
3	373.0(1)	0.47(2)	17.8(4)	
4	509.9(1)	2.13(4)	73.8(8)	

fit results for $T = 10\,K$ and compares them to the resonance frequencies obtained by Moon *et al.* [83]. All in-plane frequencies are in excellent agreement with the reported values. The weak features at $213\,cm^{-1}$ and $269\,cm^{-1}$ were either not resolved or simply overlooked so far. While the in-plane phonons exhibit a small line width γ_j, indicating a high single crystal quality, all four out-of-plane resonances are considerably broader with respect to their oscillator strength. This might be attributed to the stacking procedure of the many single crystals. Mechanical polishing as applied here can in principal induce strain effects in the surface layer which might significantly decrease the phonon lifetime [84], although the large penetration depth of FIR radiation of the order of several micrometer increases significantly the bulk sensitivity hence averaging out pure surface effects.

The temperature dependence of the resonant frequencies ω_j and corresponding line width γ_j for a representative set of in-plane and all out-of-plane modes is shown in Fig. 3.5(a-d). The resonance frequencies of the in-plane modes

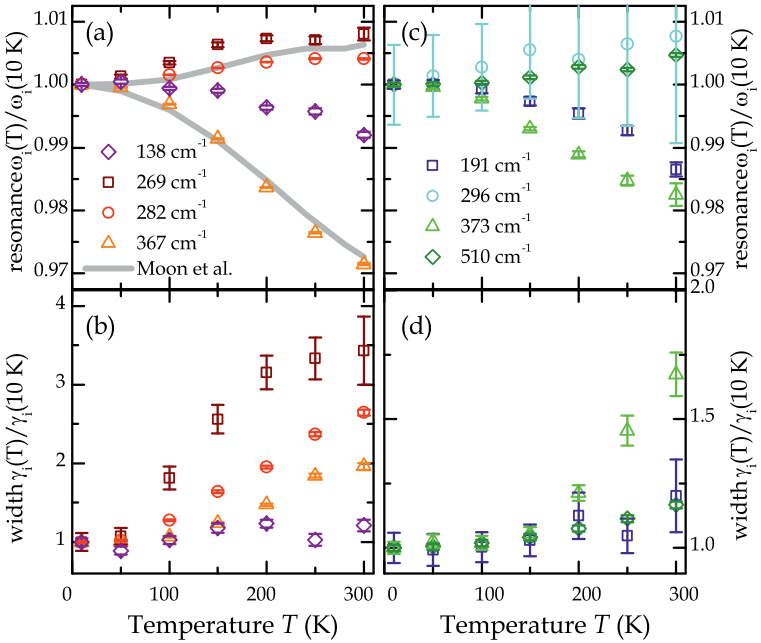

Figure 3.5: Temperature dependent phonon parameters of Sr_2IrO_4 normalized to $T = 10\,\mathrm{K}$. (a,c) Normalized resonance frequencies ω_j and (b,d) line width γ_j for ab-plane and c-axis response respectively.

reproduce the reported behavior [83] and the out-of-plane modes show qualitatively similar characteristics: a regular softening by 1.5% at 300 K of the modes at $196\,\mathrm{cm}^{-1}$ and $373\,\mathrm{cm}^{-1}$, whereas the other two exhibit a small anharmonic hardening upon heating. As expected from the already enhanced line width at low temperatures the further increase of γ_j with temperature is only moderate for the out-of-plane modes compared to their in-plane counterparts. We have checked the temperature range around the Néel temperature $T_N = 240\,\mathrm{K}$ more closely but do not find any significant changes for neither in-plane nor out-of-plane phonons indicative of structural changes or coupling to the magnetic ordering.

The in-plane phonon with the highest resonance frequency around $664\,\mathrm{cm}^{-1}$ demands some more careful analysis. As evidence from Fig. 3.4 the straight forward numerical inversion of the Fresnel equations (Eq. 2.33 and 2.34) fails to produce a Kramers-Kronig-consistent dielectric function in this spectral range.

Fig. 3.6 (a) and (b) show the ellipsometric angles $\tan\Psi$ and $\cos\Delta$, respectively, as measured for both ab-plane (circles) and c-axis (squares) orientations. Instead of performing the wavelength-by-wavelength fit we can model the optical response in both distinct experimental configurations by sets of harmonic oscillators on top of a flat background for each component of the dielectric tensor. We take the parameters from Table 3.1 which we previously obtained from Lorentz fits to the disentangled dielectric functions as a starting point for the background and add another Lorentz profile to account for the phonon at $664\,\mathrm{cm}^{-1}$ [blue lines in Fig. 3.6(c,d)]. Although the fit as indicated in panel (a) and (b) by the dotted (ab-plane) and solid (ac-plane) lines are not ideal the model is able to reproduce all essential features in the spectra. Moon *et al.* [83], however, see a much broader resonance with strongly asymmetric line shape with increased absorption on the low frequency slope in their normal incidence reflectivity spectra suggestive of multiple, closely spaced phonon resonances. While the center frequency of the phonon ω_0 is well determined by the upturn in $\cos\Delta$ right above $664\,\mathrm{cm}^{-1}$ and rather insensitive to changes in the c-axis model dielectric function the downturn in $\cos\Delta$ just below this frequency highly depends on the zero crossing in $\varepsilon_{c,1}$ and the absolute level of $\varepsilon_{c,2}$ in this spectral range. This is the reason the straight forward numerical procedure fails since all experimental uncertainties convert directly into a large deviation of the disentangled in-plane dielectric function. To conclude from this modeling approach: the value of the effective resonance frequency $\omega_{10} = 664\,\mathrm{cm}^{-1}$ is robust while the line width γ_{10} and strength $\Delta\varepsilon_{10}$ remain less well determined. The parameters obtained this way are also shown in table 3.1.

A space group analysis helps to crosscheck our result. The space group $I4_1/acd$ with the Wyckoff positions for Ir (8a), Sr (16d) and the 2 different oxygen sites (apical 16d and basal 16f) [73] allows for four A_{2u} and twelve doubly degenerated E_u infrared active phonons [85]. All modes belonging to the same irreducible representation (here either A_{2u} or E_u) are allowed to mix in order to form the eigenmodes of the ion lattice. If a irreducible representation embodies both polarizations this intermixing can in principal lead to a large number of allowed phonons in both the in-plane and out-of-plane response. The large unit cell of eight formula units, which adds up to 56 atoms per unit cell, and the reduced crystal symmetry makes a phonon calculation computationally expensive but indispensable for further insights on the lattice dynamics.

Therefore we compare our experimentally extracted phonon parameters with results from lattice dynamics calculations, courtesy of M. Höppner. The set of calculated zone center phonon frequencies is summarized in Table 3.2. The calculations predict one E_u mode at $20\,\mathrm{cm}^{-1}$ well beyond our experimentally accessible spectral range. This leaves us with eleven E_u and four A_{2u} relevant for the experimentally accessible spectral range.

Looking further into the calculated mode eigenvectors, i.e. the atomic dis-

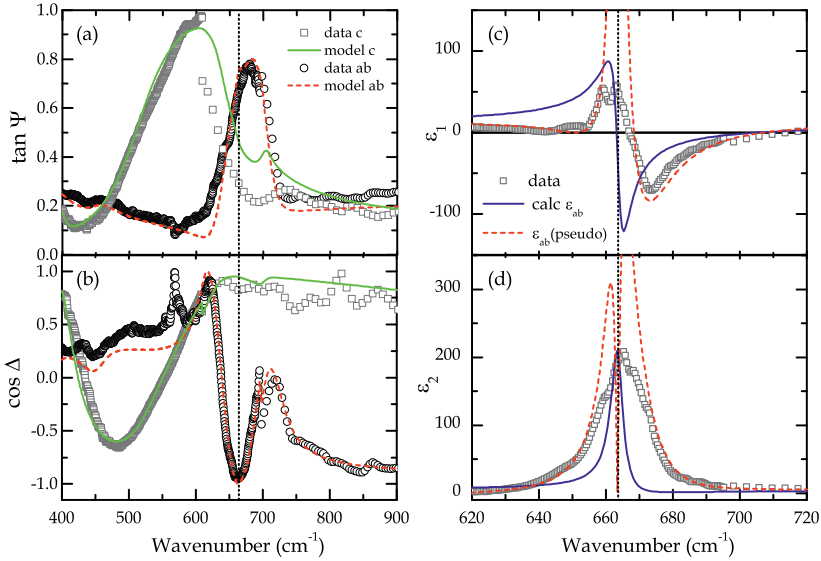

Figure 3.6: Oscillator model fit of the phonon resonance at 664 cm^{-1} at $T = 10\,\mathrm{K}$. (a,b) Ellipsometric angles tan Ψ and cos δ of the in-plane (circles) and out-of-plane (squares) response around the resonance frequency of the highest energy in-plane phonon. Dotted and solid lines denote the fit according to a multiple oscillator model for both the pure in- and out-of-plane components of the dielectric tensor, respectively. (c,d) In-plane pseudo dielectric function as resultant from in-plane Ψ and Δ data (circles) and the respective model fit (red dotted lines) by direct numerical inversion applying isotropic Fresnel equations. The blue solid lines denote the pure (disentangled) in-plane response – an harmonic oscillator at $\omega_0 = 664\,\mathrm{cm}^{-1}$ with a slight line shape asymmetry on top of a constant background.

placement patterns, we find that the set of four A_{2u} modes actually consists of three with pure c-axis polarization and one polarized in the ab-plane. The former lead to the known octahedron bending modes along the c-axis and oscillations of the IrO_6 octahedra against the Sr ions [86]; the latter involves the planar oxygen only and leads to a combined rotational, quadrupolar mode. This mode is introduced by the octahedra rotation. Thus for A_{2u} there is actually no intermixing of the in- and out-of-plane modes. In the group of the E_u modes, however, there is one normal mode originating from the planar oxygen atoms that generates a displacement in the c-direction causing a tilt or buckling of the oxygen octahedra. This mode mixes with other E_u in-plane modes which might give rise to a non-vanishing dipole moment along the c-axis for several modes. This is in contrast to the symmetric case of $I4/mmm$ where no

Table 3.2: Phonon resonance frequencies $\omega_{j,\mathrm{calc}}$ in Sr_2IrO_4 from density functional theory calculations where "ip" and "op" denote pure in- and out-of-plane polarization, respectively. Modes labeled with ip(op) are polarized predominantly in-plane and ip/op modes have non-negligible eigenvector projections in both directions. Courtesy of M. Höppner, MPI-FKF.

j	ω_j (cm^{-1})	symmetry	polarization
1	20	E_u	ip/op
2	80	E_u	ip/op
3	91	E_u	ip/op
4	122	E_u	ip (op)
5	172	A_{2u}	op
6	177	E_u	ip/op
7	185	E_u	ip (op)
8	211	E_u	ip/op
9	252	E_u	ip (op)
10	300	E_u	ip/op
11	322	E_u	op/ip
12	380	A_{2u}	op
13	444	A_{2u}	op
14	447	E_u	ip
15	651	E_u	ip
16	666	A_{2u}	ip

intermixing takes place and the two polarizations are strictly distinct. In our experimental data, however, we find in total only four out-of-plane resonances suggestive of only a weak or even absent out-of-plane dipole moment in all but one E_u phonon modes.

Although the overall energy scale matches perfectly (both calculation and experiment see the highest phonon frequency around $664\,\mathrm{cm}^{-1}$) and some groups of phonons are reasonably well reproduced, such as the three modes just above $100\,\mathrm{cm}^{-1}$, the calculations still face some difficulties. The system retains a low but finite metallicity in the DFT+DMFT calculations [71, 87] which denies the extraction of the dipole oscillator strength due to screening effects. On top of that the screening might result in a shift of certain resonance frequencies of the order of several wavenumbers to lower energies. Hence an unambiguous assignment of the in-plane modes is not yet available. A combined analysis of our infrared spectra together with Raman spectra, which have the additional capability to distinguish certain mode symmetries but are not conclusive so far [88], have the chance to resolve this issue.

In summary the far-infrared phonon spectrum is consistent with group symmetry considerations and lattice dynamics calculations. The well distinct in- and out-of-plane spectra proof that the sample stack can be considered as a quasi-single domain in terms of its optical response, which allows us to go on and examine the anisotropic dielectric tensor also at higher photon energies.

3.2.4 Optical anisotropy

Both the real part of the dielectric function and optical conductivity in-plane $\varepsilon_{a,1}$ and $\sigma_{a,1}$ as well as out-of-plane $\varepsilon_{c,1}$ and $\sigma_{c,1}$ in the photon energy range from 0.01 eV to 6.5 eV is shown in Fig. 3.7(a-d). The spectra were corrected for uniaxial anisotropy in the sense described which introduces only weak corrections.

First, we will focus on the in-plane response at photon energies up to 6.5 eV. The measured spectra agree very well with the spectra previously reported by Moon *et al.* [83] in the spectral range up to 2 eV. We assign the low energy interband transitions accordingly as α and β. Above 2 eV we find strong absorption setting in due to interband transitions with a plateau like feature around 3 eV and further rising at higher photon energies with another shoulder around 5.5 eV.

Following Fermi's golden rule one finds the following frequency dependence of the absorption coefficient $\alpha(\omega)$ in the vicinity of an direct optical gap Δ_{dir} [89]:

$$\begin{aligned} &\text{for } \hbar\omega < \Delta_{\mathrm{dir}} : \alpha_{\mathrm{dir}}(\omega) = 0\,, \\ &\text{for } \hbar\omega \geq \Delta_{\mathrm{dir}} : \alpha_{\mathrm{dir}}(\omega) \propto \left[\hbar\omega - \Delta_{\mathrm{dir}}\right]^{1/2}. \end{aligned} \tag{3.4}$$

Hence when $\alpha^2_{\mathrm{dir}}(\omega) \propto (\varepsilon_2 \cdot \omega^2)^2$ is plotted versus the photon energy ω, the direct band gap is obtained by the intersection of the fitted straight line and the energy axis. From the α band edge we determine the in-plane direct optical gap as $\Delta_{\mathrm{dir}} = 0.43\,\mathrm{eV}$ at $T = 10\,\mathrm{K}$ as illustrated in the inset of Fig. 3.7(a). Size and temperature dependence of the gap are in good agreement with the reported values [83].

The out-of-plane response, however, shows remarkably different behavior. While at high photon energies the optical conductivity is almost identical to the in-plane response with very similar characteristic shoulder features around 3 and 5 eV, the two bands α and β at lower photon energies are strongly suppressed with a remaining broad hump-like finite background extending down to lowest frequencies. Phonon assisted absorption across an indirect optical gap involves essentially two processes. When the photon is absorbed an additional phonon can either be absorbed or emitted in order to fulfill energy and momentum conservation conditions. While the former strongly depends on

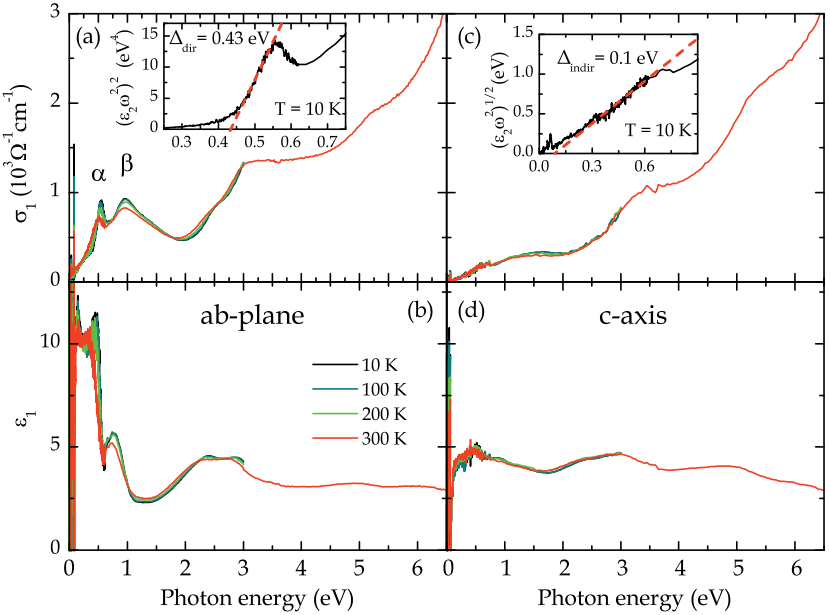

Figure 3.7: Temperature dependence of the real parts of the optical conductivity σ_1 and dielectric permittivity ε_1 of Sr_2IrO_4 in the spectral range of 0.01 eV to 6.5 eV. (a,b) ab-plane and (c,d) c-axis optical response. α and β denote the low energy interband transitions between. Insets: (a) In-plane direct optical gap $\Delta_{\mathrm{dir}} = 0.43\,\mathrm{eV}$ extracted from $(\varepsilon_2 * \omega^2)^2$, (b) c-axis optical response $(\varepsilon_2\omega^2)^{1/2}$ and indirect optical gap $\Delta_{\mathrm{indir}} \approx 0.1\,\mathrm{eV}$.

the phonon density and is therefore strongly suppressed at low temperatures, the latter is much more likely and almost temperature independent. For two parabolic bands, ε_2 follows from the relation [89]

$$\varepsilon_2 = c^{\mathrm{abs}}_{jj'}\omega^{-2}(\hbar\omega + \hbar\omega_{\mathrm{ph}} - \Delta_{\mathrm{indir}}) + c^{\mathrm{em}}_{jj'}\omega^{-2}(\hbar\omega - \hbar\omega_{\mathrm{ph}} - \Delta_{\mathrm{indir}}) \qquad (3.5)$$

which includes the matrix elements $c^{\mathrm{abs/em}}_{jj'}$ for the absorption and the emission of a phonon with energy $\hbar\omega_{\mathrm{ph}}$, respectively. Hence for indirect interband transitions the gap size can be extracted from a linear fit to $(\varepsilon_2\omega^2)^{1/2}$ at low frequencies. This way we extract an almost temperature independent indirect optical gap Δ_{indir} of about 0.1 eV as depicted in the inset of Fig. 3.7(b).

A similar trend has recently been reported on thin-films of Sr_2IrO_4 grown epitaxially in the $\langle 110\rangle$ direction on $LaSrGaO_4$ (100) substrates which also provides access to the c-axis response by normal incidence transmission [90].

Despite the fact that lattice mismatch and inevitable strain effects lead to a significant orthorhombic distortion and hence a shift in the α and β bands to lower energies the overall agreement is quite good - strong suppression of α and β followed by an upturn and shoulder around 3 eV.

In an ionic picture the origin of the optical anisotropy with respect to the α and β interband transitions might be attributed to inter-site hopping of the excited electrons since on-site d-d transitions are forbidden by the dipole selection rules [90], but this picture neglects the spatially extended nature and hybridization of the $5d$ valence states as evidence from the relatively large electronic bandwidths W realized in $5d$ TMOs. On the other hand the ground state wave function has equal contributions from all three t_{2g} orbitals intermixed and it is not obvious where the observed anisotropy emerges from. Therefore to elucidate the complex pattern of interband transitions and optical gaps we compare our experimental results with the optical conductivity from electronic band structure calculations.

Electronic band structure calculations

The calculations were performed within the local spin density approximation (LSDA) taking into account Coulomb on-site repulsion U in the presence of strong SOC. The experimental lattice parameters according to Ref. [91] were used. Since the calculated optical conductivity does not show any significant dependence on the actual spin orientation within the antiferromagnetic phase a collinear order along the c-axis was assumed in the LSDA+U calculations.

Along with the experimental data at 300 K, Fig. 3.8(a,b) presents the real parts of the calculated optical conductivity $\sigma_{1,zz}$ (out-of-plane) and $\sigma_{1,xx}$ (in-plane) in the spectral range up to 8 eV as it results from the band structure shown in Fig. 3.9(a).

Most noticeable is the large optical gap of about 2.2 eV in the c-direction [Fig. 3.8 (a)] followed by a small band centered around 3 eV and several stronger bands around 5.5 and 7 eV in rather good overall agreement with the experimentally obtained c-axis response. In the in-plane response [Fig. 3.8(b)] we identify three major features. The double peak structure at low frequencies is well reproduced, although in the calculations the lower α-band is about twice as strong as the higher β-band while in the experimental spectra the strength is approximately the same for both. Kim *et al.* [78] observe a similar trend in their microscopic model calculations when approximating only with local ionic eigenstates. This points to a interband mixing of $J_{\text{eff}} = 3/2$ and $J_{\text{eff}} = 1/2$ states and reflects the itinerancy of the system, i.e. the hybridization with neighboring oxygen $2p$ states. The next interband transition sets in around 2.2 eV concurrent with the c-axis response but at somewhat lower frequency as in the experimental spectra. From there a plateau reaches out to about 5 eV

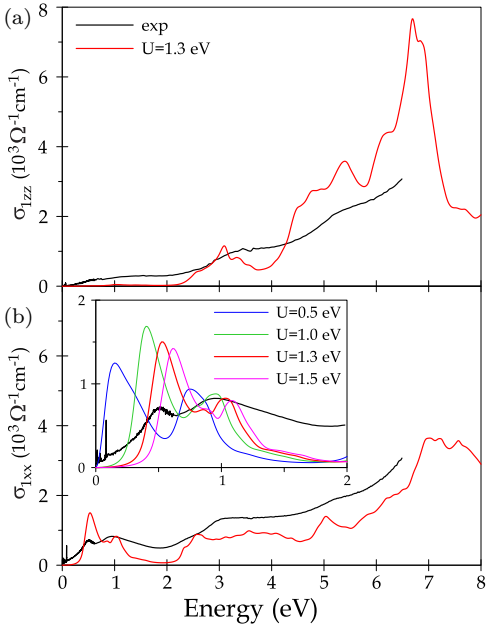

Figure 3.8: Calculated (a) out-of-plane and (b) in-plane optical conductivity $\sigma_{1,xx}$ and $\sigma_{1,zz}$, respectively, along with the experimental spectra at $T = 300\,\mathrm{K}$. Inset: Low energy in-plane double peak structure for different values of Coulomb repulsion U. $U = 1.3\,\mathrm{eV}$ is chosen to match the position of the peaks.

followed by a further rise peaking at 7 eV with approximately half the strength of the c-axis response. The weak feature around 5.2 eV seen in the experiment might find its counterpart at 5 eV in the calculation. The inset in panel 3.8(b) shows how the low energy excitation spectrum depends on the on-site repulsion U in the calculations. While the full out-of-plane response as well as the high energy part (above 2 eV) of the in-plane response shows very little variation with U (not shown) the low energy double peak structure monotonously shifts as expected to higher energies with increasing U. $U = 1.3\,\mathrm{eV}$ was found to match the peak positions of α and β the best and was therefore used in all subsequent calculations.

A more detailed analysis of the orbital character of the electronic bands and the corresponding dipole transition matrix elements allows to clarify the initial and final states of the interband transitions described above. The electronic band structure in the energy range of -8 to 8 eV together with a zoom in on the energy region around the Fermi level $[-1.5\,\mathrm{eV}, 1\,\mathrm{eV}]$ is depicted in Fig. 3.9(a) and (b), respectively. In panel (b) the bands are decorated with circles proportional in size to their orbital character projected onto the basis set of the Ir $d_{3/2}$ and $d_{5/2}$ states. As expected we find the upper Hubbard band with pure $d_{5/2}$ and hence $J_{\mathrm{eff}} = 1/2$ character well separated from the

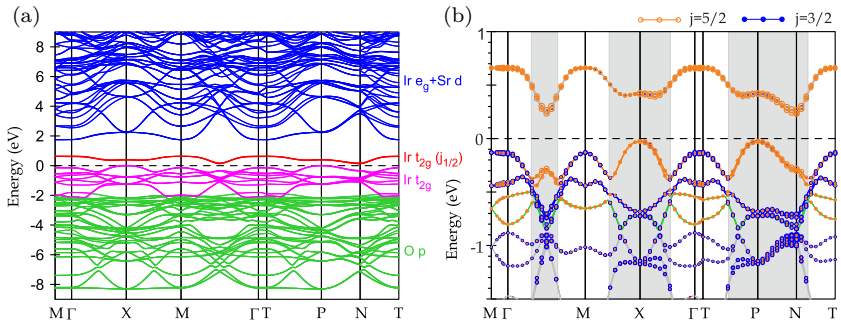

Figure 3.9: (a) Electronic band structure and respective orbital character from LSDA+U calculations with $U = 1.3\,\text{eV}$. Colors represent dominant orbital character as in the legend. (b) Enlargement of the band structure in (a). The size of the blue and orange circles is proportional to the weight of the orbital character when projected onto $d_{3/2}$ and $d_{5/2}$ states, respectively.

lower $J_{\text{eff}} = 1/2$ Hubbard band and $J_{\text{eff}} = 3/2$ states below the Fermi level [red and pink lines in Fig. 3.9(a)]. Most interesting is the origin of the low energy double-peak structure. The α band indeed stems from transitions with pure $J_{\text{eff}} = 1/2$ initial and final states but only from restricted sections of the band diagram around the zone edges at the X-point and P-N high symmetry line [gray shaded areas in Fig. 3.9(b)], which are the highest occupied states consistent with ARPES results [92]. Since U is adjusted to match the position of α and β transition the direct optical band gap is naturally found to be about 0.4 eV in the calculations – from our spectra we estimate 0.43 eV – also in very good agreement with DMFT results [71]. The β band located in spectra around 1 eV, however, is more intricate. Due to several band crossings the predominant orbital character of the highest occupied band oscillates along the high symmetry lines in the Brillouin zone. Around the Γ, T and M-points the band shows indeed significant $J_{\text{eff}} = 3/2$ character while the pure $J_{\text{eff}} = 1/2$ states reside at lower energy. Hence the β band has inherent contributions from transition with both $J_{\text{eff}} = 3/2$ and $J_{\text{eff}} = 1/2$ initial states in contrast to the previous interpretation based on a simple band picture assigning it to $J_{\text{eff}} = 3/2$ only [2]. This intermixing of the orbital character has recently been addressed within a microscopic model [78] and DMFT calculations [71]. In the former Kim *et al.* [78] link the intra-ionic $J_{\text{eff}} = 3/2 \rightarrow J_{\text{eff}} = 1/2$ transitions to a so-called "spin-orbit exciton" [93], which is also consistent with a recent RIXS study [58]. Within their model the broad electron-hole continuum originating from $J_{\text{eff}} = 1/2$ states is spread out up to 1.5 eV and mixes with the optically

forbidden spin-orbit exciton. In combination this gives rise to the double peak structure with the β peak hosting a mixture of $J_{\text{eff}} = 1/2$ and $J_{\text{eff}} = 3/2$ contributions. Kim *et al.* [78] conclude that neither a purely atomic nor a simple band picture is sufficient to describe the ground state.

More prominently, for the calculated c-axis optical conductivity we find the dipole matrix elements below 2 eV either completely vanishing as for the $J_{\text{eff}} = 1/2 \rightarrow J_{\text{eff}} = 1/2$ transitions or for $J_{\text{eff}} = 3/2 \rightarrow J_{\text{eff}} = 1/2$ to be strongly suppressed in strength by roughly two orders of magnitude compared to the in-plane response. Above 2 eV interband transitions from the low lying oxygen p states into the unoccupied $J_{\text{eff}} = 1/2$ states set in. This matches the absorption edge we find in the out-of-plane response around 2 eV.

The experimentally observed finite, hump-like background within the gap might be attributed to phonon mediated transitions across an indirect optical gap of about 0.2 eV which we find between P and N points along the Brillouin zone boundaries (see Fig. 3.9). Indirect optical transitions as second order processes are in principal beyond our calculations and hence the calculated spectra show an almost perfect band gap up to 2 eV. Similar indirect transitions could also contribute to the tail of the absorption edge in the in-plane response below 0.4 eV and the strong temperature dependent background in the far infrared spectral range.

3.2.5 Conclusions

To summarize we have determined the full uniaxial anisotropic complex dielectric function of single crystalline Sr_2IrO_4 in the spectral range from 12 meV to 6.5 eV. The uniaxial anisotropy in the infrared excitation spectrum – an indirect optical gap of about 0.1 eV followed by an direct gap of about 2 eV in the out-of-plane response together with the two-peak structure at low energies and a similar absorption edge at 2 eV in the in-plane response – is consistent with the suggested novel $J_{\text{eff}} = 1/2$ ground state within the LSDA+U band structure calculations. The temperature dependence of the phonon spectrum was analyzed in detail. Anomalous softening upon cooling and exceptional strong temperature dependencies of both in- and out-of-plane modes along with the respective mode eigenpattern provide valuable foundation for a further analysis in particular with regard to possible coupling between the electronic and lattice degrees of freedom.

3.3 $Na_3Ir_3O_8$

3.3.1 Introduction

One of the most striking manifestations of the electron-phonon interaction is the quantum interference between discrete phonons and the continuum of electron-hole excitations, which leads to asymmetric Fano resonances [27, 28] in the scattering and infrared (IR) absorption spectra of solids [94, 95]. As the electronic contribution increases the Fano resonance may undergo a change from a phonon absorption peak to a pronounced dip corresponding to reduced absorption. This dramatic behavior is one of the characteristic properties of few-layer graphene where Fano resonances have been recently observed and studied in detail [29–31, 96–99]. This elementary solid with tunable electron density has proved to be a model system to develop a microscopic theory which accounts quantitatively for the intensity and asymmetry of the Fano resonances [30, 31].

In what follows we provide evidence that conditions favorable for Fano interference are met in $Na_3Ir_3O_8$, the semi-metallic counterpart of Mott-insulating $Na_4Ir_3O_8$, one of the best candidates for a three-dimensional (3D) spin-liquid state [70]. In both $Na_3Ir_3O_8$ and $Na_4Ir_3O_8$, Ir ions are arranged on a three-dimensional geometrically frustrated Hyperkagome lattice. In formal analogy to the single-band Hubbard model [2], one refers to the $J_{\text{eff}} = 1/2$ spin-orbit 5d t_{2g} states of $Na_4Ir_3O_8$ as a half-filled narrow Mott-Hubbard band [100–106], which becomes one-third filled in semi-metallic $Na_3Ir_3O_8$. We discovered that the entire set of well-defined phonon modes in the ellipsometric IR spectra of our $Na_3Ir_3O_8$ single crystals exhibits highly asymmetric line shapes characteristic of Fano resonances. We show that with decreasing temperature a sharp increase of the Fano resonances is accompanied by concomitant changes in the underlying low-energy electronic transitions. Based on fully relativistic electronic-structure calculations in the local density approximation (LDA), we attribute this unusual behavior to Rashba-type Ir 5d t_{2g} bands intersecting near the Fermi level (resembling the Dirac cone in graphene). These bands originate from strong SOC combined with the broken inversion symmetry of the cubic lattice.

Part of the results presented in this chapter has been published in D. Pröpper *et al.*, Phys. Rev. Lett. **112**, 087401 (2014).

3.3.2 Crystal structure – the Hyperkagome lattice

Single crystals $Na_3Ir_3O_8$ of dimensions $0.3 \times 0.5 \times 0.5\,\text{mm}^3$ were grown from NaCl flux in the group of H. Takagi, MPI-FKF. For details of the growth and basic characterization we refer to Ref. 69. They crystallize in a cubic structure described by space groups $P4_132$ or $P4_332$ (No.213 and No.212 in

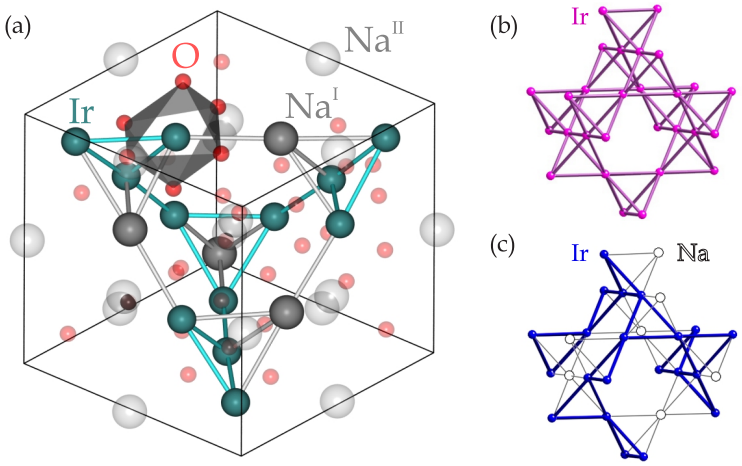

Figure 3.10: (a) Crystal structure of $Na_3Ir_3O_8$ with the space group $P4_132$. Intertwined Ir_3Na tetrahedra form a hyperkagome sublattice of Ir ions. Oxygen atoms occupy the corners of distorted octahedra around the Ir and Na^I sites. (b,c) The iridium matrix in (b) the pyrochlore $2 \times NaIr_2O_4$ and (c) the hyperkagome $2 \times Na(Na_{1/2}Ir_{3/2})O_4$ structure.

the international tables for x-ray crystallography, respectively), with 4 formula units/unit cell [see Fig. 3.10]. X-ray diffraction analysis indicates that twelve Na atoms per unit cell sit in two fully occupied nonequivalent positions marked as Na^I and Na^{II} in Fig. 3.10. This cubic structure can be regarded as a distorted modification of the face-centered cubic $2 \times NaIr_2O_4$ pyrochlore structure [Fig.3.10(b)] with space group $Fd\bar{3}m$, where a Na^I ion replaces one of the four Ir sites in the 3D pyrochlore corner-sharing tetrahedron lattice $2 \times Na(Na_{1/2}Ir_{3/2})O_4$ [Fig.3.10(c)].

3.3.3 Fano-type phonon resonances

We report a spectroscopic ellipsometry study of $Na_3Ir_3O_8$ over a wide range of temperatures (8 to 300 K) and photon energies extending from the far infrared (IR) into the visible, from 15 meV to 6 eV. The complex dielectric function, $\tilde{\varepsilon}(\omega) = \varepsilon_1(\omega) + i\varepsilon_2(\omega)$, and the related optical conductivity $\sigma_1(\omega) = \omega\varepsilon_2(\omega)/(4\pi)$, were determined by direct inversion of the Fresnel equations from the ellipsometric parameters $\Psi(\omega)$ and $\Delta(\omega)$.

Figures 3.11(a) and 3.11(b) show variation with temperature of the real part of the optical conductivity $\sigma_1(\omega)$ and permittivity $\varepsilon_1(\omega)$, respectively, in the

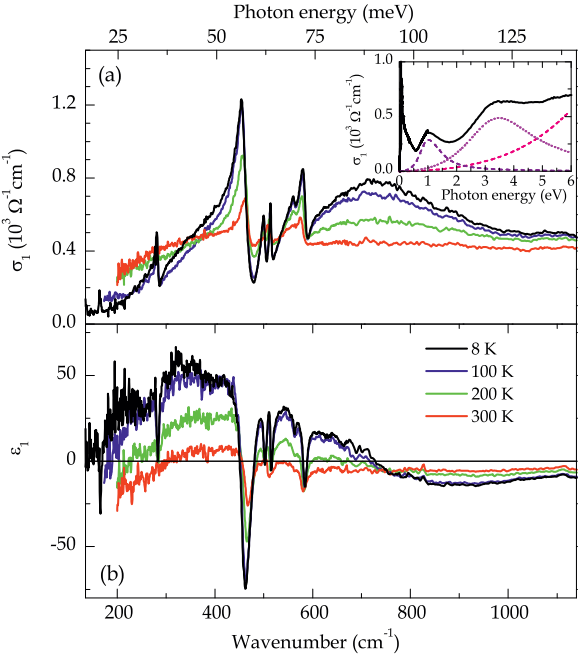

Figure 3.11: (a,b) Real part of the IR (a) conductivity $\sigma_1(\omega)$ and (b) dielectric permittivity $\varepsilon_1(\omega)$ at selected temperatures. Inset: Optical conductivity up to 6.5 eV at $T = 10$ K (solid line) along with the main interband contributions (dashed lines) as obtained from a dispersion analysis.

spectral range from 120 to 1200 cm^{-1} (15 to 150 meV). The low energy cut-off is determined by the sample dimensions and caused by the polarization-dependent diffraction of infrared light resulting in uncertainty in the analysis of the ellipsometric parameters [107]. In the low-T spectrum one can identify a set of seven highly asymmetric phonon modes located at 166, 281, 461, 501, 514, 562, and 583 cm^{-1}. Following the Wyckoff positions of the 56 atoms and their site symmetries in the $P4_132$ unit cell of $Na_3Ir_3O_8$ one would expect 21 triply degenerated T_1 IR-active modes [85]. Only seven of these modes are observed in the spectra. This is most likely due to insufficient strength and/or weak splitting of the four T_{1u} modes in the assumptive parent $Fd\bar{3}m$ pyrochlore structure of $NaIr_2O_4$. This is indeed supported by results from lattice dynamics calculations [87] where all resonance frequencies lie above 100 cm^{-1} and only eight out of the 21 allowed modes have a significant oscillator strength. The

observed asymmetric modes are superimposed on a hump-like absorption band centered around 728 cm^{-1} (90 meV), which grows monotonously in intensity on an almost flat background upon cooling. The downturn in ε_1 below 360 cm^{-1} (45 meV) indicates the free charge carrier response. In order to reconcile the IR and dc conductivity data [69] we introduce a narrow and weak single Drude peak with the plasma frequency $\omega_{\rm pl} \lesssim 0.2\,$eV. The corresponding effective charge carrier density $N^{\rm eff} = (2m/\pi e^2 N_{\rm Ir})(\omega_{\rm pl}^2/8) \approx 0.002$ electrons per Ir atom, where m is the free electron mass and $N_{\rm Ir} = 1.65 \times 10^{22} {\rm cm}^{-3}$ is the density of Ir atoms.

In order to quantitatively parametrize the observed highly asymmetric far-IR modes and the strongly temperature dependent electronic background, we fit a set of generalized Lorentzian oscillators according to Eq. 2.15 simultaneously to $\varepsilon_1(\omega)$ and $\varepsilon_2(\omega)$:

$$\varepsilon_1(\omega) + {\rm i}\varepsilon_2(\omega) = \varepsilon_\infty + \sum_{j=1}^{K} \frac{S_j\left(\omega_j^2 - {\rm i}\omega\beta_j\right)}{\omega_j^2 - \omega^2 - {\rm i}\omega\gamma_j} \tag{3.6}$$

with ω_j, γ_j and β_j the resonance frequency, line width, and asymmetry parameter, respectively, having dimensions of frequency and dimensionless S_j being the contribution to the static permittivity. The interband transitions at high energies contribute to the background term ε_∞. The causality of the dielectric response and Kramers–Kronig requirements over the entire spectral range are maintained by holding the condition of

$$\sum_j S_j \beta_j = 0\,. \tag{3.7}$$

Figures 3.12(a), 3.12(b) and Table 3.3 summarize the results of our dispersion analysis of the complex dielectric function measured at 8 K. The noticeable deviation of the fit of ε_1 from the data at low frequency is caused by the simplified single Drude peak description we used for the charge carrier response in this strongly coupled multi-band material. At the same time, we unambiguously identify seven phonon modes which are highly asymmetric as indicated by the large, negative $\beta_j^{\rm (ph)}$. In order to maintain the condition of Eq. (3.7) we used the same model with non-zero parameter $\beta_j^{\rm (el)}$ in Eq. (3.6) for one of the low-energy electronic bands, but with the opposite sign compensating the high energy contributions of the phonon modes. Since the SW of broad electronic transitions is large compared to the one of the phonon modes, the asymmetry parameter $\beta_j^{\rm (el)} > 0$ is relatively small and cannot be unequivocally assigned to one or another of the constituent optical bands of the electronic background. In the representative fit shown in Figs. 3.12(a) and 3.12(b) the optical band at

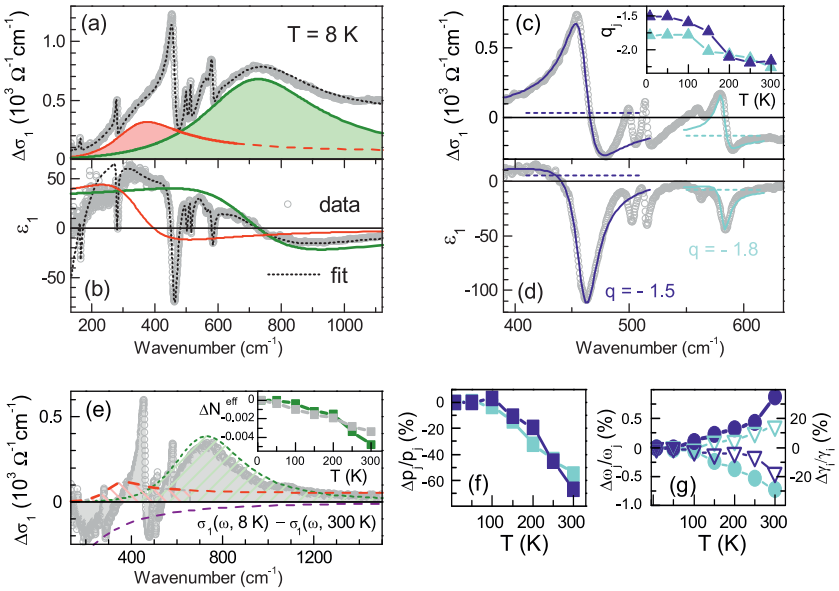

Figure 3.12: Real part of the IR (a) conductivity $\sigma_1(\omega)$ and (b) dielectric permittivity $\varepsilon_1(\omega)$ measured at $T = 8\,\mathrm{K}$ (open circles) and represented by the fit to the coupled oscillator model with Eq.(1) (dashed lines) and by the partial contribution of the low-energy electronic transitions [(a) shaded areas, (b) solid lines]. (c) and (d) Examples of the Fano fit to the spectra in the region of the phonon modes at $461\,\mathrm{cm}^{-1}$ (dark blue) and $583\,\mathrm{cm}^{-1}$ (light cyan), obtained by subtraction of an electronic background from the data in (a) and (b). Inset: Temperature dependence of the corresponding Fano coupling parameters q_j. (e) Difference spectra $\sigma_1(8\,\mathrm{K},\omega) - \sigma_1(300\,\mathrm{K},\omega)$ (open circles) represented by the changes in the separate absorption bands (dashed lines). Inset: The SW difference with increasing temperature, integrated up to 0.5 eV (light squares), along with the changes in the strength of the optical band at $728\,\mathrm{cm}^{-1}$ (90 meV) (dark squares) as derived from the fits. (f) and (g) Relative changes in the Fano parameters with increasing temperature: (f) strength p_j and (g) resonance frequency ω_j (solid circles) and width γ_j (open triangles) for the representative modes at $461\,\mathrm{cm}^{-1}$ (dark blue) and $583\,\mathrm{cm}^{-1}$ (light cyan).

Table 3.3: Best fit results for the Fano resonances and low energy electronic transitions in the far IR spectral range of $Na_3Ir_3O_8$ at $T = 8\,K$ with ω_j, S_j, γ_j, β_j and q_j being the contribution to the static permittivity, resonance frequency, line width and asymmetry parameters, respectively.

	j	ω_j (cm^{-1})	S_j	γ_j (cm^{-1})	β_j (cm^{-1})	q_j
(ph)	1	166	0.70	3.0	-101	-3.6
	2	281	0.56	5.0	-535	-1.7
	3	461	2.33	22.6	-1092	-1.5
	4	501	0.33	6.8	-490	-2.5
	5	514	0.27	4.3	-318	-3.5
	6	562	0.05	7.3	-400	-3.1
	7	583	0.31	8.9	-950	-1.8
(el)	1	358	36.1	249	97	7.4
	2	728	34.4	447		

$358\,cm^{-1}$ (44 meV) was selected to be asymmetric with $\beta_1^{(el)} = 97$, whereas the band at $728\,cm^{-1}$ (90 meV) was taken to be a classical Lorentz oscillator with $\beta_2^{(el)} = 0$. Some uncertainty of the phenomenological fitting procedure in the determination of the asymmetry parameter $\beta_j^{(el)}$ does not affect the parameters of the phonon modes listed in Table 3.3. In the vicinity of the resonance frequency the generalized Lorentz oscillator in Eq. (3.6) can be converted into the Fano profile resulting from the quantum interference of a discrete state with a continuum:

$$\Delta\sigma_1^j(\omega) = \sigma_0^j \frac{(q_j^2 - 1 + 2q_j\epsilon)^2}{1 + \epsilon^2},$$

where $\epsilon = 2(\omega - \omega_j)/\gamma_j$ and $(2\omega_j q_j)/(q_j^2 - 1) \approx \beta_j$ as outlined in section 2.1.2. Figure 3.12(c) and 3.12(d) illustrate exemplarily the Fano profiles for the two strongest resonances at $T = 8\,K$. Both resonances are characterized by $q \approx -1.5$ with an antisymmetric absorption line shape implying comparable phonon and electronic contributions into the Fano resonances. The temperature evolution of q_j is shown in the inset of Fig. 3.12(c) and one can see that the electron-phonon coupling weakens with increasing temperature. Figure 3.12(e) displays the changes occurring in the IR conductivity spectra with increasing temperature, as shown by the difference spectra $\Delta\sigma_1(\omega) = \sigma_1(\omega, 8\,K) - \sigma_1(\omega, 300\,K)$. By using the dispersion analysis of the dielectric function spectra at different temperatures with Eq. (3.6), we determine more accurately the temperature variation of the constituent Drude and low-energy inter-band contri-

butions shown by the dashed lines in Fig. 3.12(e). The corresponding loss of the associated SW, $\mathrm{SW}_j = \frac{\pi}{120}\Delta\varepsilon_j\omega_j^2$, with increasing temperature above 8 K is detailed in the inset of Fig. 3.12(e) for the optical band at 728 cm^{-1} (90 meV), along with the temperature dependence of the integrated SW difference, $\Delta\mathrm{SW}(T) = \int_0^{1eV}[\sigma_1(\omega,T) - \sigma_1(\omega,8\,\mathrm{K})]\mathrm{d}\omega$. In the latter case, the SW in the extrapolation region below 15 meV was determined by the procedure based on the Kramers–Kronig consistency check of the experimentally measured $\Delta\epsilon_1(\omega)$ and $\Delta\sigma_1(\omega)$, 15 meV $< \omega <$ 1 eV as discussed in section 2.1.3. The temperature-driven loss of the SW, expressed in terms of the effective number of charge carriers $\Delta N^{\mathrm{eff}}(T) = \frac{2m}{\pi e^2 N_{\mathrm{Ir}}}\Delta\mathrm{SW}$, is comparable to the free carrier density evaluated above, and it is not recovered within a high energy scale in excess of 1 eV. In order to quantify the temperature-dependent intensity of the sharp Fano resonances we refer to the strength parameter p_j [30], which accounts for its both positive and negative contributions to $\Delta\sigma_1^j(\omega)$ (approximately equal for $q_j \approx 1$): $p_j = S_j\omega_j^2(1 + 1/q_j^2)/8$. Figure 3.12(f) shows the temperature evolution of the Fano-strength parameter p_j for the two representative resonances. It appears clear from our analysis that both the intensity and Fano-asymmetry variations of the sharp resonances correlate remarkably well with the strength of the underlying electronic transitions. Therefore the SW loss of the phonon resonances stems from the SW loss of the interband transition. The observed intensity and asymmetry (Table 3.3) of the Fano resonances imply a considerable el-ph coupling in $Na_3Ir_3O_8$, given the high bonding ionicity and the large number of IR active modes with evidently large intrinsic dipole moments. This is in stark contrast to the case of graphene, where the static intrinsic dipole is negligible and similar values of the Fano parameter q [29, 96–99] originate mainly from the electronic excitations in the presence of a relatively small el-ph coupling [30]. Further evidence for the strong interaction of the phonons with the underlying electronic transitions in $Na_3Ir_3O_8$ is the temperature dependence of the resonance frequency and width of the strongest mode at 461 cm^{-1} (dark solid circles and open triangles in Fig. 3.12(g), respectively), which hardens and narrows with increasing temperature. A quantitative estimate of the el-ph coupling constants and the Born effective charges requires a detailed analysis of the lattice dynamics in this complex Hyperkagome structure, which is an important challenge for future theoretical work.

Yet, we can still go one step further and use the Green's function formalism as described in section 2.1.2 in order to shed some more light on the interaction of the phonons with the electronic background and give an estimate at least of the order of magnitude for the el-ph coupling constant $\lambda_{\mathrm{e,ph}}$. However, since the electronic background has a non-trivial frequency dependence – two humps lying below and above the main set of phonons between 400 and 600 cm^{-1} – which represent interband transitions between initial and final states of very

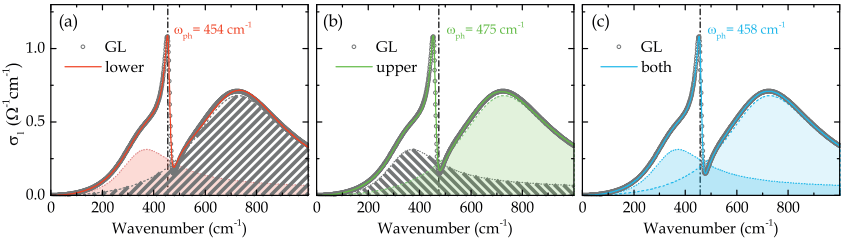

Figure 3.13: Remodeling with the Green's function formalism for coupled oscillators. Grey dots denote the generalized oscillator model according to the values in Table 3.3. (a) The red, solid line denotes pure coupling to the lower el. band (red shaded area) – the gray shaded oscillator is not coupled to the phonon, (b) the green line represents only coupling to the upper band (green shaded area), and (c) blue, solid line shows the fit to both background oscillators with the same coupling parameter g according to Eq. 3.8. The vertical dashed lines denote the bare phonon frequencies ω_{ph} obtained from the respective fits.

different orbital character and hence we cannot determine which phonon couples to which electronic excitation and how strong, we have to make certain restrictions and assumptions in order to arrive at meaningful results. Therefore we will consider only a subsystem consisting of the two Lorentzians given in table 3.3 for the background and the strongest resonance at $\omega_3 = 461\,\mathrm{cm}^{-1}$ with the strongest asymmetry of $q_3 \approx -1.5$ and anomalous temperature dependence as a representative of the other resonances. The relative shift in the phonon frequency $\Delta\omega$ with respect to its bare resonance frequency ω_0 will serve as a measure of the coupling strength and reads [35]:

$$\lambda_{\mathrm{e-ph}} = \frac{\Delta\omega}{\omega_0} \approx \frac{\frac{1}{2}g_{3,j}^2\left(\omega_{\mathrm{el},j}^2 - \omega_j^2\right)}{\left(\omega_{\mathrm{el},j}^2 - \omega_3^2\right)^2 + (\gamma_{\mathrm{el},j}\omega_1)^2} \tag{3.8}$$

where the parameters $\omega_{el,j}$ and $\gamma_{el,j}$ characterize the electronic bands to which the phonon couples with the coupling parameter $g_{3,j}$ as defined in Eq. 2.20. Since we neglect all other phonons we have to adjust the asymmetry $\beta_{\mathrm{el},1} = \beta_3 S_3/S_{\mathrm{el},1}$ which we had introduced before for the lower interband transition to maintain Eq. 2.17. This condition is already covered within the Green's function approach since we use the full frequency dependence. To determine the shift of the phonon resonance we consider three different extreme scenarios: (a) coupling only to the lower band with strength g_{low} ($g_{\mathrm{up}} = 0$), (b) coupling purely to the upper band g_{up} ($g_{\mathrm{low}} = 0$), which seems more natural due to the strong correlations in the temperature dependence of the amplitudes, and (c) coupling to both with the same strength $g = g_{\mathrm{low}} = g_{\mathrm{up}}$. The results are shown in Fig. 3.13 and the obtained parameters are summarized in table 3.4.

Table 3.4: Coupling parameters from the Green's function approach with ω_0 the bare phonon, g_{low} and g_{up} the coupling parameter and the relative frequency shift $\lambda^{\mathrm{low}}_{\mathrm{e-ph}}$, $\lambda^{\mathrm{up}}_{\mathrm{e-ph}}$ of the lower and upper interband transitions, respectively.

		ω_{ph} (cm^{-1})	g_{low} (cm^{-1})	g_{up} (cm^{-1})	$\lambda^{\mathrm{low}}_{\mathrm{e-ph}}$	$\lambda^{\mathrm{up}}_{\mathrm{e-ph}}$
(i)	lower	454	-88		0.011	
(ii)	upper	475		-168		0.031
(iii)	both	458	-70	-70	0.010	0.0006

Within this scheme (ii) results in the largest relative shift of about 3 %, where the other two scenarios give results in shift of about 1 %. Although these values suggest a non-negligible electron-phonon interaction, one has to be cautious since this Green's function formalism remains a phenomenological parametrization. While phonons are generally well described by a coherent resonance due to their small width the broad humps representing the interband transitions are certainly too approximate to make quantitative conclusions. Hence the previous statement that detailed theoretical treatment is required still holds.

Insights from LDA

We take the first step in this direction by identifying the origin of the electronic bands coupled to the phonons and performed relativistic LDA band structure calculations using the linear muffin-tin orbital method [108, 109] for the experimental crystal structure of $Na_3Ir_3O_8$ [69].

Although the IrO_6 octahedra are distorted, the Ir d shell is split into well separated t_{2g} and e_g states. A simple electron count shows that the t_{2g} states of each Ir are filled by 4.67 electrons. In spite of the non-integer valency of an $Ir^{4.33+}$ ion scalar-relativistic calculations which neglect SOC give an insulating solution with 8 unoccupied bands separated by a gap of $\sim$ 0.2 eV from the remaining occupied t_{2g} bands as illustrated in Fig. 3.14(a).

Since the crystal structure lacks inversion symmetry the Kramers degeneracy is lifted everywhere except for time-reversal invariant points. A striking effect of strong SOC is that a pair of unoccupied t_{2g} bands closes the gap [green lines in Fig. 3.14(b)] and creates two large electron-like Fermi surfaces around the R point. The charge balance is then maintained by depopulating hole-like bands near Γ [red lines in Fig. 3.14(b)] rendering the material semimetallic, with a negative indirect band gap between Γ and R. In semi-metallic materials strong temperature effects in the optical spectra are expected [110]. As temperature increases the phonon assistance of the indirect transitions is dramatically enhanced, which changes the valence and conduction band oc-

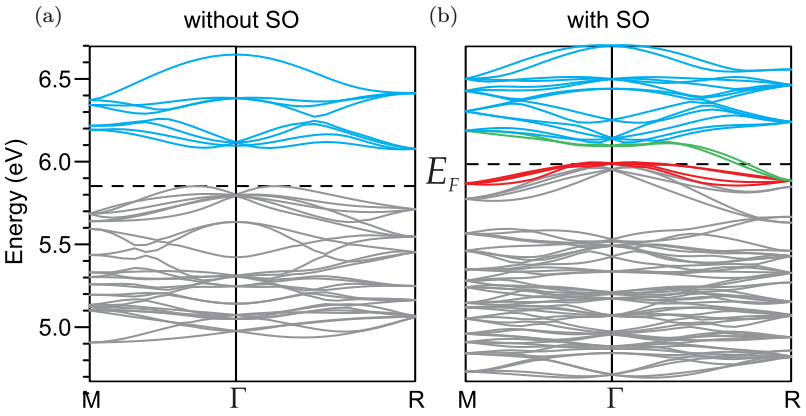

Figure 3.14: Electronic band structure as obtained from LDA calculations (a) neglecting SOC: the unoccupied states (blue) are separated from the occupied (gray) by a gap of about 0.2 eV. (b) When SOC is included one band (green) crosses the Fermi level lowering the chemical potential. The system becomes semi-metallic with hole-like Fermi surface pockets around Γ (red) and large electron-like pockets at R (green and red).

cupancies at the R and Γ points, respectively. This may explain the observed temperature evolution of the low energy electronic background with its spectral weight redistribution over an extended energy range.

This drastic impact of SOC on the electronic band structure around the Fermi level is directly reflected in the low energy IR excitation spectrum. Fully relativistic Ir t_{2g} bands decorated with circles proportional to the weight of Ir $d_{3/2}$ and $d_{5/2}$ states are shown in Fig. 3.15(c). The relativistic t_{2g} bands are subdivided into a lower- and a higher-energy group reflecting the splitting of Ir t_{2g} states into a quartet with $J_{\text{eff}} = 3/2$ and a doublet with $J_{\text{eff}} = 1/2$. As compared to $Na_4Ir_3O_8$ [100–106] the filling of the $J_{\text{eff}} = 1/2$ states is significantly reduced from one-half to one-third and therefore one would expect that the renormalization of the Ir t_{2g}-derived bands due to correlation effects is strongly suppressed. As the functions of the $J_{\text{eff}} = 1/2$ doublet are given by linear combinations of $d_{5/2}$ states only, the appreciable contribution of $d_{3/2}$ states to unoccupied t_{2g} bands [Fig. 3.15(c)] implies a strong hybridization between the $J_{\text{eff}} = 3/2$ and $J_{\text{eff}} = 1/2$ states – in stark contrast to Sr_2IrO_4. The multiplet of closely spaced occupied and unoccupied states around the Γ point give rise to strong interband transitions. These transitions are responsible for a peak of the optical conductivity below 0.1 eV shaded by red in Fig. 3.15(b).

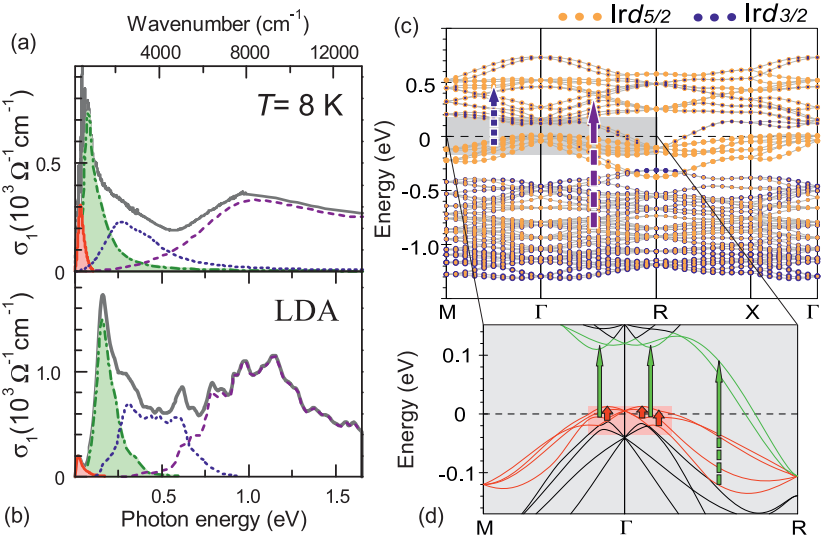

Figure 3.15: (a) $\sigma_1(\omega)$ of $Na_3Ir_3O_8$ measured at $T = 8\,K$ and contributing interband transitions determined by a dispersion analysis. (b) Corresponding relativistic LDA calculation with a breakdown into separate t_{2g} orbital contributions. (c) Band structure for Ir t_{2g} states. The size of blue and orange circles is proportional to the weight of d states with true $d_{3/2}$ and $d_{5/2}$ orbital character, respectively. (d) Enlargement of the band structure of (c). Color coding sketched with arrows in (c) and (d) corresponds to the band color in (a) and (b).

The bands crossing E_F also provide an intra-band Drude contribution to the conductivity with $\omega_{pl} = 0.6\,eV$ [not shown in Fig. 3.15(b)] which is somewhat larger than the experimentally observed value. A sharp peak at 0.2 eV (green shaded area) is due to interband transitions from occupied $J_{eff} = 1/2$ bands to the pair of bands which cross E_F near R, whereas transitions from the same initial $J_{eff} = 1/2$ bands to the rest of the unoccupied t_{2g} bands give a broad feature centered at 0.5 eV. Finally, transitions from the bands formed predominantly by $J_{eff} = 3/2$ states to unoccupied t_{2g} bands give a broad maximum of the conductivity at ∼1.2 eV. The overall shape of the optical conductivity, i.e. a strong, low lying transition followed by a near IR band peaking at about 1 eV and an absorption edge setting in between 2 and 3 eV (see inset of Fig. 3.11), is nicely captured by the calculations, although the absolute values calculated exceed the experimental ones roughly by a factor of two.

3.3.4 Conclusions

The results presented above emphasize the significance of the electron-phonon interaction in strongly spin-orbit driven systems. Because of the lack of inversion symmetry the four $J_{\text{eff}} = 1/2$ bands in $Na_3Ir_3O_8$ have linear Rashba-type dispersion in the vicinity of Γ with their apex lying slightly above E_F, similar to the bulk band structure of BiTeI [111, 112]. An analysis of the dipole matrix elements has shown that interband transitions between these partially filled bands have a high probability. This provides a high density of electron-hole excitations which interfere with superimposed discrete phonon states, in a similar manner as discussed for graphene [29, 96]. Our experiments highlight the need for a detailed analysis of the electron-phonon interaction and its influence on the ground states and low energy excitation spectra in the 5*d*-electron compounds.

4 Iron pnictides

One of the recent hot topics in the research field of correlated electron systems is the new class of iron-based high-transition-temperature superconductors. In both this new materials and the copper-oxide-based superconductors superconductivity emerges on the background of enhanced electronic correlations. As the strength of the electronic correlations has to be "just right" – if too strong a Mott transition drives the system into an insulating state, however if too weak there is not enough attraction between the electrons to form Cooper-pairs at temperatures this high – controlling this strength can provide new insights on the underlying mechanism, which is still not fully resolved. Therefore in this chapter we will explore the effect of varying the electronic correlation strength in the iron-based materials: first, substituting 3*d* Fe with isoelectronic 4*d* Ru in $BaFe_2As_2$ and second, changing the chemical composition in the series of isostructural, non-superconducting parent compounds AFe_2As_2 with A= Ca, Sr, Ba.

4.1 Introduction

The "iron age"[1] in the field of superconductivity research was initiated upon the discovery[2] of a new class of iron-based high-temperature superconductors in the group of Hideo Hosono [21]. Soon after the initial synthesis of F doped $LaFeAsO_{1-x}F_x$ [21] with a superconducting transition temperature of $T_c = 26\,K$ a plethora of new compounds with a similar crystal structure was reported with T_c as high as 56 K [114, 115] in the so called oxy-pnictides and 38 K in related potassium doped, oxygen-free $Ba_{0.6}K_{0.4}Fe_2As_2$ [116]. Not only these remarkably high transition temperatures but also their phase diagram with respect to charge doping, which is in striking similarity to the copper-oxide based high-T_c superconductors as depicted in Fig. 4.1, has stimulated tremendous excitement and research efforts since this was believed to open up a new pathway to get a deeper understanding of unconventional superconductivity in general – also in the cuprates. In both material classes superconductivity emerges in close proximity to an antiferromagnetic phase in a dome-shaped region when the magnetism is suppressed. In the iron-based compounds this can be achieved

[1] M. Johannes, Physics 1, 28 (2008)

[2] A preceding discovery of superconductivity in LaFePO with $T_c = 4\,K$ in the same group [113] did not attract much attention.

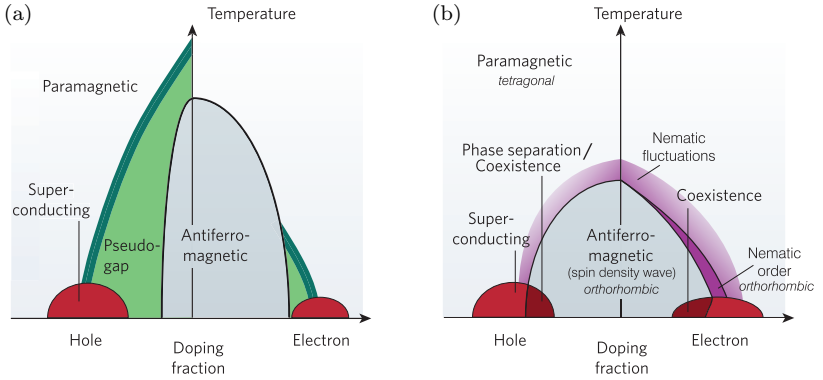

Figure 4.1: Schematic doping phase diagram of (a) cuprate and (b) iron based high-T_c superconductors. The undoped parent compounds of the cuprate superconductors are antiferromagnetic (AFM) Mott insulators. With increasing charge doping the magnetic order is suppressed until eventually the superconducting (SC) state emerges in a dome-like region. In the strongly overdoped region Fermi liquid behavior is recovered. Between AFM and SC phase the system exhibits the exotic "pseudo-gap" phase which breaks the tetragonal symmetry of the electronic phase. (b) Superconductivity in the iron pnictides emerges from a antiferromagnetic metallic phase via both electron and hole doping in a similar dome-like fashion as the cuprates. Maximal T_c is reached where the AFM phase vanishes. In the underdoped region SC and AFM ordering are found to coexist. Recent reports on detwinned single crystals disclosed a nematic ordering and associated with strong nematic fluctuations close to the antiferromagnetic phase. Adapted from [119, 120].

by different means: chemical doping and applying external pressure [117, 118]. This close proximity of antiferromagnetism and superconductivity – even microscopic coexistence in some compounds in limited doping ranges – along with a strong two-dimensionality of the electronic system induced by the underlying crystal structure are now believed to be two of the key elements to high-temperature superconductivity [22].

In the following we will introduce the basics of the iron-based superconductors; in particular their crystal structure, doping phase diagram as well as the main characteristics of their magnetic and superconducting phases and at the end with a focus on the special case of isoelectronic substitution. In the past years the solid-state research community has shown overwhelming productivity in this field. In consequence already early on several reviews both of general scope [117, 121, 122] and on selected topics, such as magnetism [123] and the superconducting state [118, 124, 125], have tried to preprocess and condense the current knowledge and input from the experimental as well as theoretical point of view. This brief review is to some extend based on these works.

4.1.1 Crystal structure

The common building block of all iron-based superconductors are quasi-two-dimensional iron pnictide (Pn, either As or P) or chalcogenide (Ch, i.e. S, Se or Te) layers. Superconductivity is found to take place in these layers in appealing analogy to the copper-oxide planes common to all members of the cuprate family [118]. As depicted in Fig. 4.2 within these layers the Fe ions are arranged in a square lattice (red spheres) and are tetrahedraly coordinated by either Pn or Ch atoms (golden spheres), which are located alternately above and below the iron plane. These layers then are stacked along the c-axis and in most compounds separated by spacer layers of different types [see Fig. 4.2]. Accordingly compounds are addressed or classified by the stoichiometric composition of their parent compounds – or hence equivalently the composition of their spacer layers between the FePn/Ch-layers. This is illustrated in Fig. 4.2 for the major, most intensively studied classes: iron chalcogenides of the *11* type without intercalating ions, *111* – with one type of alkaline metal ions (e.g.

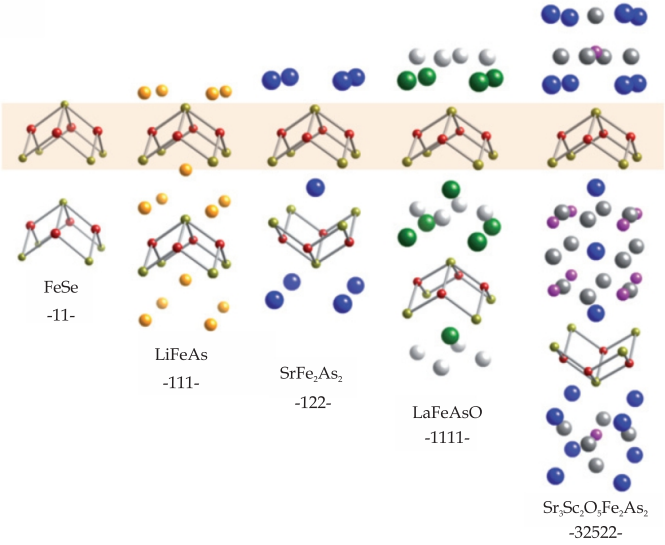

Figure 4.2: Representatives of the major subgroups of the iron-based materials. The compounds are classified by their stoichiometry. The common building block – the iron pnictide/chalgogenide layers are depicted in the shaded area. A square lattice of Fe ions is tetrahedraly coordinated by Pn/Ch ions. These layers are separated by spacer layers of a varying number of different ions. After Ref. 121

LiFeAs), *122* – with one earth alkaline ion and two iron layers per tetragonal unit cell, and *1111* – with rare earth or alkaline metal oxide interlayers as in LaFeAsO [121]. Attempting to extend the *c*-axis lattice parameter in order to increase the inter-layer spacing more subclasses (such as *-32522-*) with even larger and more complicated groups of intercalating atoms has been synthesized but no further improvement in raising the maximal T_c has been achieved so far [121, 126].

Early on, the large variety of available compounds, which on first sight differ only in their spacer layers, rose the question to what extend the maximal transition temperature T_c is related to the local structural details. It became clear that rather than the inter layer distance the tetrahedra-angle (Pn-M-Pn, Pn is the pnictogen and M the metal ion) within the FeAs-layers [Fig 4.3(a)] and the distance of the pnictogen atom above and below the Fe plane [Fig 4.3(b)] show some correlation with the maximal T_c that can be achieved in the respective materials [117, 122]. Although there seems to be no general rule T_c tends to get optimized for almost undistorted tetrahedral coordination, i.e. an angle of 109.47° and an pnictogen height above the Fe square lattice of about 1.4 Å [117].

As in this work we are dealing with the 122 family solely, often considered as prototypical for the entity of the iron-based materials, in the following we will focus on their specific properties and will point out important differences to the other classes when required in certain context.

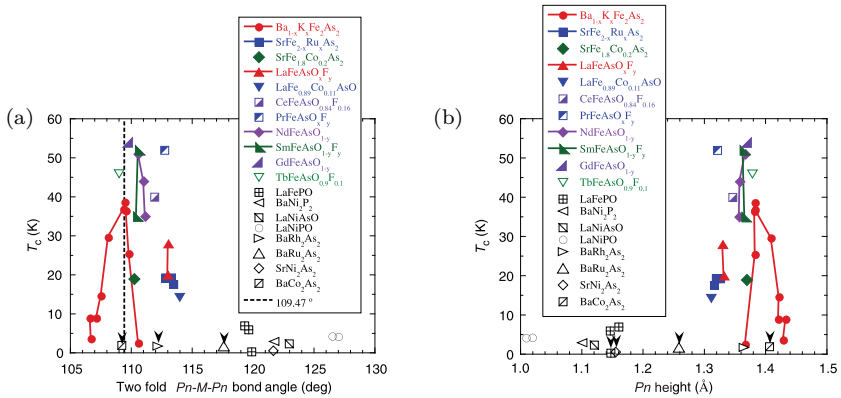

Figure 4.3: Superconducting transition temperature T_c as a function of (a) room temperature pnictogen(Pn)-metal(M)-pnictogen bond angle and (b) pnictogen height above the metal (Fe) ion layer for several compounds. The dashed vertical line in (a) denotes the undistorted MPn_4 tetrahedron angle of 109.7° [after [117]].

The undoped, non-superconducting parent compounds of the 122 family, i.e. $A\mathrm{Fe_2As_2}$ with A = Ca, Sr, Ba, all crystallize in the $\mathrm{ThCr_2Si_2}$ structure with a tetragonal symmetry of the $I4/mmm$ space group [116, 127, 128]. Upon lowering the temperature they undergo a combined structural and magnetic transition into an antiferromagnetic orthorhombic phase (F/mmm), with the orthorhombic distortion along the in-plane (1,1) direction in the tetragonal unit cell. Hence the longer a- and shorter b-axis of the orthorhombic unit cell are turned by 45° with respect to the high temperature tetragonal unit cell.

Throughout the current literature one finds a variety of reciprocal space representations which are based on crystallographic unit cells with a varying number of iron atoms. The most commonly used are pictured in Fig. 4.4. $\mathrm{Fe_2}$ denotes the primitive unit cell of the body centered tetragonal Bravais lattice [4.4(c), black lines] which corresponds to the truncated first Brillouin zone. The tetragonal $\mathrm{Fe_4}$ unit cell [4.4(a), orange lines] represents the high crystal symmetry and its larger size leads to the folded Brillouin zone. Finally, the one iron ($\mathrm{Fe_1}$) unit cell of the pure iron sub-lattice, which possesses an even higher symmetry because it neglects the staggered arrangement of the pnictogen atoms, corresponds to the larger unfolded Brillouin zone [4.4(b), green lines]. The latter is often used two describe experimental data as such from ARPES and neutron diffraction [129]. The long range magnetic order and orthorhombic distortion results in an even larger unit cell and smaller corresponding first Brillouin zone. The X-points in the corners of the $\mathrm{Fe_2}$ Brillouin zone and face centers of the unfolded $\mathrm{Fe_1}$ Brillouin zone are equivalent to the corner M points in the $\mathrm{Fe_4}$ Brillouin zone.

4.1.2 Phase diagram

In the iron-pnictides several different approaches have proven successful to suppress the antiferromagnetic phase and induce superconductivity in close proximity. In the 122 family these are: charge doping by holes (K on the A site [128, 130]) or electrons (e.g. Co or Ni for Fe [131–133]), physical/external pressure [134, 135] or isoelectronic substitution (P for As [136] or Ru for Fe[137, 138]). Although different in nature all methods produce similar results and the evolution of the different phases with respect to the external parameter can be combined in a generic phase diagram as put together in Fig. 4.1(b). Starting from the semimetallic parent compounds doping (or external pressure) suppresses quickly the combined structural antiferromagnetic SDW transition. Superconductivity emerges in a dome-shaped region when the magnetism is strongly suppressed and about to vanish. Further doping typically recovers regular Fermi liquid behavior [117]. The shaded area on the boarder of the SDW and paramagnetic phase denotes a region where the occurrence of a nematic order is discussed. In detwinned crystals in-plane anisotropy in the resistivity

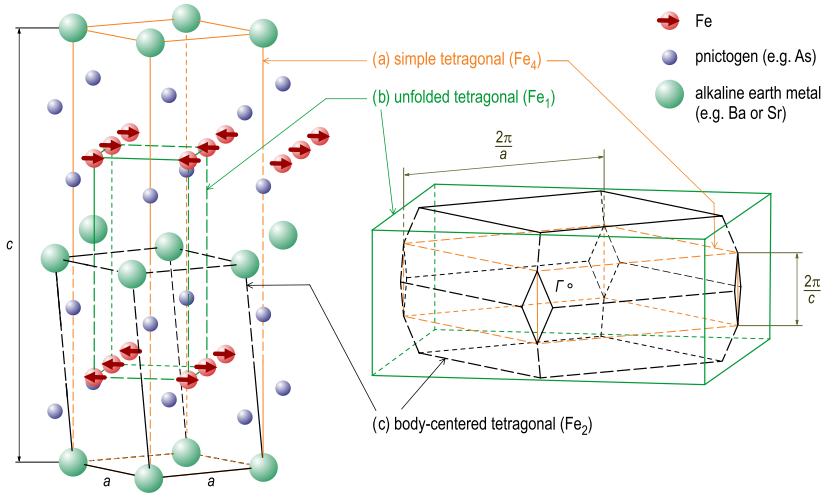

Figure 4.4: Real space unit cells and corresponding first Brillouin of the 122 iron-pnictides. (a) Tetragonal unit cell with four iron atoms per unit cell (Fe_4) and corresponding folded Brillouin zone. (b) One iron unit cell (Fe_1) of the Fe sublattice with corresponding unfolded Brillouin zone. (c) Primitive unit cell of the body-centered tetragonal Bravais lattice. Adapted from Ref. 129.

as well as optical conductivity has been observed in the SDW state which sets in already before the phase transition. This is attributed to a nematic phase, which is still paramagnetic but lowers the four-fold symmetry of the tetragonal phase to C_2. In the underdoped region of many compounds superconductivity is found to coexist with the antiferromagnetism on a microscopic scale. Phase separation, as reported early e.g. in underdoped $Ba_{1-x}K_xFe_2As_2$ [129], now seems to be due to inhomogeneities for example in the local doping concentrations and are not observed anymore in recent studies on single crystals of improved quality [139, 140]. This coexistence points out the intimate link between superconductivity and antiferromagnetism. Indeed, the superconducting dome of the transition temperatures T_c of a particular doping series peaks just where the antiferromagnetic transition temperature T_N goes to zero. Hence at zero temperature the system could undergo a second order phase transition from the antiferromagnetic directly into the superconducting phase not driven by thermal but quantum fluctuations. Such zero-temperature phase transitions are called a quantum critical point and are linked to strong modifications in the physical properties of the system also at finite temperatures. So called non-Fermi liquid behavior (indicated for example by a T-linear behavior of the

resistivity in contrast to T^2 for Fermi liquids at low temperatures) is taken as a strong indication for the existence of such a quantum critical point in the iron-pnictides hidden in the superconducting state. This linear temperature dependence has indeed been observed in both isovalently P and Ru doped $BaFe_2As_2$ [141, 142].

4.1.3 Electronic band structure

Many fundamental physical properties of a crystalline solid, such as current transport, optical absorption or photoemission spectra, can be conveniently understood in terms of their electronic band structure. Thereby the electronic bands close to the Fermi level are particularly interesting. In the iron pnictides and chalcogenides these bands are largely given by the Fe-*d* orbitals, which cross the Fermi level and establish the multi-band character inherent to all iron-based compounds. The parent compound $BaFe_2As_2$ will serve as representative example to describe the band structure characteristics of the iron pnictide and chalcogenide families. Fig. 4.5(a) shows the electronic band structure as obtained by *ab initio* LDA band structure calculations based on the crystal lattice parameters determined by means of x-ray diffraction [116]: $a = 3.9625(1)$ Å and $c = 13.0168(3)$ Å in the high temperature tetragonal phase. The color coding represents the main orbital character of these bands. In $BaFe_2As_2$ three of the Fe-*d* bands (red) with downwards dispersion, i.e. hole-like character, cross the Fermi level close to the Γ-point, whereas two electron-type bands (upwards dispersion, magenta) are found centered around the X-point in the Fe_2 unit cell. The weak coupling between adjacent FeAs layers and corresponding strong two-dimensionality of the Fe-*d* electronic subsystem is reflected in an only moderate z-dispersion of the Fermi surface sheets as illustrated in Fig. 4.5(b). The states below the Fe-*d* bands are mainly of As-*p* character (blue), whereas the states just above the Fermi level show significant hybridization of Fe-*d* and As-*p* states (green). Ba-*d* states are located > 4 eV above the Fermi level (black).

The LDA predictions described above has been probed and consistently confirmed by several experimental techniques, probably most directly by angle resolved photo emission spectroscopy (ARPES). ARPES, especially when performed with synchrotron light, has the capability to map out the entire Brillouin zone in detail (with an energy resolution as good as 1 meV to 3 meV [145]) providing access to the full momentum-energy dispersion [146]. Although ARPES is a surface sensitive technique the band structure found this way in many iron-based compounds is also consistent with the results obtained by other, more bulk sensitive probes, such as quantum oscillations or de-Haas-van-Alphen measurements, which measure extremal circumferences on the Fermi surface sheets [see Ref. 147 for a review]. The latter techniques, however, require high magnetic fields, also to suppress superconductivity since it gaps the Fermi surface,

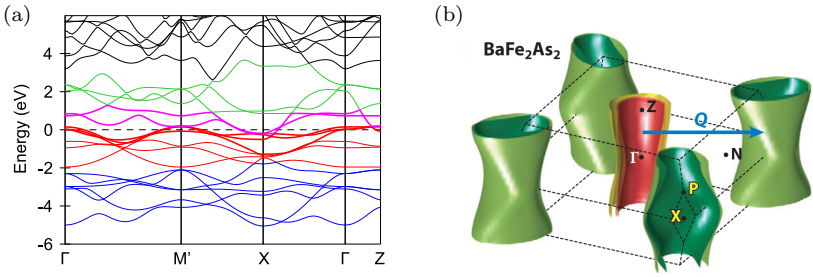

Figure 4.5: (a) Electronic band structure of $BaFe_2As_2$ as obtained from LDA calculations, courtesy of A. N. Yaresko, similar to Ref. 143 and (b) corresponding Fermi surface topology in the folded Fe_2 first Brillouin zone: three almost cylindrical hole-type sheets around the Γ-point and two electron-type barrels located at the zone boundary. Good nesting conditions (geometrical match) between the electron- and hole-type sheets is found at $Q = (\pi, \pi)$ [144].

and sufficiently clean samples. That makes these experiments in the iron-pnictides quite challenging, since heavy doping up to 50% (inevitably accompanied by disorder) is an essential control parameter to achieve superconductivity and the upper critical field H_{c2} are estimated to exceed 100 T, which is not accessible in experiments on a regular basis.

4.1.4 Magnetic properties – the antiferromagnetic ground state

The intimate link between superconductivity and the antiferromagnetic phase, as becoming evident in their microscopic coexistence in the underdoped region of the phase diagram, demands a detailed knowledge of the magnetic phase to get a full understanding of superconductivity in these materials.

In contrast to the copper-oxide superconductors, where the antiferromagnetic phase of the parent compounds is described in the framework of Mott insulators, which means localized unpaired spin-1/2 magnetic moments, the metallic ground state of the iron-based materials makes the matter more complex. The mass of experimental data from different techniques such as neutron diffraction [148–154], nuclear magnetic resonance [155, 156] or muon spin rotation [157–159], along with theoretical predictions [121, 160, 161] suggest that both itinerant and localized magnetism play an essential role. As implied by the name, magnetism is called itinerant if the magnetic moments are associate with de-localized electrons as often naturally realized in $3d$ metals with partially filled electronic bands. For strong Coulomb effects U and a large density

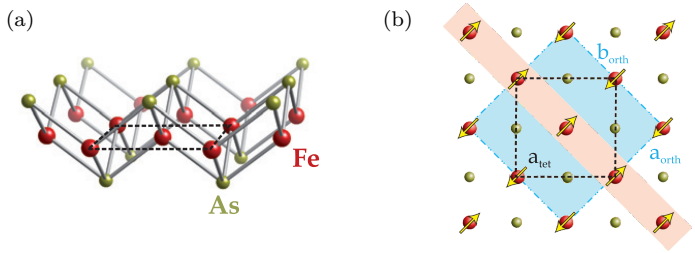

Figure 4.6: Magnetic ordering pattern of the iron-based materials (except 11 family). (a) Common FeAs layers with staggered As coordination on the left and corresponding stripe pattern along the (1,1) direction with respect to the tetragonal unit cell (black dashed lines) on the right. (b) The larger orthorhombic unit cell (blue shaded area) is turned by 45°, where $a_{\mathrm{orth}} > b_{\mathrm{orth}} \approx \sqrt{2}a_{\mathrm{tet}}$. Adapted from Ref. 121

.

of states at the Fermi level $N(E_{\mathrm{F}})$ the system has the potential to exceed the Stoner criterion (see e.g. Ref. [162])

$$UN(E_{\mathrm{F}}) \geq 1 \tag{4.1}$$

and develop spontaneous ferromagnetism due to spin-splitting of the electronic bands. Even if ferromagnetism is not realized, close to the Stoner criterion the magnetic susceptibility χ gets enhanced over the Pauli susceptibility[3] χ_{P}, approximately as:

$$\chi \approx \frac{\chi_{\mathrm{P}}}{1 - UN(E_{\mathrm{F}})} \quad . \tag{4.2}$$

The Stoner enhancement can be generalized to the momentum-dependent magnetic susceptibility χ_q:

$$\chi_q \approx \frac{\chi_q^0}{1 - \alpha\chi_q^0} \tag{4.3}$$

with the susceptibility

$$\chi_q^0 = \chi_{\mathrm{P}} f(q/2k_{\mathrm{F}}) \quad \text{and} \quad f(x) = \frac{1}{2}\left(1 + \frac{1-x^2}{2x}\log\left|\frac{x+1}{x-1}\right|\right)$$

in the case of of absent Coulomb interactions and $\alpha = U/\mu_0\mu_{\mathrm{B}}^2$. Here, μ_0 and μ_{B} are the vacuum permeability and Bohr magneton, respectively. If large sections of the Fermi surface are mapped on top of each other by the same

[3]The Pauli susceptibility χ_{P} describes the paramagnetic response of the conduction electrons due to their spin magnetic moment [162].

translation vector Q_{SDW} (called Fermi surface nesting) the bare susceptibility χ_q^0 can develop a maximum at $q = Q_{\mathrm{SDW}}$ due to enhanced particle scattering along this wave vector. In this case even small Coulomb interactions can lead to a divergence of $\chi_q(Q_{\mathrm{SDW}})$ which induces spontaneously a static, long range, spatially oscillatory magnetization, the spin-density wave, with Q_{SDW} as its propagation vector. Q_{SDW} can in principal be either commensurate (e.g. antiferromagnetic for $Q_{\mathrm{SDW}} = \pi/a$) or incommensurate with the underlying crystal structure. Opposite to that one finds the picture of electrons occupying spatially localized, atomic-like orbitals whose spin and orbital magnetic moments are not compensated other electrons in the same orbitals as for fully occupied shells.

First we recall the situation in the copper-oxides. Neutron scattering experiments on the undoped, non-superconducting parent compounds have confirmed a collinear antiferromagnetic checkerboard pattern with an in-plane ordering wave vector $(\pi/2, \pi/2)$ [123]. The strong magnetic moments associated with the unpaired valence electrons (each spin contributes $1\mu_{\mathrm{B}}$ to the total magnetic moment) lead to robust electronic correlations [163]. Superconductivity, since it requires at least some itinerant electrons which can form Cooper-pairs, is induced via doping of additional charge carriers, what concurrently suppresses the AFM state. Spin fluctuations survive in the paramagnetic state close to the phase boundary and are now strongly believed to act as the pairing glue in the Cooper-pairing [22].

On the contrary the parent compounds of the iron-pnictides are semi-metals with multiple, almost cylindrical Fermi surface sheets around the Γ-point (hole-type) and electron type sheets around the X-point in the Fe_2 reference frame. The cylindrical shape and comparable size of the pockets lead to good Fermi surface nesting conditions and hence the possibility to cause a spin-density wave instability [161, 164] very much like in pure, metallic chromium [165]. The ordering wave-vector $Q_{\mathrm{SDW}} = (\pi, \pi)$, which is commensurate with the crystal structure, is depicted as an arrow in Fig. 4.6(a). Early neutron scattering [148–154] and ^{75}As nuclear magnetic resonance experiments [155, 156] on single crystals of the parent compounds have revealed a magnetic stripe pattern, with antiferromagnetic ordering along the longer a- and ferromagnetic ordering along the shorter b-axis of the extended orthorhombic unit cell [152], which has its axes turned by 45° with respect to the tetragonal unit cell [blue shaded area in Fig. 4.6(b)]. The ordering along the c-axis is again antiferromagnetic. Itinerant magnetism is also consistent with the small observed ordered magnetic moments which vary in the range $0.1 - 1\,\mu_{\mathrm{B}}$/Fe throughout the different families compared to a magnetic moment of $3.3\,\mu_{\mathrm{B}}$/Fe in FeO where Fe has nominally the same oxidation state Fe^{2+} [117]. The SDW formation itself is well reproduced in calculations while the size of the magnetic moment is usually overestimated by roughly a factor of two [143, 160]. The magnetic moments

coming out of the early LDA calculations show strong dependence on the exact pnictogen height (as does the entire low energy band structure) [143, 166]. Combined DFT+DMFT approaches, however, have significantly improved the consistency with respect to magnetic moments and SDW induced Fermi surface reconstructions when compared to the experimental results [167].

Although the picture of itinerant magnetism seems to apply quite well to most of the members of the iron pnictide family, in particular the 122, 1111 and 111 families, Dai *et al.* [123] have pointed out several issues that are hard to reconcile within a purely itinerant picture. The 11 FeTe/Se family shows a different magnetic structure with a different ordering vector , despite the fact that the Fermi surface shows good nesting with $Q = (\pi, \pi)$ as in the other families [168]. The recently discovered 245-class with ordered Fe and Se vacancies shows strong antiferromagnetism but no nesting, since only the electron-like FS pockets are present. This material, however, is more complex since it shows (so far) inherent phase separation into layers of AFM and SC phases and the former might be necessary to even stabilize the latter [169]. Related LaFePO with a well-nested Fermi surface does not order magnetically and actually becomes superconducting below 6 K, LaFeAsO despite a very similar Fermi surface undergoes the SDW transition and remains non-superconducting down to lowest temperatures[170]. LiFeAs with $T_c = 18$ K, however, shows band renormalization by a factor of ~ 3 as other iron-based compounds but nesting is absence [171]. In all subclasses of the iron-based-materials a sizable magnetic moment is found at room temperature [172], which in the weak coupling description should only appear together with the long-range order.

In summary these observations suggest that only a combined description of itinerant and local effects can sufficiently describe the magnetic phase of the iron-based compounds and its influence on emerging superconductivity.

Investigations of the optical conductivity have been instrumental in obtaining the value of the SDW-induced energy gap and characterizing the energetics of the spin-density–wave order [173–176].

4.1.5 Superconducting properties

The similarities throughout the class of iron-based superconductors with respect to their structural, electronic as well as magnetic properties as outlined above strongly suggest a common thread for the underlying mechanism of unconventional superconductivity [22, 164]. The two main questions about the superconducting state concern on one hand the size and symmetry of the order parameter and on the other hand, but closely connected, the source of the effectively attractive interaction required in the Cooper-pair condensation. Although there is by far no consensus reached concerning the microscopic mechanism behind unconventional superconductivity in the iron-based materials,

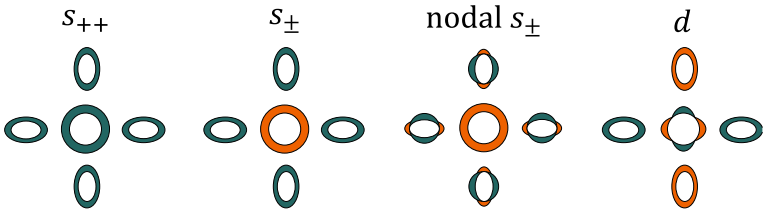

Figure 4.7: Sketches of different gap structures within the two most discussed symmetries (s- and d-wave) for a singlet order parameter in presence of the simplified, two-band tetragonal Fermi surface in the iron-based superconductors. Different colors denote opposite sign of the order parameter. From Ref. 124.

thanks to the huge amount of theoretical and experimental input, the main characteristics become more and more evident and seem to form a general picture, which applies to most compounds in the family: antiferromagnetic spin-fluctuations link orbital like sections of (nearly) nested hole and electron-like Fermi surface sheets and leads to a so-called $s\pm$ (or extended s-wave) symmetry of the order parameter, which changes sign between the sheets. AFM fluctuations are also the leading candidate for the "pairing glue" in the copper-oxide materials.

In the following we will briefly review this preliminary conclusion. Already in the beginning it was shown theoretically [177, 178] that phonon mediated interactions, characteristic of conventional superconductivity in the framework of the standard BCS theory, are far too weak to solely account for transition temperatures above 30 K. This is supported by an absence of a clear isotope effect in most compounds [118, 179, 180]. The antiferromagnetism in close proximity, however, offers spin fluctuations as an additional interaction channel [160]. Spin fluctuation mediated pairing along with the spin singlet state as established from the Knight shift in NMR experiments [181–183] demands certain restrictions on the order parameter itself. Although the direct bosonic exchange of spin fluctuations between the fermions is in principal repulsive in nature in the singlet channel[184], if the order parameter changes its sign on different parts of the Fermi surface the interaction can become overall effectively attractive [22]. For d-wave this is naturally given by the symmetry itself but in multi band materials this can also be realized by s-wave symmetry if the order parameter changes sign on different sheets of the Fermi surface, called $s\pm$ or extended s-wave pairing. The four different structures of the order parameter that has been discussed most for the iron-based superconductors are depicted in Fig. 4.7. Although d-wave symmetry does not necessarily imply nodes of the order parameter on a single Fermi surface [124], i.e. the order parameter

vanishes at well-defined k-points or lines, due to the hole-like Fermi surface cylinder around the Γ-point present in (almost all) iron-based materials d-wave symmetry is inevitably associated with nodes on the Fermi surface, while s-wave symmetry is expected to be isotropic. For $s\pm$ symmetry, however, accidental line nodes might appear due to a necessary angle dependence of the order parameter to minimize the intra-pocket repulsion caused by the spin-fluctuations [22]. These nodes, since not protected by symmetry as in the d-wave case, might be removed continuously or only appear due to details/changes in the Fermi surface topology and pair interaction [124]. This significantly complicates the distinction of the possible gap structures. Yet, the sign change in the order parameter between different Fermi surface sheets is supported by the observation of an resonance enhancement in inelastic neutron scattering experiments which occurs at the same wave vector as the magnetic ordering emphasizing the link to the antiferromagnetic SDW fluctuations [185–188].

An efficient way to address this question experimentally is ARPES with its capability to map out the Fermi-surface topology in the entire Brillouin zone and hence determine the superconducting gap structure (in particular the size), that opens around the Fermi surface when entering the superconducting state. Another approach is the temperature and magnetic field evolution of heat transport at very low temperatures. ARPES and thermal conductivity measurements has been carried out on essentially all major families and their doped relatives. While some compounds show clear indication for nodes in the gap structure (e.g. $BaFe_2(As_{1-x}P_x)_2$ [189, 190]) others were found to have a finite minimum gap value (e.g. $Ba_{1-x}K_xFe_2As_2$ [191]). This makes a d-wave gap symmetry in the iron-based superconductors unlikely – maybe except the interesting case of fully substituted KFe_2As_2, where also d-wave symmetry is discussed [192].

The symmetry of the superconducting gap in the cuprates was finally conclusively proven to be d-wave e.g. from phase sensitive superconducting interference device (SQUID) arrangements on thin films with multiple grain boundaries, where half integer flux quanta enclosed by the SQUID loop could be observed, or on single crystals with Josephson junctions at 90° to each other. The inherent multi-band nature of the iron-pnictides make these type of experiments extremely difficult to interpret and despite recent proposals for similar phase sensitive experiments [193, 194] a successful prove of the $s_\pm$ symmetry by this means is still being awaited. Nevertheless, $s_\pm$ symmetry (with or without accidental nodes) is considered so far the best or "standard" description of the order parameter symmetry and gap structure of the iron-based superconductors.

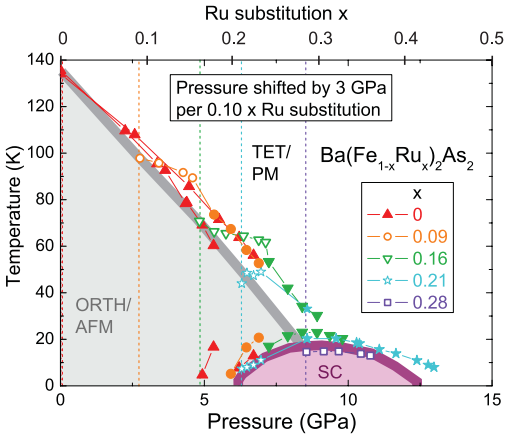

Figure 4.8: Combined pressure phase diagram of $Ba(Fe_{1-x})_2As_2$ for samples with different initial Ru content x on top of a generic phase diagram with respect to Ru substitution (shaded areas). Adapted from Ref. 197.

4.1.6 Isoelectronic substitution

As discussed in section 4.1.1, within the 122 family there a several ways to induce superconductivity: charge doping [130, 131, 195], physical pressure [134] and isoelectronic substitution [137, 138, 196]. The latter, realized by replacing 3*d* Fe by 4*d* Ru or 4*p* As by 3*p* P, is also addressed as chemical pressure because the different atomic radii of the dopants affect substantially the inter-atomic distances, their orbital hybridization and hence the low energy electronic band structure and Fermi surface topology. As expected from Ru's spatially more extended 4*d* orbitals, the chemical pressure expands the lattice along the Fe ab-planes but decreases the c-axis, leading still to an overall increase in the unit cell volume and concomitant a decrease in the pnictogen height and increase in the Fe-As bond angle [137, 138]. This is in contrast to both physical pressure and P substitution, which causes a contraction of the lattice in all directions [134, 196]. Nevertheless, Ru was found to suppress the spin-density wave state in a very similar fashion as physical pressure if the respective phase diagrams are scaled properly (10 % Ru doping is equivalent to 3 GPa [197]) as depicted in Fig.4.8. The different phases in $Ba(Fe_{1-x}Ru_x)_2As_2$ evolve slowly with increasing Ru content and superconductivity survives up to surprisingly high substitution levels ($\sim$ 40 %). Furthermore, there is no indication of phase separation nor splitting of the structural and magnetic phase transitions [198].

The isovalency has interesting consequences for the evolution of the low en-

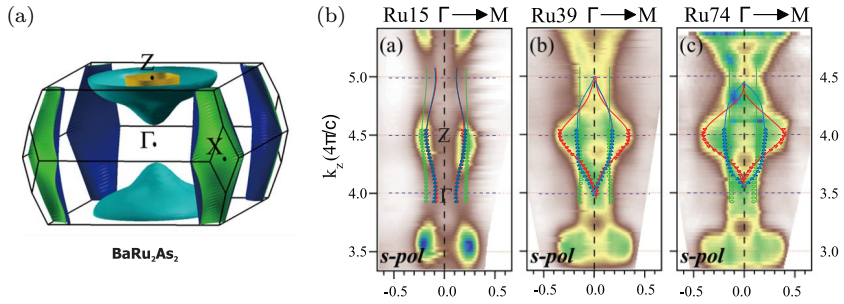

Figure 4.9: (a) Calculated Fermi surface of $BaRu_2As_2$ [200] and (b) evolution of the hole-like Fermi surface sheets with increasing Ru substitution ($x = 0.15$, 0.39 and 0.74) as seen by ARPES experiments [201].

ergy band structure with Ru substitution. Charge doping with Co and K into the Fe-d states can be understood in first order approximation within a rigid band filling picture [121, 122, 199]. That means lifting the chemical potential by introducing additional charge carriers increases the size of the electron pockets while shrinking the hole pockets, hence if obeying Luttinger theorem $n_{\mathrm{el}} > n_{\mathrm{h}}$. Hole doping with K on the Ba site has the opposite effect. In consequence the number of holes and electrons is no longer balanced, the Fermi surface nesting conditions degrade and the SDW instability is continuously suppressed. On the contrary Ru substitution preserves the state of a compensated semimetal, $n_{\mathrm{el}} = n_{\mathrm{h}}$. This has been predicted theoretically [92, 200] and also confirmed by recent ARPES experiments [201, 202], even though the authors report substantial modifications in the Fermi surface itself. The electron-like Fermi surface sheets do not change much in shape but the hole pockets around the Γ-point gain an essential $3D$ character with strong warping in the k_z direction, eventually even disconnecting at the Γ-point and surviving only around Z in a cone shape for large substitution levels x. This is clearly visible in the ARPES maps in the $\Gamma - Z - M$ plane for different Ru content x in Fig. 4.9. Two out of three hole pockets show indeed strong k_z-dispersion while the third keeps the cylinder shape.

There is, however, no consensus reached so far whether Ru substitution leaves the total charge carrier density $n = n_{\mathrm{el}} = n_{\mathrm{h}}$ unchanged. While the reported ARPES experiments do not see significant changes in n with doping up to high doping levels of 70 % [201, 202] or in one case even an increase in the charge carrier density [203], recent theoretical work by Wang *et al.* [92], who try to account for impurity effects of Ru substitution in their calculations, predicts n to be reduced by about 25% in $BaRu_2As_2$ with respect to $BaFe_2As_2$. Sim-

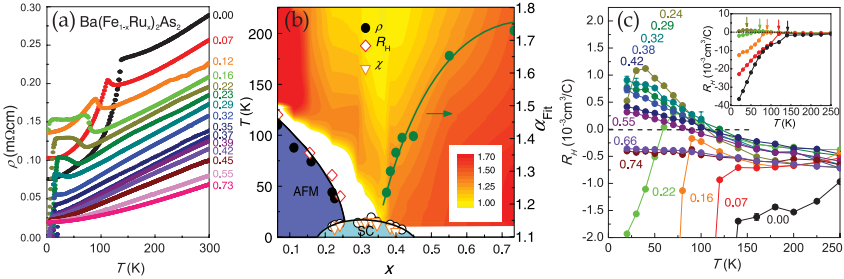

Figure 4.10: Current transport properties of $Ba(Fe_{1-x})_2As_2$. Temperature evolution of (a) the in-plane dc resistivity $\rho(T, x)$, (b) the temperature exponent α according to fits of $\rho(T) = \rho_0 + AT^{\alpha}$, presented in a contour map and (c) Hall resistance R_H. Adapted from Ref. 142.

ilar observations were made by means of quantum oscillation experiments on $BaFe_2(As_{1-x}P_x)_2$ where shrinkage of the electron pockets induces extra holes despite the isovalency of the P substitution [204]. But full substitution in $BaFe_2P_2$ recovers the compensated metal again. The absence of a dominating charge carrier type and hence contributions from both holes and electrons to current transport is directly reflected in the dc and magneto-resistivity characteristics [137, 142]. The Hall resistance R_H exhibits a sign change from negative to positive for a certain doping range x upon cooling [137, 142] as shown in Fig. 4.10(c) – interestingly a unique feature of Ru substitution, not seen for any other compound within the 122 family. It seems obvious to disentangle the electron and hole contributions to the dc transport, σ_{el} and σ_h, by an effective two-band model with different electron and hole mobilities [137], as successfully applied to Co doping before [205]. But Eom *et al.* [142] showed that this model fails to explain the magneto-resistance data. Taking into account AFM fluctuations, which create "hot" and "cold" spots , i.e. increased and reduced scattering rates due to the well nested Fermi surface sheets, in different parts of the electron Fermi-surface sheets depending on their orbital character [206, 207] provides a more coherent picture of the charge transport, when relocating of these spots with Ru substitution is assumed [142]. The temperature dependence of the dc resistivity in Fig. 4.10(a,b) indicates that in the strongly overdoped regime ($x > 0.5$) Fermi liquid behavior (T^2 temperature dependence of the resistivity) is progressively recovered [142]. What actually drives the suppression of the SDW state and eventually enables superconductivity in Ru substituted compounds is still under debate. The extended spatial nature of the Ru 4*d* orbitals, which increases the electronic band width and

reduces the Stoner enhancement (the Stoner parameter[4] for Ru is $I \approx 0.6$, Fe has $I \approx 0.9$) and electronic correlations, is consistently seen as the key player, the microscopic mechanism is not fully resolved yet. Dhaka *et al.* [202] have proposed a magnetic dilution picture consistent with suggested inhomogeneous doping on the nano-scale based on ^{75}As NMR probes [208], that means a suppression of the AFM order in real space. On the other hand, since the latter might also be linked to local distortions of the chemical bonds (to As) [208] and the magnetic dilution is hard to reconcile with the observed modifications in the Fermi surface topology [92, 201, 209] seems to favor the degraded nesting conditions as the main driving force akin to the other types of doping and pressure [131, 134].

[4] I corresponds to U in Eq. 4.1.

4.2 Optical properties of $Ba(Fe_{1-x}Ru_x)_2As_2$

Optical spectroscopy directly probes the low energy charge dynamics and provides immediate access to electronic correlations (e.g. Refs. 210, 211). In general these correlations can influence the optical response up to high energies due to interactions which are usually not taken into account by *ab-intio* electronic band structure calculations. As discussed in chapter 2.1.3 the strength of the correlations can be appraised by the ratio of the experimental and within LDA calculated kinetic energies $K_{\mathrm{exp}}/K_{\mathrm{LDA}}$. Care must be taken to exclude all contributions from interband transitions to K_{exp}. In strongly correlated bad metals as the multi-band iron pnictides this becomes more difficult since low energy interband transitions within the set of Fe-3*d* bands overlap in energy with the intraband transitions. By having the capability to measure both real and imaginary part of the dielectric response independently spectroscopic ellipsometry helps to overcome this issue [212, 213]. Applying the Kramers-Kronig consistency analysis as described in section 2.1.3 we can estimate the spectral weight of the itinerant charge carrier outside the experimentally accessible spectral range. This allows us to track the spectral weight redistribution as a function of the Ru content.

To this end we perform a detailed study of the normal state optical properties of $Ba(Fe_{1-x}Ru_x)_2As_2$ over a wide substitution range starting from the undoped parent compound, crossing the superconducting dome, deep into the overdoped region (up to $x \leq 0.74$). We observe a monotonic spectral weight redistribution in the mid-infrared spectral range (0.3 eV to 1 eV) which establishes a direct link to the Ru substitution. In contrast to remarkable resilience of the itinerant charge carriers in the underdoped region, we find a strong increase in the bare plasma frequency ω_{pl} with increasing Ru substitution and a concurrent strong decrease in the Fe-As bond polarizability (static electric permittivity ϵ_s) which nevertheless still takes remarkable high values (≈ 36 for $x = 0.74$) compared to other high-T_c superconductors ($\epsilon_\infty \approx 5$ [212]). By comparing our results with DFT-LDA electronic band structure calculations and recent ARPES results [201, 202] we attribute this to a strong decrease of electronic correlations or equivalently a reduced band mass m_{b}. In the end we analyze the reduction of the SDW optical gap Δ_{SDW} at moderate Ru doping levels as another measure of the correlation strength.

4.2.1 Sample preparations

The measurements were carried out on single crystals of $Ba(Fe_{1-x}Ru_x)As_2$ grown from FeAs and RuAs self flux in the group of J. S. Kim, Pohang University, as described in Ref. 142. The platelet-like crystals have lateral dimensions ranging from $0.7 \times 1.5\,\mathrm{mm}^2$ to $1.2 \times 2.4\,\mathrm{mm}^2$ and cleave naturally along the

Table 4.1: Doping level x and respective transition temperatures $T_N(x)$ and $T_c(x)$ of the $Ba(Fe_{1-x}R_x)_2As_2$ samples studied in this work.

x	T_N (K)	T_c (K)
0	139	
0.08	119	
0.16	90	
0.23	60	11
0.39		12
0.46		
0.56		
0.74		

FeAs-planes. The actual Ru content of each sample was determined by energy dispersive x-ray (EDX) spectroscopy [142] on several spots on the sample surface. The respective SDW and SC transition temperatures T_N and T_c were inferred from SQUID measurements of the magnetic susceptibility on the same samples and the respective transition temperatures T_N and T_c listed in table 4.1.

4.2.2 Results and Discussion

Mid-infrared interband transitions and itinerant charge carrier response

The real parts of the optical conductivity $\sigma_1(\omega)$ and permittivity $\varepsilon_1(\omega)$ for various Ru substitution levels in the range of $0 \leq x \leq 0.74$ is shown in Fig. 4.11. At low frequencies the optical response is dominated by the contribution of the itinerant charge carriers as indicated by the sharp downturn and negative values of $\varepsilon_1(\omega)$. With rising substitution level x we detect a strong monotonous shift of the screened plasma frequency ω_{pl}^{scr}, i.e. where $\varepsilon_1(\omega) = 0$, from about 160 meV ($x = 0$) to 520 meV ($x = 0.74$). At the same time spectral weight in the optical conductivity is monotonically removed from the spectral range around 0.5 eV and redistributed to higher as well as lower energies. The interband transitions above 2 eV get more pronounced with increasing x. Although we observe significant changes in the strength of theses high frequency interband transitions, surprisingly their center frequencies do not shift. The strong high energy interband transition around 6 eV is quickly suppressed upon Ru substitution and as indicated by the change in the slope of ε_1 shifted to even higher energies.

In aim of a quantitative analysis of the spectral weight redistribution as a

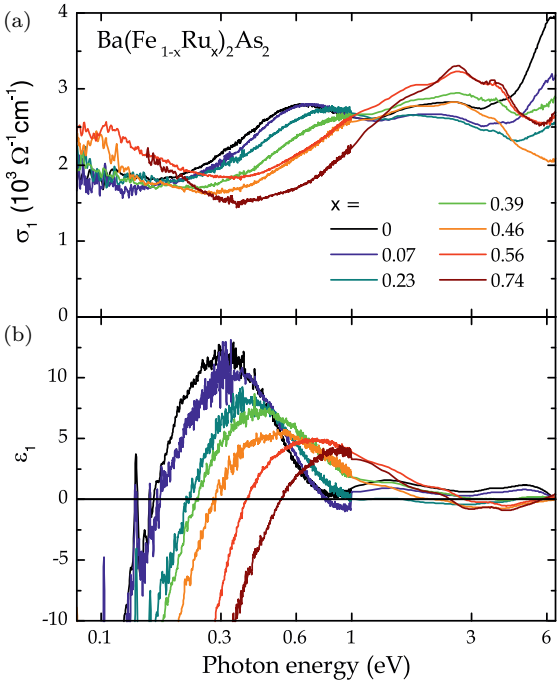

Figure 4.11: Real part of the normal state ($T = 300\,\mathrm{K}$) (a) optical conductivity σ_1 and (b) permittivity ϵ_1 of $Ba(Fe_{1-x}Ru_x)_2As_2$ for various substitution levels x.

function of Ru content x and to address the contributions from itinerant and localized charge carriers separately we perform a dispersion analysis in the framework of the Drude-Lorentz approach, as discussed in section 2.1.2. The interband transitions are parameterized by a minimal set of seven Lorentzian oscillators

$$\varepsilon_{\mathrm{interband}(\omega)} = \sum_{j=1}^{7} \frac{\Delta\varepsilon_j \omega_j^2}{\omega_j^2 - \omega^2 - \mathrm{i}\gamma_j\omega} \ , \tag{4.4}$$

where $\Delta\epsilon_j$ is the contribution to the static permittivity, ω_{0j} the center frequency and γ_j the respective line width:

We are able to address the major spectral features throughout the entire set of samples with the same number of Lorentz oscillators, which gives us the opportunity to track the evolution of the different fitting parameters with

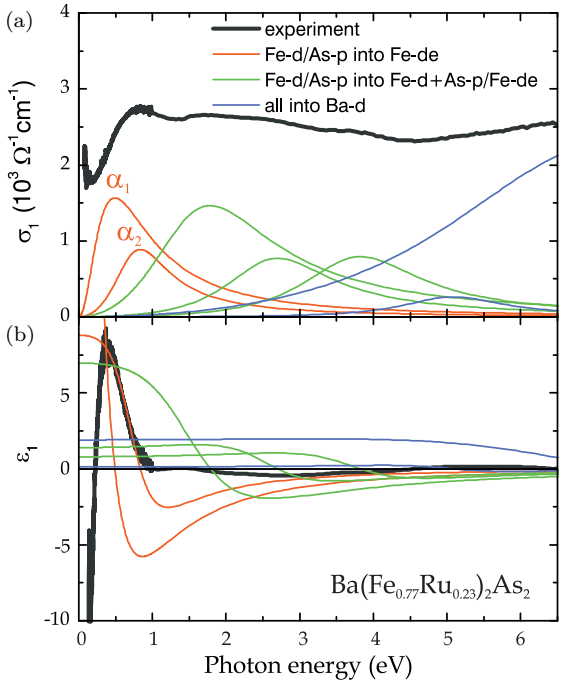

Figure 4.12: Dispersion analysis of the real part of the (a) normal state optical conductivity σ_1 and (b) permittivity ϵ_1 for $x = 0.23$. Data points are shown in gray. Three sets of interband transitions are identified (red, green and blue solid lines) and assigned according to LDA band structure calculations as given in the legend.

increasing x. From the fit we identify three different sets of optical interband transitions, which are illustrated in Fig. 4.12 in the case of substitution level $x = 0.23$. Following *ab-initio* LDA band structure calculations for the parent compound (see Fig. 4.5) the lowest bands (red curves) are assigned to origin from interband transitions within the set of Fe-d bands around the Fermi level. The set of three almost equally strong bands (green curves) in the range between roughly 1.5 and 4.5 eV represent transitions from hybridized Fe-d/As-p states into Fe-d and Fe-d/As-p states. Transitions into Ba-d states well above the Fermi level contribute to the last Lorentzian seen in the spectra (blue curve) which models the vast majority of the UV absorption. The best fit parameters for $x = 0.23$ are listed in Table 4.2.

Table 4.2: Best fit parameters of the Lorentzian terms according eq. 4.4 in the case of $Ba(Fe_{0.77}Ru_{0.23})As_2$. The terms are shown in Fig. 4.12 as red, green and blue solid lines.

j	$\Delta\epsilon_j$	ω_j (eV)	γ_j (eV)
1	50.08	0.491	1.036
2	8.80	0.835	0.931
3	6.96	1.788	2.045
4	1.40	2.703	1.783
5	0.80	3.826	1.977
6	0.13	5.080	1.712
7	1.90	7.348	5.971

We go on and analyze the parameter evolution with Ru content in more detail. First, we will focus on the mid-infrared spectral range (0.4 eV to 1 eV) since these interband transitions are affected most sincerely by Ru substitution. For all doping levels x we have consistently modeled this spectral range by two Lorentzian oscillators denoted as α_1 and α_2 in Fig. 4.13(d) [and red lines in Fig. 4.12]. We observe a monotonous, almost linear transfer of spectral weight (SW) from the lower band α_1 centered around 0.45 eV (blue circles) into the band α_2 (red triangles) around 1 eV [see Fig. 4.13(a)], whereas the total SW is well conserved within these two bands (black squares). This linear dependence suggests a direct link to the mixing ratio of Fe and Ru. With increasing substitution level x the band α_2 shifts up in energy from about 0.8 eV to 1.1 eV [Fig. 4.13(c)], while α_1 keeps centered around 0.4 eV but experiences a drastic loss in its oscillator strength. This results in a strongly reduced contribution to the static permittivity $\Delta\varepsilon_1 = SW_1/\omega_1^2$ [Fig. 4.13(b)]. Within our analysis scheme the lowest band α_1 accounts for almost the entire interband contribution to the static permittivity $\sum_{\text{interband}} \Delta\epsilon_j$. As reported before [213] the interband contributions to the static permittivity take anomalously large values in basically all members of the 122 family ($\epsilon_{\text{inter}} \approx 40$ to 70), which are significantly larger than in the cuprate superconductors where $\epsilon_{\text{inter}} \approx 5$ [212]. This drop in the total $\Delta\epsilon$ of these two bands is slow for small x and gets stronger when x excesses 0.3, where the SDW phase diminishes while superconductivity becomes strongest. We can compare this to P substitution in $BaFe_2(As_{1-x}P_x)_2$ where Nakajima *et al.* [214] also report a small shift of the lowest interband transition to higher energies, but do not analyze it any further. Moreover, they observe that the entire spectral weight redistribution induced by P doping is confined below ~ 0.75 eV. The latter is certainly not the case for Ru substitution where the entire spectral range up to the UV range

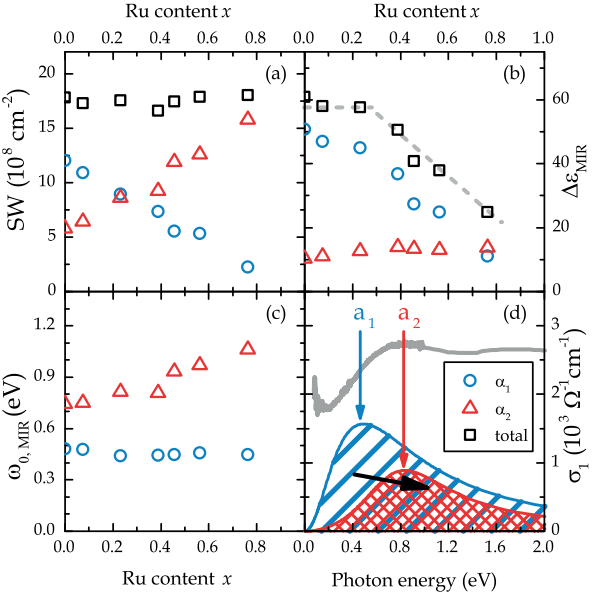

Figure 4.13: Dispersion analysis of the two MIR bands α_1 (blue circles) and α_2 (red triangles). (a) Shift of spectral weight from α_1 to α_2, (b) reduction of polarizability in α_1 and (c) shift of resonance frequency $\omega_{0,\alpha,1}$ in α_2. (d) Contributions of α_1 and α_2 to the optical conductivity σ_1 in the MIR spectral range for Ru content $x = 0.23$.

is susceptible to spectral weight redistribution. Ru substitution apparently modifies the electronic band structure more severely.

Not only the interband transitions strongly evolve with doping but also the low energy response from the itinerant charge carriers (as also evident from dc transport [142]). The itinerant charge carrier response is characterized by the unscreened (bare) plasma frequency ω_{pl} which we infer from the measured spectra following the Kramers-Kronig consistency analysis as described in Sec. 2.1.3. The result of this analysis for the same spectrum ($x = 0.23$) as in Fig. 4.12 is exemplarily depicted in Fig. 4.14. With the interband transitions (blue lines) subtracted from the experimental data (gray lines) we extrapolate the remainder of the optical conductivity with a Drude-like term (red dotted line) so that the Kramers-Kronig transformation of the optical conductivity (Eq. 2.4a) matches the measured real part of the permittivity (red open circles on top of the data in panel (b)). The unscreened plasma frequency ω_{pl} of the itinerant charge carriers is then given by the spectral weight SW_{it} [gray area in panel

(a)] via the f-sum rule (Eq. 2.25). The plasma frequency as a function of doping level x as obtained from this analysis is displayed in the inset of Fig. 4.14. In the underdoped regime ($x \leq 0.35$) the plasma frequency $\omega_{\mathrm{pl}}(x)$ is almost independent of x with values around 1.7 eV, whereas in the overdoped regime it shows a steep, almost linear rise up to about 2.3 eV at $x = 0.74$. These values for the bare plasma frequency ω_{pl} are consistent with the screened plasma frequencies $\omega_{\mathrm{pl}}^{\mathrm{scr}}$ following Eq. 2.9. For $x = 0.23$ as discussed above $\omega_{\mathrm{pl}} = 1.72\,\mathrm{eV}$ and the total contribution to the static dielectric function from the interband transitions $\Delta\varepsilon_{\mathrm{tot}} = 70$ results in $\omega_{\mathrm{pl}}^{\mathrm{scr}} \approx 0.21\,\mathrm{eV}$ compared to the value 0.22 eV from the intersection $\varepsilon_1(\omega) = 0$.

The two main regimes in the doping evolution seem to be observed as well by recent DFT calculations [92] and ARPES experiments [201]. Wang *et al.* [92] compute the band structure and Fermi surface topology for different doping levels up to full substitution. Despite minor changes in the topology good nesting conditions are preserved at least up to $x \approx 0.4$. Above this value the hole-like Fermi surface sheets around Γ become more and more three-dimensional with strong warping along the k_z-direction and eventually disconnect around the Γ-point with large pockets around Z remaining. The latter in accordance with Ref. 200. Wang *et al.* [92] find that the bands around the Fermi level essentially preserve a predominant Fe-d character to even higher doping levels whereas the Ru-d orbitals are mainly located around 0.5 eV below the chemical potential and only take over at the Fermi level close to full substitution. Since the plasma frequency is determined by exactly these bands this picture might explain why the plasma frequency develops only slowly in the underdoped region but more quickly on the overdoped site. This leads to the remarkable resilience of the itinerant charge carriers (and accordingly superconductivity) to rather high impurity levels which are comparable to K and P doping, where optimal doping is also realized around 35 % to 40 %, in contrast to Co ($\sim 7.5\,\%$) or even Ni ($< 5\,\%$) which are also doped into the Fe planes [117].

In analogy from an experimental point of view ARPES experiments can provide further insight on the increase in the plasma frequency. Xu *et al.* [201] find the same regimes in the evolution of the Fermi velocity v_{F} in the Γ-Z plane for both electron and hole pockets: v_{F} is fairly constant below $x \approx 0.4$ and rises quickly on the overdoped site. At the same time they do not observe any significant changes in the total free charge carrier density for both hole and electron-type Fermi surface sheets over the entire doping range, i.e. the compensated semimetallic nature is preserved. Interestingly, there seems to be a charge carrier transfer The Fermi velocity v_{F} is related to the plasma frequency by $\omega_{\mathrm{pl}}^2 \propto N(E_{\mathrm{F}})\langle v_{\mathrm{F}}^2\rangle_{\mathrm{FS}}$ (see e.g. Refs. 215, 216), where $N(E_{\mathrm{F}})$ denotes the electronic density of states at the Fermi level and the brackets $\langle\cdots\rangle$ the average taken over the Fermi surface. In multi-band materials like the iron pnictides the total plasma frequency ω_{pl} as observed in optical spectroscopy

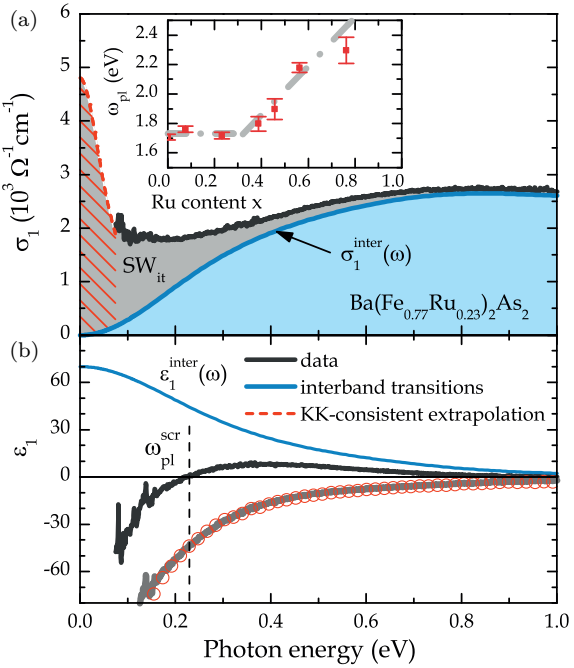

Figure 4.14: Exemplary Kramers-Kronig consistency analysis for ($x = 0.23$). (a) Subtraction of the interband contributions σ_1^{inter} (blue line) from the optical conductivity KK-consistently extrapolated below 70 meV gives the spectral weight SW_{it} (gray shaded area) of the itinerant charge carrier response and hence their unscreened plasma frequency ω_{pl}. (b) Circles (red) show the result of KK-transformation of σ_1 in (a). The dashed vertical line notes the screened plasma frequency ω_{pl}^{scr}. Inset: Bare plasma frequency ω_{pl} of the free charge carrier response as a function of the Ru substitution level x as obtained from the described procedure. The gray dotted line is a guide to the eye.

sums up the contributions from all Fermi surface sheets, each with it's own effective mass and carrier density, and an disentanglement of different bands is typically not possible. Nevertheless, if we take the ARPES result of doping independent total free charge carrier density from Ref. 201 and assume the Fermi velocity in the $k_z = \pi$ plane to be representative for the respective Fermi surface sheets at a specific Ru doping level we can attribute the increase in the plasma frequency in the overdoped regime to the increase in the Fermi velocity, which is then equivalent to a strong decrease in the optical mass [216]. The same argument holds for $\omega_{pl} \propto n/m_b$ directly. Again, these results are

similar to recent observations in isoelectronic P doped $BaFe_2As_2$. A strong, almost quadratic increase in the plasma frequency of the coherent Drude part [214] as well as the Fermi velocity on both hole and electron pockets [217] has been reported recently. The monotonous increase of the plasma frequency in the underdoped region might be due to the slight hole doping seen in quantum oscillation experiments [204]. In this respect P and Ru doping seem to have quite similar influence on the correlations.

Insights from LDA calculations

The strength of electronic correlations is commonly addressed by comparing the kinetic energies $K \propto \omega_{\mathrm{pl}}^2$ obtained from electronic band structure calculation with the experimental ones [22, 41].

Ab-initio electronic structure calculations for different Ru substitution levels x were performed by A. N. Yaresko, in the framework of the linear muffin-tin orbital method [108, 109] using the experimentally obtained lattice parameters of $Ba(Fe,Ru)_2As_2$ [137]. Different substitution levels $x = 0, 0.25, 0.5, 0.75$ and 1 were realized by constructing super-cells enlarged by $\sqrt{2} \times \sqrt{2}$ within the Fe/Ru planes with respect to the Fe_4 tetragonal unit-cell. In accordance with the report from Zhang and Singh [200], for partial substitution of $x = 0.25$ and $x = 0.75$ the results are robust with respect to the arrangement of the Ru and Fe atoms within the super-cell. Equal mixing of Fe and Ru ($x = 0.5$), however, appears to be more sensitive. While in the optical conductivity the interband transitions experience only minor changes on small sharp features, the calculated plasma frequency varies more drastically. To account for these variations the spectra presented below are averaged over different atomic configurations inside the unit-cell.

Before we go on, we note that since we can extract the pure ab-plane and c-axis response from the calculations we can check for the influence of the finite uniaxial anisotropy on the ellipsometric data, which in principal can be expected from the weak coupling between the FeAs-layers. However, we find only small deviations of the in-plane pseudo-dielectric function from the pure ab-plane response. The main features in the spectra are not altered and hence the treatment of the ellipsometric data in the simplified framework of an isotropic bulk material is a posteriori justified.

Fig. 4.15 shows both the experimental and calculated optical conductivity $\sigma_1(\omega)$ for three different substitution levels $x = 0.25, 0.5, 0.75$ in the calculation and $x = 0.23, 0.54, 0.76$ in the experiment. In the spectral range above $\sim 4\,\mathrm{eV}$ the $\sigma_1(\omega)$ is well reproduced even in absolute numbers. At lower energies, however, we detect the known deviations between experiment and LDA calculations: the lowest interband transitions in the calculated spectra appear between 1 and 2 eV, which is also indicated by a strong upturn in ϵ_1 around the

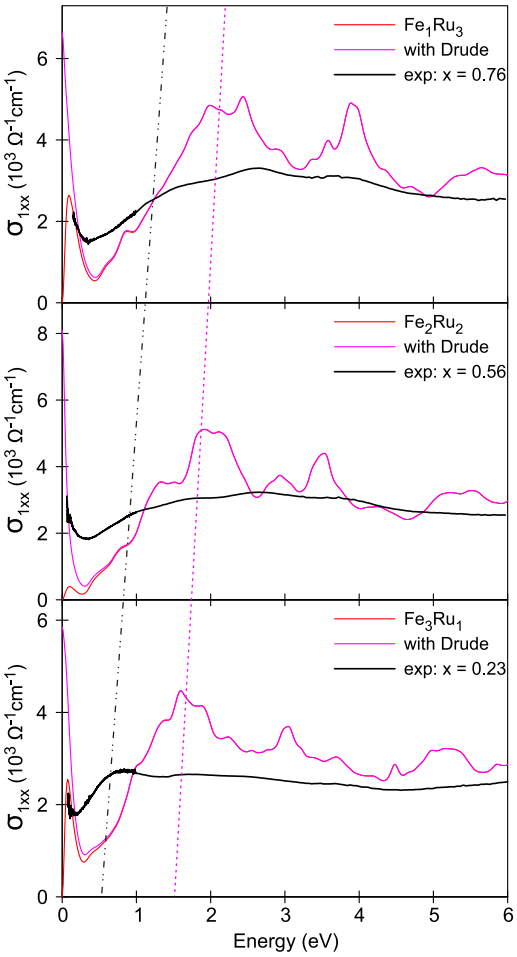

Figure 4.15: Real part of the in-plane optical conductivity $\sigma_1\omega$ of $Ba(Fe_{1-x}Ru_x)_2As_2$ for several substitution levels x as obtained from LDA calculations along with the experimental data. The dashed vertical lines track (as an guide to the eye) the shift in the position of the lowest MIR peak.

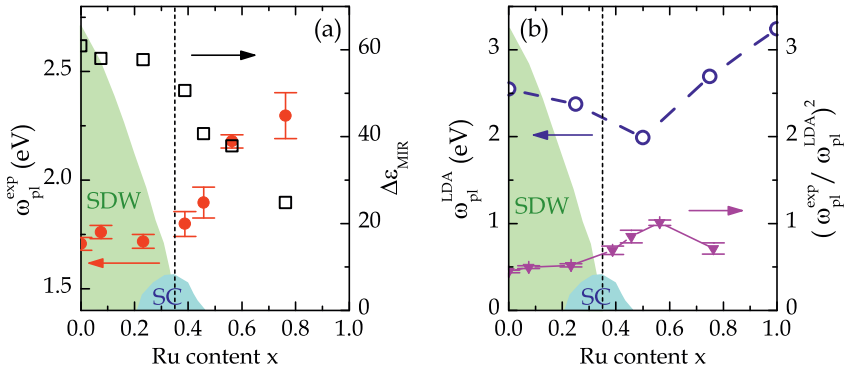

Figure 4.16: (a) Experimental plasma frequency $\omega_{\mathrm{pl}}^{\mathrm{exp}}$ (circles) [from inset in Fig. 4.14] and MIR oscillator strength (squares) (see also Fig. 4.13(b)] as a function of Ru substitution x in $Ba(Fe_{1-x}Ru_x)_2As_2$ on top of a schematic phase diagram. (b) Plasma frequency $\omega_{\mathrm{pl}}^{\mathrm{LDA}}$ (circles) as obtained from LDA calculations and the ratio of the respective kinetic energies $K_{\mathrm{exp}}/K_{\mathrm{LDA}} = (\omega_{\mathrm{pl}}^{\mathrm{exp}}/\omega_{\mathrm{pl}}^{\mathrm{LDA}})^2$ (triangles). Dashed vertical lines denote optimal T_c and and full suppression of the SDW order at $x \approx 0.35$.

same frequencies (not shown), in contrast to the experiments where the lowest interband transitions reside around 0.5 This is generally attributed to the effective mass renormalization needed to reconcile the low energy band structure with ARPES spectra since electronic correlations are naturally not fully captured in a localized approximation. This has been observed throughout the iron pnictide family [171, 218–221]. With increasing Ru content the mid-infrared bands monotonically shift up in frequency (indicated by the vertical dashed lines) which is, disregarding the band width renormalization, qualitatively in good agreement with our experimental observations in this spectral range. The shifting up in frequency is directly related to the drop in the polarizability of the system as expressed in the drop of $\Delta\varepsilon(x)$ above $x \approx 0.4$ plotted in Fig. 4.16(a).

Finally, we can assess the strength of the electronic correlations by comparing the plasma frequency obtained from the spectra $\omega_{\mathrm{pl}}^{\mathrm{exp}}$ with the results from the LDA calculations $\omega_{\mathrm{pl}}^{\mathrm{LDA}}$. The doping evolution of the plasma frequency $\omega_{\mathrm{pl}}^{\mathrm{LDA}}(x)$ from the calculations (open circles) is shown in Fig. 4.16(b). For undoped $BaFe_2As_2$ we find in the calculation $\omega_{\mathrm{pl}}^{\mathrm{LDA}}(0) = 2.55\,\mathrm{eV}$ consistent with reported values [41, 117, 222]. With increasing Ru content x $\omega_{\mathrm{pl,LDA}}(x)$ goes through a minimum of about 2 eV around $x = 0.5$ and rises again strongly in the overdoped regime indicating strong metallicity of the end member of the series, $BaRu_2As_2$. Within the tight binding framework the ratio of kinetic

Table 4.3: Larger optical spin-density–wave gap $2\Delta_L^{SDW}$ and corresponding gap ratio of $Ba(Fe_{1-x}Ru_x)_2As_2$ as a function of x as inferred from the optical conductivity spectra in Fig. 4.17 and from Table 4.4.

x	0	0.07	0.13
$2\Delta_L^{SDW}$ (cm^{-1})	745	445(20)	300(20)
k_BT_N (cm^{-1})	96	83	62
$2\Delta_L^{SDW}/k_BT_N$	7.8	5.3(3)	4.8(3)

energies $K_{exp}/K_{LDA} = (\omega_{pl}^{exp}/\omega_{pl}^{LDA})^2$ shows an interesting development with increasing Ru content x. Starting off at ~ 0.47 for $x = 0$ – somewhat larger as a previous estimate of ~ 0.3 [41] – the ratio rises slowly to unity in the overdoped region. Although there is some uncertainty in the absolute values of K_{exp}/K_{LDA}, especially at $x = 0.74$, the trend is clear. The correlations get reduced with increasing Ru content x, first slowly when only few Ru atoms are there, then more and more pronounced when the contribution of Ru $4d$ states at the Fermi level becomes noticeable.

Spin-density-wave gap in $Ba(Fe_{1-x}Ru_x)_2As_2$

Suppression of the SDW phase is a requirement for establishing the superconducting state. Tracking the evolution of the SDW gap Δ^{SDW} in the optical conductivity with increasing Ru substitution x and gradually decreasing Neél temperature T_N serves as an additional measure of the strength of the SDW instability. We extended the spectral range to the far infrared ($150\,cm^{-1}$ to $600\,cm^{-1}$) with synchrotron based ellipsometry in the temperature range of 10 K to 300 K.

We define the gap ratio as $2\Delta_L^{SDW}/k_BT_N$ with k_B being the Boltzmann constant. Table 4.3 summarizes the values for the larger gap Δ_L^{SDW} obtained from difference spectra $\Delta\sigma_1(T,\omega) = \sigma_1(T,\omega) - \sigma_1(T_0,\omega)$ with $T_0 \geq T_N$ for the samples with substitution levels of $x = 0.07$ and 0.13 (see Fig. 4.17 (a,b)). In all samples the smaller gap Δ_S^{SDW}, clearly visible in the parent compound (see section 4.3), as well as even the large gap at $x = 0.23$ lie below our experimentally accessible spectral range ($\omega < 150\,cm^{-1}$). From the $x = 0.07$ sample we find that already small amounts of Ru suppress the optical gap significantly, while the Neél temperature T_N itself is much less affected. The gap ratio is reduced from 7.8 to 5.3 with respect to the parent compound. Increasing x suppresses both $T_N$and the gap further and their ratio further reduces to 4.8 for $x = 0.16$. This trend reflects the reduction in strength of the SDW instability with increasing Ru substitution. The suppression of Δ_L^{SDW} by Ru

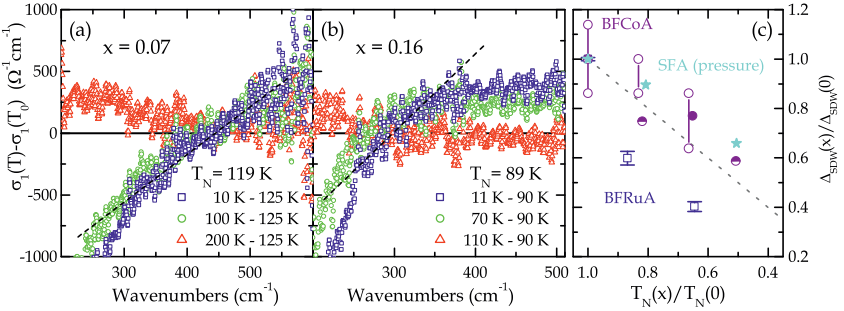

Figure 4.17: Optical SDW-gaps in $Ba(Fe_{1-x}Ru_x)_2As_2$. (a,b) Difference optical conductivity $\sigma_1(T) - \sigma_1(T_0)$ with $T_0 \geq T_N$ for $x = 0.07$ and 0.13 at different temperatures T. The dashed lines mark a linear fit to the lowest $T = 10\,\mathrm{K}$ difference spectrum. (c) Normalized larger SDW-gap $\Delta_L^{SDW}(x)/\Delta_L^{SDW}(0)$ (blue squares) as a function of normalized Néel temperature $T_N(x)/T_N(0)$ extracted from spectra in (a) and (b) as well as gap values for $SrFe_2As_2$ under pressure [176] (light blue triangles) and $Ba(Fe1-xCox)_2As_2$ from twinned [175, 226] (full circles) and detwinned samples [225] (vertically connected open circles) normalized to their respective parent compounds. The dashed line marks the case of a constant gap ratio.

substitution is somewhat stronger as compared to the evolution upon external pressure reported for $SrFe_2As_2$ [176] as well as Co doping in $BaFe_2As_2$ [175] [dot and triangles in Fig. 4.17(c)]. This is in contrast to the observation that hydrostatic pressure and Ru doping have a very similar effect on suppression of T_N and the phase diagrams for different types of doping and under pressure actually fall nicely on top of each other when universally scaled with a universal relation 0.1 of Ru doping equals G3 Pa [197] [see Fig. 4.8]. Nevertheless, the observed trend is still comparable, especially taking into account that the absolute gap value, as defined here via the quasi-isosbestic point below which the SW is suppressed, depends to some extend on the sample quality. In the undoped parent compound $BaFe_2As_2$for example gap values in the rage of $650\,\mathrm{cm}^{-1}$ to $750\,\mathrm{cm}^{-1}$ have been reported [173, 175, 222, 223]). Moreover, the gap differs significantly in detwinned samples along the a- ($600\,\mathrm{cm}^{-1}$) and b-axis ($850\,\mathrm{cm}^{-1}$) of the orthorhombic phase [224, 225], giving rise to some additional uncertainty when the optical conductivity is averaged in twinned single crystals.

4.2.3 Conclusions

We have determined for the first time the normal state complex dielectric function $\varepsilon(\omega)$ of $Ba(Fe_{1-x}Ru_x)_2As_2$ in a broad spectral range for different substitution levels x. From that we were able to extract the doping evolution of two

main characteristic optical parameters: the unscreened plasma frequency $\omega_p(x)$ and the contribution to the static dielectric permittivity $\Delta\varepsilon_{MIR}(x)$ from the lowest MIR bands. Both quantities shows a clear correlation with the doping evolution of the spin-density-wave phase and the superconducting dome in the phase diagram. While rather constant in the underdoped region around optimal doping and full suppression of the SDW instability ($x \approx 0.35$) both $\omega_{pl}(x)$ and $\Delta\varepsilon_{MIR}(x)$ change their behavior drastically: $\omega_{pl}(x)$ rises and $\Delta\varepsilon_{MIR}(x)$ drops significantly. Scaling the experimental plasma frequency with its LDA counterpart allows for gauging the electronic correlations. As expected from the spatially more extended 4*d* orbitals in Ru compared to 3*d*-Fe the electronic correlations get more and more reduced as the Ru content increases. Our results are consistent with recent ARPES measurements [201]. Since Ru indeed leaves the total charge carrier density unchanged we can link the increase in $\omega_{pl}(x)$ in the overdoped region to an increase in the average Fermi velocity $v_F(x)$, which by itself reflects the modifications in the band dispersion at the Fermi level. The suppression of the bond polarizability, which is proportional to $\Delta\varepsilon_{MIR}(x)$, beyond optimal doping can contribute significantly to the suppression of superconductivity After all, in terms of the optical properties Ru doping on the Fe site seems to be quite similar to P doping on the As site, which brings these two approaches to induce superconductivity in the 122 compounds closer together. The bonds are further strengthened by the recent observation of horizontal line-nodes in the superconducting gap in the Ru doped compounds similar to $BaFe_2(As_P)_2$ [189].

4.3 SDW-induced anomalies in the optical conductivity of $A\mathrm{Fe_2As_2}$ with A = Ca, Sr, Ba

Although the growth of $CaFe_2As_2$ (Ref. 127) and its phase diagram with respect to cobalt doping [227] were first reported several years ago, the interest in this material started to build up upon the observation of its surprising sensitivity not only to doping and pressure but also to annealing [228]. The direct observation of electronic nematicity due to anisotropic impurity scattering potential of substituted cobalt atoms in the underdoped region of the phase diagram of $Ca(Fe_{1-x}Co_x)_2As_2$ (Ref. 229, 230), analogous to $Ba(Fe_{1-x}Co_x)_2As_2$ (Refs. 225, 231–233), has brought $CaFe_2As_2$ to the forefront of condensed-matter research. Notwithstanding all this interest and some preliminary measurements [234] (normal-state optical-conductivity data from Ref. 234 were also reproduced in Ref. 174), as well as extensive studies of the charge dynamics in both the parent $(Ba, Sr, Eu)Fe_2As_2$ (Refs. 173, 174, 235–238) and most of their doped/substituted superconducting derivatives, [174, 175, 214, 222, 239–247] the detailed investigation of the charge dynamics in $CaFe_2As_2$ and a systematic comparison with other 122-type materials are still lacking.

In the present work we fill this gap by reporting broad band ellipsometric study of not only $CaFe_2As_2$ but also its Sr- and Ba-based counterparts and a systematic comparison thereof over a wide spectral range, complemented by a thorough Drude-Lorentz analysis of the interband and itinerant optical response. We find that, similarly to the previous reports on $BaFe_2As_2$ and $SrFe_2As_2$ (Ref. 173, 222), two distinct SDW energy gaps can be identified in the Ca-based compound. In order to address the degree of interplay between these two SDW subsystems we further carried out a detailed temperature-dependent study of the far-infrared conductivity of all these compounds and discovered the presence of an anomaly at $T^* \approx 80$ K in $CaFe_2As_2$ well below its Néel temperature at the frequencies of the smaller SDW energy gap. This observation clearly indicates that the two electronic subsystems in this material are weakly coupled (as shown for the analogous case of superconductivity in Refs. 248–252). Further comparison with the Sr- and Ba-based counterparts reveals that this coupling evolves via intermediate in the former to strong in the latter compound, systematically with increasing atomic number of the intercalant. The temperature dependence of the infrared phonons shows a clear anomaly at T_N in all three compounds, whereby the SDW-induced modifications of the phonon properties set in exactly at T_N in both Ba- and Sr-based materials but at somewhat higher temperatures in $CaFe_2As_2$, suggesting the early development of SDW fluctuations and their impact on the lattice. We also find a possible indication of T^* in the temperature dependence of the Ca-related phonon intensity $\Delta\varepsilon_0$.

The results and their discussion as presented in this chapter has been published in A. Charnukha, D. Pröpper *et al.*, Phys. Rev. B **88**, 184511 (2013).

4.3.1 Sample preparations

The parent (Ca,Sr)Fe$_2$As$_2$ single crystals were grown in zirconia crucibles sealed in quartz ampoules under argon atmosphere [253]. From dc resistivity and magnetization measurements we obtained the Néel temperatures T_N = 150 and 200 K for CaFe$_2$As$_2$ (see Fig. 4.18) and SrFe$_2$As$_2$ (Ref. 253), respectively. This characterization of our CaFe$_2$As$_2$ samples revealed no secondary transitions at lower temperatures related to the collapsed tetragonal phase, previously observed in this material for certain growth conditions [254]. BaFe$_2$As$_2$ single crystals were grown from As-rich self-flux in a glassy carbon crucible using pre-reacted FeAs$_2$ powders mixed with Ba and As [255]. The sample surface was cleaved prior to every optical measurement. All samples were grown either by T. Wolf, KIT Karlsruhe, or in the group of C. T. Lin, MPI-FKF.

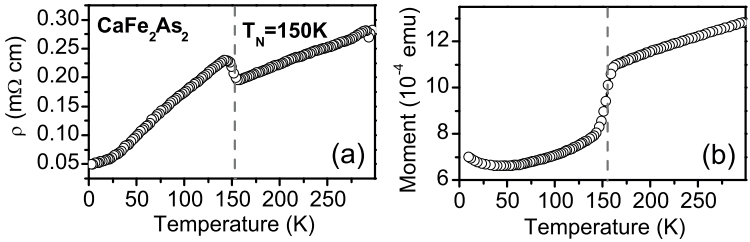

Figure 4.18: Temperature dependence of the resistivity (a) and magnetic moment (b) of the CaFe$_2$As$_2$ single crystals used in the present study. Both measurements reveal a clear signature of a SDW transition at about 150 K and the absence of any secondary transitions at lower temperatures related to the collapsed tetragonal phase, previously observed in this material for certain growth conditions [254].

4.3.2 Results and Discussion

Optical conductivity

The independently obtained real and imaginary parts of the complex optical conductivity $\sigma(\omega) = \sigma_1(\omega)+i\sigma_2(\omega)$ of the AFe$_2$As$_2$, (A=Ca, Sr, Ba) compounds in the entire investigated spectral range at several representative temperatures is shown in Fig. 4.19. The far-infrared response of CaFe$_2$As$_2$ [Fig. 4.19(a) and 4.19(d)] in the normal state is dominated by a strong itinerant response, clearly manifested in the large positive values of both $\sigma_1(\omega)$ and $\sigma_2(\omega)$. Below the SDW

transition temperature of 150 K this itinerant response experiences a dramatic suppression due to the opening of an energy gap in the quasiparticle excitation spectrum, as previously observed in this and other 122-type iron-based materials [173–176]. Due to the conservation of the total number of electrons, the missing area under the conductivity curve at low frequencies is transferred to higher energies, which results in a formation of a "hump" structure [38, 256]. In the most common case when the SDW energy gap does not cover the entire Fermi surface of a material and, therefore, the optical conductivity remains non-zero at all frequencies, determination of the optical quasiparticle excitation gap 2Δ from the conductivity spectra is difficult but it can be approximated by the energy, at which the low-temperature conductivity spectrum crosses the one at the Néel temperature for the first time [256]. This energy $2\Delta_{\mathrm{L}}^{\mathrm{SDW}}$ is marked by the right vertical dashed lines in panel 4.19(a). At lowest frequencies, the optical conductivity of $CaFe_2As_2$ reveals a change in its shape at 10 K as compared to intermediate temperatures below T_{N}, which indicates the presence of another SDW gap, with a smaller magnitude $2\Delta_{\mathrm{S}}^{\mathrm{SDW}}$ [left vertical dashed line in panel 4.19(a)]. This observation is analogous to the previous report of two different SDW energy gaps in the Sr- and Ba-based compound of the same class [173, 222, 235]. Our own ellipsometric measurements on the Sr- and Ba-based compounds, shown in Fig. 4.19(b,e) and 4.19(c,f) fully reproduce and confirm previously reported data, [173–176, 222, 235, 237] provide additional information due to the independently obtained real and imaginary parts of the optical conductivity, and allow for a systematic investigation of the electronic properties of the $ThCr_2Si_2$-type iron-based materials as a function of the intercalating atom.

First of all, we find that, although the Néel temperature does not show a systematic dependence on the atomic number of the intercalating atom, the gap ratios, which quantify the strength of the coupling to a boson mediating a given electronic instability, certainly do display some systematic trends, as shown in Table 4.4. Here we define the gap ratio of an itinerant antiferromagnetic material with an optical SDW energy gap 2Δ and a Néel temperature T_{N} as $2\Delta/k_{\mathrm{B}}T_{\mathrm{N}}$, where k_{B} is the Boltzmann constant. The values of the large and small optical SDW gaps are extracted from the experimentally obtained optical conductivity as described above and indicated in Fig. 4.19 with vertical dashed lines.

Table 4.4 shows that, albeit the Ca-based compound has a Néel temperature significantly lower than that of the Sr-based counterpart and comparable to that of $BaFe_2As_2$, its both gap ratios are significantly larger than those of the other two materials, which implies a much stronger electronic instability in this compound. In addition, the larger gap ratio $2\Delta_{\mathrm{L}}^{\mathrm{SDW}}/k_{\mathrm{B}}T_{\mathrm{N}}$ gradually decreases with the increasing atomic number of the intercalant.

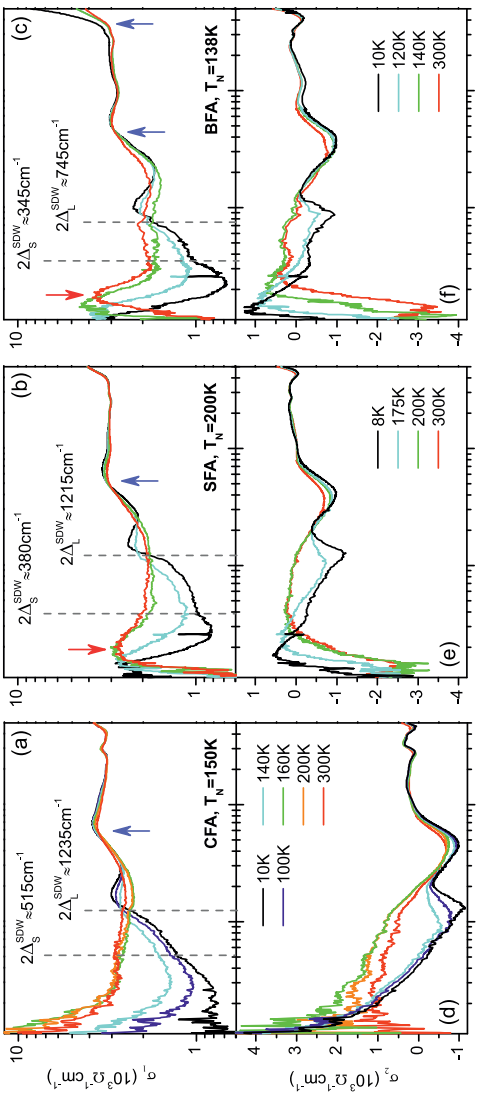

Figure 4.19: (a)–(c) Real part of the complex optical conductivity of $CaFe_2As_2$ (a), $SrFe_2As_2$ (b), and $BaFe_2As_2$ (c). Characteristic energies of the large and small optical SDW gaps ($2\Delta_{L,S}^{SDW}$, vertical dashed lines) are defined as the intersection points between the lowest and the Néel temperatures for the large gap and the deviation point for the small gap (see text). Strongly temperature dependent absorption bands are marked with blue arrows. Low-energy peak feature observed in Sr- and Ba-based compounds but not in $CaFe_2As_2$ is indicated with red arrows. (d)–(f) The corresponding imaginary part of the complex optical conductivity.

Table 4.4: Large and small optical SDW gap $2\Delta_{L,S}^{SDW}$ as inferred from the optical conductivity spectra in Fig. 4.19 and the corresponding gap ratios.

	$CaFe_2As_2$	$SrFe_2As_2$	$BaFe_2As_2$
$2\Delta_L^{SDW}$, cm^{-1}	1235	1215	745
$2\Delta_S^{SDW}$, cm^{-1}	515	380	345
k_BT_N, cm^{-1}	105	140	96
$2\Delta_L^{SDW}/k_BT_N$	11.8	8.7	7.8
$2\Delta_S^{SDW}/k_BT_N$	4.9	2.7	3.6
$2\Delta_L^{SDW}/2\Delta_S^{SDW}$	2.4	3.2	2.14

The existence of a large anisotropy in the optical conductivity of detwinned $BaFe_2As_2$ identified in a previous study [225] suggests that the two gap-like features might originate from the electronic transport along the two different in-plane crystallographic axes in the orthorhombic antiferromagnetic state. However, while the overall level of the optical conductivity, the intensity of the Fe-As–related phonon at about $250 - 260$ cm^{-1}, and the spectral-weight redistribution from low to high energies show a remarkable anisotropy in detwinned crystals, both gap-like features are present and have essentially identical energy scales in both directions [225]. At the same time, the anomaly at T^* in the temperature dependence of the optical conductivity of $CaFe_2As_2$ is only observed at the energies of the smaller gap-like feature and is entirely absent at higher energies, as shown in Fig. 4.20a. Therefore, the origin of these two features is unlikely to lie exclusively in the anisotropy of the 122 compounds.

The far-infrared optical conductivity of $SrFe_2As_2$ and $BaFe_2As_2$ at lowest frequencies is dominated by a peak feature [red arrows in Fig. 4.19(b,c)] reminiscent of the collective excitation previously observed in the nearly optimally doped high-temperature cuprate superconductor $YBa_2Cu_3O_{6+x}$ pristine [257] and after irradiation with helium ions [258]. One of the possible origins of this feature is charge-carrier localization, as observed in disordered doped superconductors [259–261]. It also can not be excluded that this low-energy feature arises due to the contaminating contribution of the intense phonon mode in the out-of-plane optical conductivity [262] to the in-plane response extracted at a grazing angle of incidence. Whatever the origin of this low-energy peak feature may be, it does not affect any of the analysis below. As discussed in section 2.1.3 within the KK analysis the exact shape of the far infrared spectral range is of minor importance since the procedure relies on the real part of the

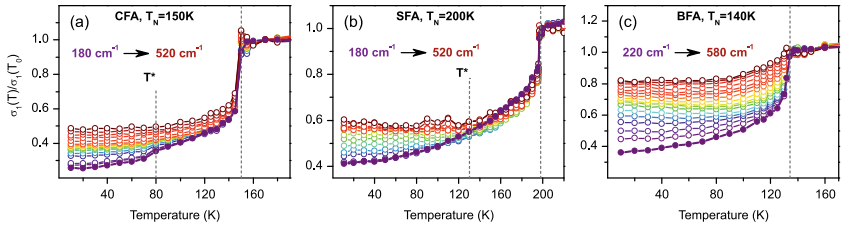

Figure 4.20: (a)–(c) Detailed temperature dependence of the real part of the complex optical conductivity of $CaFe_2As_2$ (a), $SrFe_2As_2$ (b), and $BaFe_2As_2$ (c) on a fine grid of wavenumbers in the far-infrared spectral range, normalized to the value of the optical conductivity at $T = T_0$ close to T_N (T_0 = 170 K, 200 K and 140 K for the Ca-, Sr-, and Ba-based compounds, respectively). The grid of wavenumbers runs from 180 cm^{-1} (blue colors) to 520 cm^{-1} (red colors) in steps of 20 cm^{-1} with the exception of the spectral window of the 260 cm^{-1} phonon. SDW-related features in the temperature dependence of the optical conductivity (vertical dashed lines), for interpretation see text. The lowest-frequency temperature dependence is plotted as filled circles unlike the rest (open circles) to emphasize the change in the temperature dependence of the optical conductivity.

dielectric function $\varepsilon_1(\omega)$ between 2000 cm^{-1} and 3000 cm^{-1}. In this range the shape uncertainty is negligible.

At higher energies the optical conductivity of all three compounds shows a strongly temperature-dependent absorption band centered at about 5000–6000 cm^{-1}, as well as at UV energies in the case of $BaFe_2As_2$, as shown in Figs. 4.19(a)-4.19(c) with blue arrows.

Temperature dependence of the SDW-induced suppression

The existence of two separate SDW energy gaps raises a question as to the degree of interaction between the corresponding electronic subsystems. This question becomes particularly difficult to address in the presence of as many Fermi-surface sheets as is the case for the iron-based materials, which often commonly possess five separate Fermi-surface sheets in the first Brillouin zone. This complexity arises mainly due to the fact that the optical conductivity represents an intertwined response of all electronic subsystems at once. To shed some light onto this issue, in addition to our broad band ellipsometric measurements at several representative temperatures, we have carried out detailed measurements in the far-infrared spectral range (i.e. in the range where the real part of the optical conductivity experiences a drastic suppression, as shown in Fig. 4.19) with a very fine temperature grid for all three materials in question. The results are compiled in Fig. 4.20, which shows the temperature dependence of the optical conductivity normalized to its value at $T = T_0$

close to T_N (T_0 = 170 K, 200 K, and 140 K for the Ca-, Sr-, and Ba-based compounds, respectively) at an equidistant set of wavenumbers from 180 cm^{-1} (blue colors) to 520 cm^{-1} (red colors) in steps of 20 cm^{-1} with the exception of the spectral window of the 260 cm^{-1} phonon.

The temperature dependence of the normalized conductivity shows a very pronounced drop for all compounds at their respective Néel temperatures (right vertical dashed lines) due to the onset of SDW order, with a clear mean-field order-parameter–like temperature dependence at large wavenumbers (red colors). This temperature dependence changes, however, as one moves toward progressively smaller wavenumbers and in the case of $CaFe_2As_2$ reveals a clear second suppression feature at a temperature T^* of about 80 K. This second feature becomes washed out in the Sr-based compound, although the temperature dependence of σ_1 at smallest wavenumbers remains markedly different from that at large wavenumbers and some sort of an analogue of T^* can be sketched also in this case, although there is no clear second suppression feature present in any of the separate temperature dependencies themselves. Finally, in the case of $BaFe_2As_2$, the change in the temperature dependence of σ_1 between large and small wavenumbers becomes hardly noticeable, with the exception of an upturn in its temperature dependence at intermediate frequencies due to the pile-up of the spectral weight transferred from the energies below $2\Delta_S^{SDW}$.

The presence of a second suppression feature in the temperature dependence of the real part of the optical conductivity at small enough wavenumbers in $CaFe_2As_2$ indicates, that the electronic subsystem that develops the smaller SDW energy gap $2\Delta_S^{SDW}$ preserves some knowledge about its own Néel temperature that it *would have* if this subsystem were completely independent from the other(s). In any real material all electronic subsystems are coupled, even if weakly, so that all SDW energy gaps open at the same T_N. However, in case of weak inter-subsystem coupling, those with smaller gaps exhibit an anomaly below the real Néel temperature, as is the case in $CaFe_2As_2$, albeit this anomaly does not correspond to a true phase transition. Such an effect has been predicted theoretically for the analogous case of multi-band superconductivity [248, 249] and discovered experimentally in $FeSe_{1-x}$ in Refs. 250–252. This argument thus suggests that in the Ca-based material the two electronic subsystems developing the large and the small SDW energy gap are weakly coupled. Naturally, as the coupling between such electronic subsystems increases, the temperature dependence of the small gap would gradually approach that of the large gap via an intermediate state when it already does not show any anomaly but still has not matched the temperature dependence of the large gap. Figure 4.20(b) provides evidence for such a behavior in the Sr-based iron pnictide. Finally, the temperature dependence of the normalized optical conductivity in $BaFe_2As_2$ is almost the same at all wavenumbers, both in the region of the large SDW gap and in that of the small one, indicating strongly cou-

pled electronic subsystems in this compound. Thus, by monitoring the detailed temperature dependence of the optical conductivity in the far-infrared spectral range on a fine grid of wavenumbers, a gradual transition could be observed from weak coupling between the electronic subsystems developing the two different SDW energy gaps in $CaFe_2As_2$, via intermediate coupling in $SrFe_2As_2$, to strong coupling between them in $BaFe_2As_2$, systematically with increasing atomic number of the intercalant.

Temperature dependence of the infrared phonons

We now use the same detailed ellipsometric measurements of the real and imaginary parts of the optical conductivity to analyze and compare between the three different compounds the temperature dependence of the strength, position, and the width of the far-infrared optical phonons. As can be seen in Fig. 4.19, the low-energy phonon due to the vibrations of the intercalating ions can be seen at $\approx$ 140 cm^{-1} in the Ca-based compound but not in the Sr- and Ba-based counterparts due to the much smaller mass of the former, which pushes this phonon into the accessible experimental spectral range. The phonon arising from vibrations of Fe and As is seen at an approximately the same position of 260 cm^{-1} in all three materials. The detailed temperature dependence of the Lorentz parameters of the Ca-related phonon at temperatures below T_N, where it can be clearly resolved, as well as the comparison of the Lorentz parameters of the 260 cm^{-1}-phonon in all three compounds is shown in Fig. 4.21.

In the $CaFe_2As_2$ compound, the splitting of the Ca-related phonon at the magneto-structural transition can be clearly resolved, similarly to the previously reported splitting of the Ba-related phonon in the sister compound, [237] and amounts to about 8 cm^{-1} [Fig. 4.21(b)] . Within the noise floor the temperature dependence of the width of these two phonons, plotted in Fig. 4.21(c), does not appear to display any anomalies. That of the phonon strength $\Delta\varepsilon$, on the other hand, seems to slightly change at the temperature T^* [left vertical dashed line in (a)] inferred from Fig. 4.20(a), albeit this change is quite close to the limit of the fit uncertainty.

The temperature dependence of all Lorentz parameters of the Fe-As phonon in all three compounds, Fig. 4.21(d)–(f), shows noticeable anomalies at the respective Néel temperatures (gray, light blue, and pink vertical dashed lines for Ca-, Sr-, and Ba-based compounds, respectively). In $SrFe_2As_2$ and $BaFe_2As_2$ the phonon intensity $\Delta\varepsilon_0$ and position ω_0 change abruptly at the magneto-structural transition temperature, as shown in Fig. 4.21(d), 4.21(e), whereas in $CaFe_2As_2$, quite surprisingly, the SDW-induced changes seem to set in already at somewhat higher temperatures [Fig. 4.21(e)]. This observation indicates the existence of incipient critical lattice strain at temperatures higher than the magneto-structural transition temperature in this compound, which may be

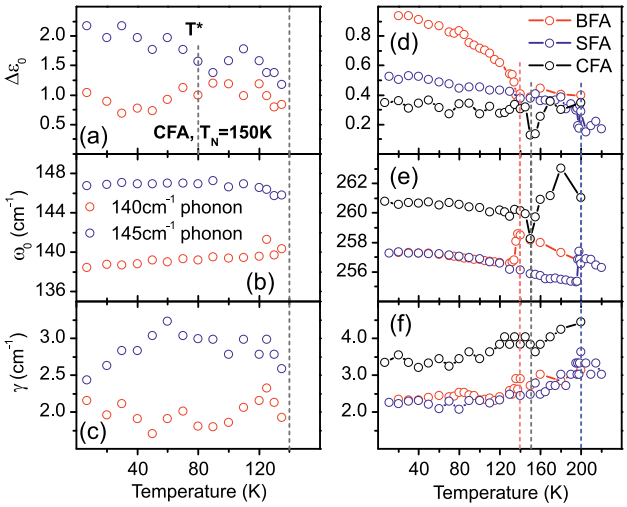

Figure 4.21: (a)–(c) Temperature dependence of the strength $\Delta\varepsilon$, position ω_0, and the width γ of the Ca-related phonon below the Néel transition temperature of $CaFe_2As_2$, split due to the lowering of the crystallographic symmetry from tetragonal to orthorhombic at the concomitant structural transition (right vertical dashed line). The temperature T^* of the small optical SDW gap $2\Delta_S^{SDW}$ [left vertical dashed line in (a)] as inferred from Fig. 4.20(a). (d)–(f) Temperature dependence of the strength $\Delta\varepsilon$, position ω_0, and the width γ of the phonon due to the vibrations of Fe and As ions. Vertical dashed lines indicate the Néel transition temperatures of the Ca-, Sr-, and Ba-based compounds (gray, light blue, pink, respectively).

related to the electronic nematicity recently discovered in a doped compound of this class [229]. In addition, while the width and the position of the Fe-As phonon in both Sr- and Ba-doped compounds [Fig. 4.21(e), 4.21(f)] display essentially identical magnitude and behavior, those of the Ca-doped material are significantly larger. While the somewhat broader phonon feature could, in principle, be traced back to the quality of the sample surface or the sample itself, the harder Fe-As phonon of Ca-based compound compared to its Sr- and Ba-based counterparts must be intrinsic. Such a hardening most likely results from the shorter Ca-As and Fe-As bond lengths compared to those in the Sr- and Ba-based compounds and has also been observed in inelastic-neutron-scattering measurements on $CaFe_2As_2$, $BaFe_2As_2$ and predicted by ab-initio calculations [263].

Spin-density-wave-induced anomaly in the visible

Having investigated the SDW-induced anomalies in the infrared spectral range, let us turn to the charge dynamics in the 122 compounds at visible frequencies. [5] Recently, a criticality-induced suppression of an absorption band at energies, much higher than the corresponding energy gaps, has been reported in both the optimally doped superconducting $Ba_{0.68}K_{0.32}Fe_2As_2$ and the antiferromagnetic $SrFe_2As_2$ (Ref. 42). The analysis of the spectral-weight transfer across the SDW transition carried out in the same work, revealed that high energies up to 4 eV are involved in the spectral-weight redistribution and that the f-sum rule is fully satisfied above the suppressed absorption band in the visible spectral range. It appears to be of interest whether in other parent compounds of the same 122-type the SDW energetics is similar or rather shows a systematic variation with the atomic number of the intercalant within the class. To this end we have carried out accurate ellipsometric measurements in the visible spectral range to match the data quality of Ref. 42 and compare the intensity and location of the SDW-suppressed absorption bands, as well as the spectral-weight redistribution in the entire investigated spectral range, in all three parent compounds.

The results are presented in Fig. 4.22. Panels 4.22(a)–(c) show the difference real and imaginary parts of the dielectric function $\varepsilon(\omega) = 1 + 4\pi i\sigma(\omega)/\omega$ in the visible spectral range. The difference is taken between the temperatures above and below the material's Néel transition temperature: 160 K and 140 K, 200 K and 175 K, and 140 K and 120 K for $CaFe_2As_2$, $SrFe_2As_2$, and $BaFe_2As_2$, respectively. These spectra reveal a clear suppression of absorption at optical frequencies. The magnetostructurally induced character of this suppression is confirmed by drastic drop in the temperature dependence of the imaginary part of the dielectric function ε_2 at the Néel temperature, shown in the inset of Figs. 4.22(d), 4.22(f) for the Ca- and Sr-based compounds, respectively. The suppressed optical response of all three iron pnictides shown in Figs. 4.22(a)–(c) reveals the contribution of two absorption bands and the systematic evolution of their suppression intensities with the atomic number: the suppression of both bands reduces upon going from lighter to heavier intercalating atoms.

We now move to the analysis of the spectral-weight redistribution across the spin-density-wave transition presented in Figs. 4.22(d), 4.22(e), and 4.22(f) for the case of Ca-, Sr-, and Ba-based material, respectively. The energy-dependent spectral weight is defined as the integral of the real part of the

[5] To facilitate the comparison with previous work, in this section we use electron-volt instead of wavenumber as the unit of photon energy. The conversion factor between the two is 8066 $\mathrm{cm}^{-1}/\mathrm{eV}$.

optical conductivity $\sigma_1(\omega)$ up to a certain cut-off frequency Ω:

$$SW(\Omega) = \int_0^{\Omega} \sigma_1(\omega) d\omega.$$

Several common features can be identified in the energetics of the spin-density-wave transition: the spectral weight from below the optical spin-density-wave gap $2\Delta^{\mathrm{SDW}}$ [lowest-energy red area in Fig. 4.22(e) and corresponding areas in Figs. 4.22(d),(f)] is redistributed to energies directly above the optical gap [subsequent blue area in Fig. 4.22(e) and the corresponding areas in Figs. 4.22(d),(f)]. However, the spectral weight gained directly above the optical gap does not balance that lost within the gap, which implies that higher-energy processes beyond the characteristic magnetic energy scales proposed for these materials are affected by the spin-density-wave transition, including the spin-density-wave-suppressed band in the visible spectral range [higher-energy blue and red areas in Fig. 4.22(e) and the corresponding areas in Figs. 4.22(d),(f)]. Such a high-energy modification of the spectral weight might originate in a redistribution of the electronic population between several bands at the spin-density-wave transition, as suggested for $SrFe_2As_2$ in Ref. 42.

In contrast to the case of the phase transition, the temperature-induced spectral-weight transfer above the Néel temperature in $CaFe_2As_2$ (red solid line in Fig. 4.22d) leaves the low-energy itinerant-charge-carrier response largely unaffected and is dominated by the temperature dependence of the 0.5 eV absorption band, indicated with a blue arrow in Fig. 4.19a and analyzed in Table 4.5. The compensating effect due to the suppression of the 3.5 eV absorption band is entirely absent in the normal state and only a very weak decrease in the spectral weight at higher energies takes place, comparable to that across the SDW transition. The absence of any significant temperature dependence of the 3.5 eV absorption band above T_{N} is further confirmed by the temperature scan of the imaginary part of the dielectric function at 3.5 eV shown in the inset of Fig. 4.22d.

The above commonalities notwithstanding, it is clear from Figs. 4.22(d)–(f) that the overall intensity of the spectral-weight redistribution at the SDW transition decreases systematically with increasing atomic number of the intercalant even though the corresponding Néel temperatures do not reflect this behavior (T_{N} is almost the same in the Ca- and Ba-based compound, whereas the amplitude of the spectral-weight redistribution is more than three times larger).

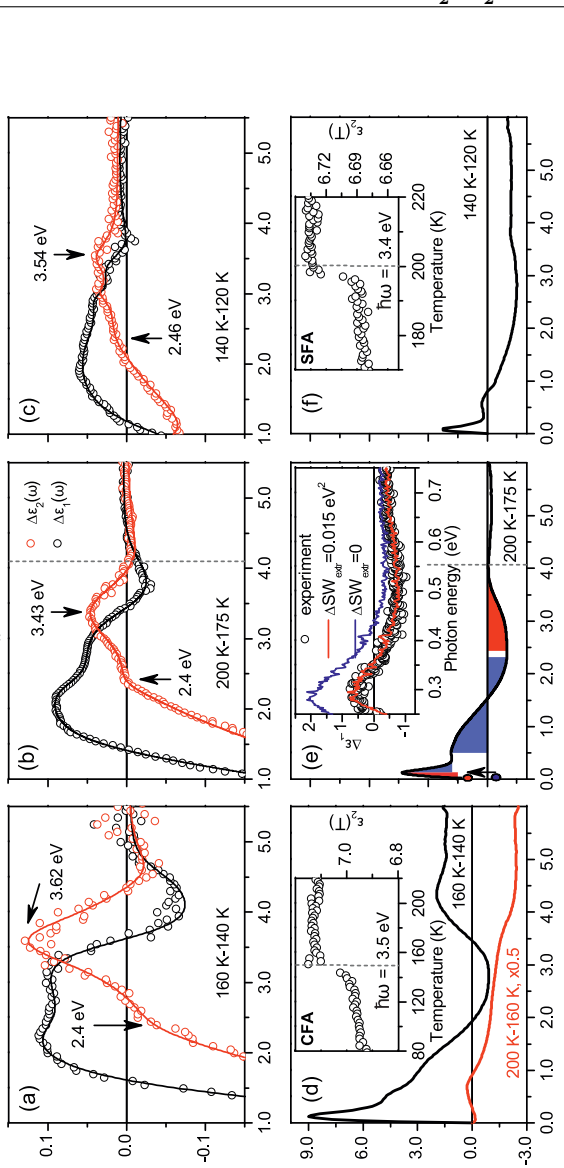

Figure 4.22: (a)–(c) Difference real and imaginary parts of the dielectric function $\Delta\varepsilon_1$, $\Delta\varepsilon_2$ in the visible spectral range between the temperatures above and below the Néel transition temperature, as specified in the panels. The arrows indicate the two SDW-suppressed absorption bands. (d)–(f) Spectral-weight redistribution between the same temperatures and in the same compounds as in (a)–(c) as a function of photon energy (black solid lines). Blue and red areas in (e) indicate the regions of spectral-weight gain and loss, respectively, in the magnetic versus the normal state. Red solid line in (d) shows the spectral-weight redistribution between 200 K and 160 K scaled by a factor of 0.5. [Inset in (e)], Real part of the dielectric function and the Kramers-Kronig transformations of the real part of the optical conductivity of $SrFe_2As_2$ with different amount of spectral weight contained in the extrapolation region at low frequencies (solid lines, colors match filled circles). [Insets in (d),(f)] Temperature scan of ε_2 in $CaFe_2As_2$ at 3.5 eV and in $SrFe_2As_2$ at 3.4 eV, respectively. Panel (e), the inset therein, as well as in (f). Partially adapted from Ref. 42

Itinerant charge carriers

Systematic trends similar to those found in the overall energetics of the 122 parent compounds investigated in this work can also be identified in the itinerant-charge-carrier response. However, whereas the former could be revealed already in the raw ellipsometric data, the extraction of the properties of the latter requires careful elimination of the interband contribution to the optical conductivity by means of a dispersion analysis (e.g. as carried out in Ref. 213), which allows one to isolate the inherent itinerant response. In the present work we have analyzed the free-charge-carrier and interband contributions in the standard Drude-Lorentz model.

In this method, the optical conductivity $\sigma(\omega) = \sigma_1(\omega) + i\sigma_2(\omega)$ or, equivalently, the full complex dielectric function $\varepsilon(\omega) = 1 + 4\pi i\sigma(\omega)/\omega$ (in CGS units) is fitted with an expression of the following form:

$$\varepsilon(\omega) = 1 - \sum_j \frac{\omega_{\mathrm{pl},j}^2}{\omega^2 + i\gamma_j\omega} + \sum_j \frac{\Delta\varepsilon_j\omega_{0j}^2}{(\omega_{0j}^2 - \omega^2) - i\Gamma_j\omega}, \tag{4.5}$$

where the first sum runs over all Drude and the second one over all Lorentz terms. $\omega_{\mathrm{pl},j}$ and γ_j are the plasma frequency and the quasiparticle scattering rate of the partial itinerant response and $\Delta\varepsilon_j$, ω_{0j}, Γ_j are the static permittivity contribution, the center frequency and the width of the Lorentzian oscillators used to model the interband transitions, respectively. The function in Eq. 4.5 is fitted simultaneously to the real and imaginary parts of the dielectric function.

The oscillator parameters obtained in such a fit for all three 122 parent compounds are summarized in Table 4.5. The contribution of the most important interband transitions to the real part of the optical conductivity is broken down in Figs. 4.23(a)–4.23(c) (red, green, and blue shaded areas) for the Ca-, Sr-, and Ba-based compounds, respectively, and their integral contribution to the real part of both the optical conductivity [black lines in Figs. 4.23(a)–4.23(c)] and the dielectric function [black lines in Figs. 4.23(d)–4.23(f)], as well as the extracted itinerant response (gray lines in all panels), is also shown. The overall structure of the interband transitions is very similar in all three compounds. The lowest clearly identifiable interband transition, previously found to be strongly renormalized with respect to the prediction of band-structure calculations and to give an unusually large contribution to the total zero-frequency interband permittivity $\Delta\varepsilon_{\mathrm{tot}}$ of the order of 60 in the optimally doped $Ba_{1-x}K_xFe_2As_2$ (see Ref. 213), shows a systematic softening with increasing atomic number of the intercalating atom, with a concomitant increase in $\Delta\varepsilon$. The evolution of the total zero-frequency interband permittivity $\Delta\varepsilon_{\mathrm{tot}}$ is relatively small and is dominated by that of the lowest interband transition, as can be inferred from the limiting zero-frequency behavior of the total interband

Table 4.5: Parameters of the Drude and Lorentzian terms in Eq. 4.5 obtained from the dispersion analysis of the optical conductivity of $CaFe_2As_2$, $SrFe_2As_2$, and $BaFe_2As_2$ at room and Néel temperature (shown for room temperature in Fig. 4.23).

	$CaFe_2As_2$			$SrFe_2As_2$			$BaFe_2As_2$		
j	$\Delta\varepsilon_j$	$\omega_{\mathrm{pl},j}$ ω_{0j} cm^{-1}	γ_j Γ_j cm^{-1}	$\Delta\varepsilon_j$	$\omega_{\mathrm{pl},j}$ ω_{0j} cm^{-1}	γ_j Γ_j cm^{-1}	$\Delta\varepsilon_j$	$\omega_{\mathrm{pl},j}$ ω_{0j} cm^{-1}	γ_j Γ_j cm^{-1}
				300 K					
Dru_1	—	4400	40	—	1960	156	—	2622	162
Dru_2	—	22 000	2960	—	17 340	2650	—	14 833	1717
$\mathrm{Dru}_{\mathrm{tot}}$	—	22 500	—	—	17 450	—	—	15 060	—
$\mathrm{Dru}_{\mathrm{KK}}$	—	22 000	—	—	17 895	—	—	15 300	—
L_1	35	6121	9683	40	5407	9167	46	4888	8200
L_2	14.25	18 592	36 627	13.8	19 138	37 238	12.7	18 930	33 539
L_3	0.68	31 035	16 374	0.397	31 325	17 580	0.27	31 483	20 992
L_4	2.35	58 810	44 568	2.47	58 087	39 548	2.57	53 464	38 045
L_5	1.35	113 407	3991	1.04	165 782	3102	1	80 467	3011
				T_{N}					
Dru_1	—	5900	40	—	2150	144	—	2300	600
Dru_2	—	20 475	2724	—	17 315	2785	—	13 212	1310
$\mathrm{Dru}_{\mathrm{tot}}$	—	21 308	—	—	17 448	—	—	13 410	—
$\mathrm{Dru}_{\mathrm{KK}}$	—	20 870	—	—	17 915	—	—	13 335	—
L_1	33.7	6353	9503	37.3	5614	8928	45	4986	7956
L_2	14.8	18 096	35 971	13.98	19 138	37 238	12.5	19 460	34 555
L_3	0.7	30 703	13 062	0.39	31 322	16 222	0.2	32 164	14 191
L_4	2.36	58 461	44 615	2.44	58 087	38 761	2.2	52 906	33 500
L_5	1.64	273 090	8172	0.92	138 292	2947	1.12	70 949	22 284

contribution to the real part of the dielectric function shown with black lines in Figs. 4.23(d)–4.23(f) and from Table 4.5.

The extracted itinerant response (gray lines in Fig. 4.23) can be broken down into a narrow and broad component (see Table 4.5) for all three compounds, in agreement with Ref. 174, which previously identified this phenomenon in essentially all known parent iron pnictides of the $ThCr_2Si_2$ type. In our Drude-Lorentz fit we excluded the lowest far-infrared spectral range strongly affected by the collective excitation in the Sr- and Ba-based compounds [gray shaded areas in Figs. 4.23(b), 4.23(c), 4.23(e), and 4.23(f)]. The two Drude contributions to the itinerant response are plotted in Fig. 4.23 as black dashed lines and their plasma frequencies and quasiparticle scattering rate are listed in Table 4.5.

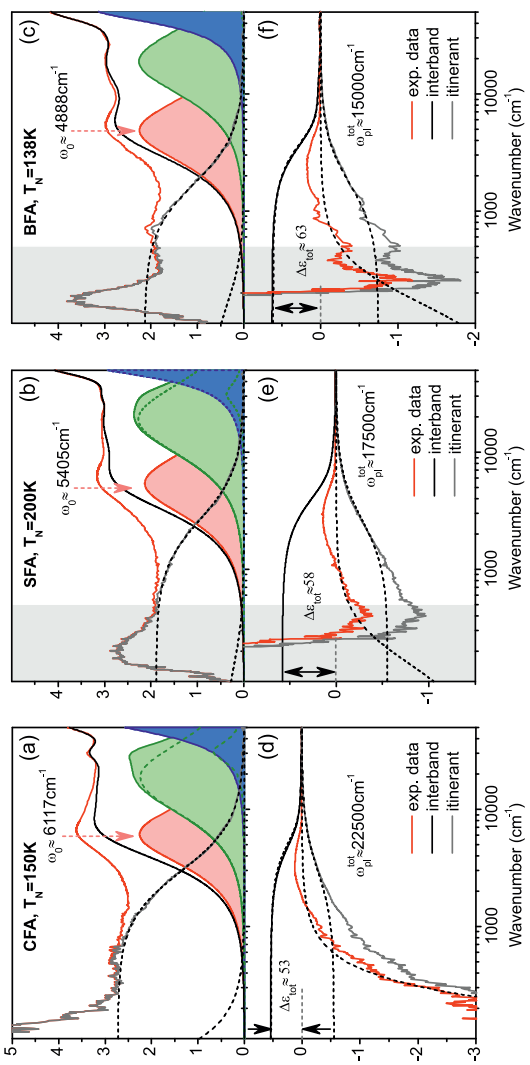

Figure 4.23: Real part of the optical conductivity (a)–(c) and dielectric function (d)–(f) of the Ca-, Sr-, and Ba-based compounds at 300 K (red line) and the corresponding interband [red, green, and blue areas in (a)–(c)] and itinerant (gray line) contributions obtained in a Drude-Lorentz dispersion analysis as described in the text. The partial Drude contributions are shown as black dashed lines. The lowest clearly identifiable absorption band is indicated with a pink arrow. Major partial Lorentz contributions to the absorption band in the visible (green area) are plotted as green dashed lines in (a)–(c). The total contribution of all interband transitions (black line). The gray-shaded area in (b), (c) and (e), (f) indicates the spectral range excluded from the Drude-Lorentz fit due to the presence of a low-energy collective excitation.

The total plasma frequency of the free electrons $\omega_{\rm pl}^{\rm tot} = \sqrt{\omega_{\rm pl,1}^2 + \omega_{\rm pl,2}^2}$ shows a systematic increase with decreasing atomic number of the intercalant and is significantly larger in $CaFe_2As_2$ than in the other two compounds (see Fig. 4.23 and Table 4.5). This trend is also weakly present in first-principles calculations of the plasma frequency [264] but is significantly enhanced by renormalization in the real materials.

To further confirm the values of the total plasma frequency inferred from our Drude-Lorentz fit, we carried out a Kramers-Kronig consistency analysis of ellipsometric data. This analytical technique, utilizing the unique capacity of ellipsometry to independently obtain the real and imaginary part of the dielectric function, [42] allows one to accurately determine the spectral weight contained in the extrapolation region at lowest frequencies and thus accurately measure the total plasma frequency of itinerant charge carriers. This is made possible by comparing the Kramers-Kronig transformation of the extrapolated real part of the optical conductivity with the independently obtained real part of the dielectric function, as shown in Fig. 4.22(e) and the inset therein. The total plasma frequencies for all three compounds obtained with this method are shown in Table 4.5. It is clear that the agreement between $\omega_{\rm pl}^{\rm tot}$ obtained using the Drude-Lorentz fit and by means of a Kramers-Kronig consistency check is remarkable. It should be noted that the accuracy of the Kramers-Kronig consistency check in determining the total spectral weight and thus plasma frequency is extremely high (below 0.5% in the present case) and this approach only very weakly depends on the shape of extrapolation [42].

The systematic enhancement of the itinerant response with decreasing atomic number of the intercalant, together with the results of the previous sections, shows that in $CaFe_2As_2$ a number of electronic properties are significantly enhanced compared to its Sr- and Ba-based counterparts.

4.3.3 Conclusions

In summary, we have reported a systematic comparison of the charge dynamics in three representative parent compounds of 122-type iron-based superconductors ($CaFe_2As_2$, $SrFe_2As_2$, and $BaFe_2As_2$) in a broad spectral range as well as a detailed temperature dependence of their far-infrared conductivity. We identified two SDW energy gaps in all three compounds, with a significantly stronger coupling in the Ca-based material within both SDW subsystems as compared to the other two compounds, in which the larger gap decreases systematically with increasing atomic number of the intercalant. Our detailed temperature measurements of the far-infrared conductivity of the three compounds allowed us to accurately track the temperature dependence of both SDW gaps and reveal an anomaly in $CaFe_2As_2$ in the energy range of the smaller gap at $T^* \approx 80$ K, well below the Néel temperature of this compound.

The presence of this remnant transition implies that the two SDW subsystems are very weakly coupled to one another. A comparison to the temperature dependence of the far-infrared conductivity of $SrFe_2As_2$ and $BaFe_2As_2$ shows a clear evolution of this coupling from weak in the Ca-based compound via intermediate in the Sr-based to strong in the Ba-based material. The temperature dependence of the infrared phonons reveals a clear anomaly at T_N in all three compounds, whereby the SDW-induced modifications of the phonon properties set in exactly at T_N in both Ba- and Sr-based materials but at somewhat higher temperatures in $CaFe_2As_2$, suggesting the early development of SDW fluctuations and their sizable impact on the lattice. The temperature dependence of the intensity $\Delta\varepsilon_0$ of the Ca-related phonon shows a possible signature of T^*. Similarly to the previously reported SDW-induced suppression of two absorption bands in $SrFe_2As_2$, we find an analogous effect in both Ca- and Ba-based compounds, as well as a systematic evolution of the intensity of the suppression with the atomic number of the intercalant. The investigation of the spectral-weight transfer induced by the SDW transition reveals that in all three parent compounds energies much larger than the characteristic magnetic energy scales proposed for these materials are involved. This high-energy modification of the spectral weight might originate in a redistribution of the electronic population between several bands at the transition. Our accurate dispersion analysis of the independently obtained real and imaginary parts of the optical conductivity by means of spectroscopic ellipsometry reveals a strongly enhanced plasma frequency in $CaFe_2As_2$, decreasing systematically with increasing atomic number of the intercalating atom. Our results single out $CaFe_2As_2$ in the class of $ThCr_2Si_2$-type iron-based materials by demonstrating the existence of two weakly coupled but extremely metallic electronic subsystems. Since the three investigated materials are driven superconducting upon doping, our results may provide insights into the physics of the related superconductors.

5 Summary

In this final chapter we briefly summarize our results which we have obtained on strongly correlated electron systems by means of a fruitful cooperation of broad band spectroscopic ellipsometry and *ab initio* electronic band structure calculations in the framework of density functional theory. We make use of the capabilities of optical spectroscopy to assess the electronic correlations encoded in the materials specific complex dielectric function. The general notion that electronic correlations have to have just the right strength to lead to the most interesting and in many cases still puzzling phenomena suggests that a systematic reduction in the strength of the leading correlations opens up the chance for competition with other electronic interactions and hence novel properties. Therefore we have focused on two material classes where reduced Coulomb interactions due to an increased single particle bandwidth foster this interplay.

First, we investigated two iridium oxide compounds where the spatially extended nature of the $5d$ valence states promotes interesting competition of enhanced spin-orbit interactions and reduced Coulomb repulsion. We study the prototype of this family, Sr_2IrO_4, in order to further explore the proposed $J_{\text{eff}} = 1/2$ isospin ground state which is believed to bear the essence of the physics in the iridium oxides. By extracting the full complex dielectric function in the range of 12 meV to 6.5 eV from the ellipsometric measurements while the in-plane response reproduces the reported results we are able to disclose a strong anisotropy in the optical response between ab-plane and the c-axis. The sharp infrared interband transitions, key features of the in-plane optical response and attributed to the manifestation of the $J_{\text{eff}} = 1/2$ state, are strongly suppressed and a large direct optical gap of ~ 2 eV is observed. Fully relativistic band structure calculations support this observation to be consistent with the $J_{\text{eff}} = 1/2$ ground state. A indirect optical gap of about 0.2 eV gives rise to a low, but finite phonon enhanced absorption below the direct gap in the c-axis response. We determine the anisotropic infrared active phonon spectrum to be consistent with group symmetry considerations and lattice dynamics calculations which supports the validity of the obtained spectra.

Having our understanding of the $J_{\text{eff}} = 1/2$ ground state improved we moved on to explore the influence of geometrical frustration on this concept. We have studied only recently grown single crystals of the hyperkagome compound $Na_3Ir_3O_8$, a semi-metallic counterpart of $Na_4Ir_3O_8$, which is one of the best candidates to realize a three-dimensional spin liquid ground state. In the far

infrared spectrum all detected phonon resonances exhibit a highly asymmetric line shape and their oscillator strength follows closely the strong temperature dependence of the background. By comparing the experimental spectra to fully relativistic band structure calculations we identify the low energy interband transitions responsible for the background. A negative band gap establishes the semimetallic state and might provide an explanation for the unusual strong temperature dependence of the low energy excitations due to phonon mediated indirect interband transition. Therefore we attribute the strong asymmetry to the quantum mechanical Fano interference of discrete phonon states with the electron-hole excitation continuum. We quantify its impact by the Fano parameter q. For the strongest modes we find $q \sim -1.5$ at low temperatures. In consideration of non-negligible intrinsic dipole moments these small values of q require a finite electron-phonon coupling to be present in this system. Despite its importance to the physics in the 3*d*-electron counterparts, electron-phonon coupling in the 5*d* iridium oxides had not been addressed so far. Due to the small crystal size and the high absorption cross section neutron scattering experiments are not yet feasible on this material. Since the Ir hyperkagome sub-lattice is essentially identical in both $Na_3Ir_3O_8$ and $Na_4Ir_3O_8$ – in the latter the additional Na atoms on the interstitial lattice sites serve mainly as a doping reservoir – our results might also be relevant to the latter.

The phase diagram of the recently discovered metallic iron-pnictides with superconductivity emerging upon suppression of the strongly correlated antiferromagnetic state, emphasizes the crucial role of fine tuning of the electronic correlations in this material class. Therefore we have focused on isovalent substitution in the $ThCr_2Si_2$-type family to study the influence of structural modifications on the low energy band structure in absence of additional charge doping.

We investigate 4*d* Ru substitution for 3*d* Fe in $Ba(Fe_{1-x}Ru_x)_2As_2$ and report for the first time the normal state in-plane optical response for a large doping range $0 \leq x \leq 0.74$, which covers all relevant segments in the phase diagram: spin-density wave phase, superconductivity and overdoped, paramagnetic, metallic phase. Making use of the capabilities of ellipsometry to determine both real and imaginary part of the dielectric function we infer the spectral weight and hence the (unscreened) plasma frequency ω_{pl} associated with the itinerant charge carrier response disentangled from the low energy interband transitions within the Fe-*d* bands. We clearly distinguish two regimes in the optical response: in the underdoped regime (Ru content $x \lesssim 0.35$) ω_{pl} and the static permittivity $\Delta\varepsilon_{\mathrm{MIR}}$ descending from the mid infrared interband transitions remain almost constant, whereas in the overdoped region ($x \gtrsim 0.35$) where superconductivity is quickly suppressed ω_{pl} shows a strong increase and $\Delta\varepsilon_{\mathrm{MIR}}$ a suppression. The latter might be relevant to superconductivity in the presence of redistribution of the band populations upon entering the super-

conducting state, as observed in optimally doped $Ba_{0.64}K_{0.36}Fe_2As_2$ [42]. By gauging the experimentally obtained plasma frequency by its LDA counterpart, $(\omega_{\rm pl}^{\rm exp}/\omega_{\rm pl}^{\rm LDA})^2$, we detect a monotonous reduction in the electronic correlations with increasing Ru content x. Our findings are fully consistent with both experimental ARPES [201] and theoretical LDA studies [92] which show strong evolution in the Fermi surface topology setting in only in the overdoped regime.

The series of parent compounds AFe_2As_2 (A = Ca , Sr, Ba) can to some extend also be considered as a extreme case of "isoelectronic" doping which influences the electronic correlations by structural modifications due to the different atomic radii (from Ca-4s to Ba-6s configuration). We undertake a comprehensive optical study of the evolution in the charge dynamics in this series. From a detailed temperature dependence on all three compounds we are able to identify two optical gaps of different size which we associate with two coupled spin-density wave subsystems. The coupling within the spin-density wave subsystems is significantly stronger in the Ca-based material compared to Sr and Ba compounds and The coupling strength between these subsystems develops systematically from weak in the case of the Ca intercalant via intermediate for Sr and to strong in the Ba-based compound. The weak coupling regime in $CaFe_2As_2$ is implied by an anomaly in the energy range of the smaller gap at $T^* \approx 80$ K, well below the Néel temperature of this compound. Resonance frequency and strength of the infrared phonons experience a clear shift at $T_{\rm N}$ in all three compounds, whereby the modifications set in exactly at $T_{\rm N}$ in both Ba- and Sr-based materials but at somewhat higher temperatures in $CaFe_2As_2$, suggesting the early development of spin-density–wave fluctuations and their sizable impact on the lattice. The temperature dependence of the intensity $\Delta\varepsilon_0$ of the Ca-related phonon shows a possible signature of T^*. Similarly to the previously reported spin-density-wave-induced suppression of two absorption bands in $SrFe_2As_2$, we find an analogous effect in both Ca- and Ba-based compounds, as well as a systematic evolution of the intensity of the suppression with the atomic number of the intercalant. Redistribution of the electronic population between several bands at the transition might be responsible for the spectral weight redistribution at energies much larger than the characteristic magnetic energy scales. Our results single out $CaFe_2As_2$ in the class of $ThCr_2Si_2$-type iron-based materials by demonstrating the existence of two weakly coupled but extremely metallic electronic subsystems. Since the three investigated materials are driven superconducting upon doping, our results may provide insights into the physics of the related superconductors.

Bibliography

[1] M. Imada, A. Fujimori, and Y. Tokura, Rev. Mod. Phys. **70**, 1039 (1998).

[2] B. J. Kim, H. Jin, S. J. Moon, J.-Y. Kim, B.-G. Park, C. S. Leem, J. Yu, T. W. Noh, C. Kim, S.-J. Oh, J.-H. Park, V. Durairaj, G. Cao, and E. Rotenberg, Phys. Rev. Lett. **101**, 076402 (2008).

[3] Y. Okamoto, M. Nohara, H. Aruga-Katori, and H. Takagi, Phys. Rev. Lett. **99**, 137207 (2007).

[4] J. Bardeen, L. N. Cooper, and J. R. Schrieffer, Phys. Rev. **108**, 1175 (1957).

[5] F. Bloch, Zeitschrift für Physik **57**, 545 (1929).

[6] A. H. Wilson, Proceedings of the Royal Society of London. Series A **133**, 458 (1931).

[7] N. F. Mott and R. Peierls, Proceedings of the Physical Society **49**, 72 (1937).

[8] N. F. Mott, Proceedings of the Physical Society. Section A **62**, 416 (1949).

[9] N. F. Mott, Philosophical Magazine **6**, 287 (1961).

[10] A. G. Gavriliuk, I. A. Trojan, and V. V. Struzhkin, Phys. Rev. Lett. **109**, 086402 (2012).

[11] J. G. Bednorz and K. A. Müller, Zeitschrift fur Physik B Condensed Matter **64**, 189 (1986).

[12] Y. Tokura and N. Nagaosa, Science **288**, 462 (2000).

[13] Y. K. Kato, R. C. Myers, A. C. Gossard, and D. D. Awschalom, Science **306**, 1910 (2004).

[14] M. König, S. Wiedmann, C. Brüne, A. Roth, H. Buhmann, L. W. Molenkamp, X.-L. Qi, and S.-C. Zhang, Science **318**, 766 (2007).

[15] J. Chaloupka, G. Jackeli, and G. Khaliullin, Phys. Rev. Lett. **105**, 027204 (2010).

[16] J. Chaloupka, G. Jackeli, and G. Khaliullin, Phys. Rev. Lett. **110**, 097204 (2013).

[17] H. Kamerlingh Onnes, Commun. Phys. Lab. Univ. Leiden **12**, 120 (1911).

[18] V. L. Ginzburg and L. D. Landau, Zh. Eksp. Teor. Fiz. **20**, 1064 (1950).

[19] J. Bardeen, L. N. Cooper, and J. R. Schrieffer, Phys. Rev. **106**, 162 (1957).

[20] G. Ghiringhelli, M. Le Tacon, M. Minola, S. Blanco-Canosa, C. Mazzoli, N. B. Brookes, G. M. De Luca, A. Frano, D. G. Hawthorn, F. He, T. Loew, M. M. Sala, D. C. Peets, M. Salluzzo, E. Schierle, R. Sutarto, G. A. Sawatzky, E. Weschke, B. Keimer, and L. Braicovich, Science **337**, 821 (2012).

[21] Y. Kamihara, T. Watanabe, M. Hirano, and H. Hosono, Journal of the American Chemical Society **130**, 3296 (2008).

[22] D. N. Basov and A. V. Chubukov, Nat Phys **7**, 272 (2011).

[23] M. Dressel and G. Grüner, *Electrodynamics of solids: optical properties of electrons in matter* (Cambridge University Press, 2002).

[24] P. Drude, Annalen der Physik **274**, 265 (1889).

[25] P. Drude, Annalen der Physik **275**, 481 (1890).

[26] J. D. Jackson, *Classical Electrodynamics*, 3rd ed. (Wiley, 1998).

[27] U. Fano, Phys. Rev. **124**, 1866 (1961).

[28] A. E. Miroshnichenko, S. Flach, and Y. S. Kivshar, Rev. Mod. Phys. **82**, 2257 (2010).

[29] A. B. Kuzmenko, L. Benfatto, E. Cappelluti, I. Crassee, D. van der Marel, P. Blake, K. S. Novoselov, and A. K. Geim, Phys. Rev. Lett. **103**, 116804 (2009).

[30] E. Cappelluti, L. Benfatto, and A. B. Kuzmenko, Phys. Rev. B **82**, 041402 (2010).

[31] E. Cappelluti, L. Benfatto, M. Manzardo, and A. B. Kuzmenko, Phys. Rev. B **86**, 115439 (2012).

[32] A. Damascelli, K. Schulte, D. van der Marel, and A. A. Menovsky, Phys. Rev. B **55**, R4863 (1997).

[33] A. S. Barker and J. J. Hopfield, Phys. Rev. **135**, A1732 (1964).

[34] J. Humlíček, R. Henn, and M. Cardona, Phys. Rev. B **61**, 14554 (2000).

[35] V. Burlakov, S. Shulga, J. Keller, and K. Renk, Physica C: Superconductivity **190**, 304 (1992).

[36] S. Bar-Ad, P. Kner, M. V. Marquezini, S. Mukamel, and D. S. Chemla, Phys. Rev. Lett. **78**, 1363 (1997).

[37] M. L. Goldberger and K. M. Watson, *Collision theory* (Wiley, New York, 1964).

[38] R. Kubo, J. Phys. Soc. Jpn. **12**, 570 (1957).

[39] D. Baeriswyl, C. Gros, and T. M. Rice, Phys. Rev. B **35**, 8391 (1987).

[40] W. Götze and P. Wölfle, Phys. Rev. B **6**, 1226 (1972).

[41] M. M. Qazilbash, J. J. Hamlin, R. E. Baumbach, L. Zhang, D. J. Singh, M. B. Maple, and D. N. Basov, Nat Phys **5**, 647 (2009).

[42] A. Charnukha, P. Popovich, Y. Matiks, D. L. Sun, C. T. Lin, A. N. Yaresko, B. Keimer, and A. V. Boris, Nature Communications **2**, 219 (2011).

[43] M. Tinkham, *Introduction to superconductivity* (Mcgraw-Hill Publishing Co, 1996).

[44] R. M. A. Azzam and N. M. Bashara, *Ellipsometry and Polarized Light* (North-Holland Pub. Co., 1977).

[45] H. Tompkins and E. A. Haber, eds., *Handbook of Ellipsometry* (William Andrew, 2006).

[46] R. T. Holm, *Handbook of optical constanants of solids*, edited by E. D. Palik, Vol. 2 (Academic Press, 1991).

[47] M. Dressel, B. Gompf, D. Faltermeier, A. K. Tripathi, J. Pflaum, and M. Schubert, Opt. Express **16**, 19770 (2008).

[48] A. Roeseler, *Infrared Spectroscopic Ellipsometry* (Akademie-Verlag, Berlin,

1990).

[49] C. Bernhard, J. Humlíček, and B. Keimer, Thin Solid Films **455–456**, 143 (2004).

[50] T. N. Stanislavchuk, T. D. Kang, P. D. Rogers, E. C. Standard, R. Basistyy, A. M. Kotelyanskii, G. Nita, T. Zhou, G. L. Carr, M. Kotelyanskii, and A. A. Sirenko, Review of Scientific Instruments **84**, 023901 (2013).

[51] F. Münz, J. Humlíček, and P. Maršík, Thin Solid Films **519**, 2703 (2011), 5th International Conference on Spectroscopic Ellipsometry (ICSE-V).

[52] E. Dagotto, Science **309**, 257 (2005).

[53] W. Witczak-Krempa, G. Chen, Y. B. Kim, and L. Balents, Annual Review of Condensed Matter Physics **5**, 57 (2014).

[54] L. F. Mattheiss, Phys. Rev. B **13**, 2433 (1976).

[55] T. Mizokawa and A. Fujimori, Phys. Rev. B **54**, 5368 (1996).

[56] M. Ge, T. F. Qi, O. B. Korneta, D. E. De Long, P. Schlottmann, W. P. Crummett, and G. Cao, Phys. Rev. B **84**, 100402 (2011).

[57] B. J. Kim, H. Ohsumi, T. Komesu, S. Sakai, T. Morita, H. Takagi, and T. Arima, Science **323**, 1329 (2009).

[58] J. Kim, D. Casa, M. H. Upton, T. Gog, Y.-J. Kim, J. F. Mitchell, M. van Veenendaal, M. Daghofer, J. van den Brink, G. Khaliullin, and B. J. Kim, Phys. Rev. Lett. **108**, 177003 (2012).

[59] G. Jackeli and G. Khaliullin, Phys. Rev. Lett. **102**, 017205 (2009).

[60] A. Shitade, H. Katsura, J. Kuneš, X.-L. Qi, S.-C. Zhang, and N. Nagaosa, Phys. Rev. Lett. **102**, 256403 (2009).

[61] S. K. Choi, R. Coldea, A. N. Kolmogorov, T. Lancaster, I. I. Mazin, S. J. Blundell, P. G. Radaelli, Y. Singh, P. Gegenwart, K. R. Choi, S.-W. Cheong, P. J. Baker, C. Stock, and J. Taylor, Phys. Rev. Lett. **108**, 127204 (2012).

[62] R. Comin, G. Levy, B. Ludbrook, Z.-H. Zhu, C. N. Veenstra, J. A. Rosen, Y. Singh, P. Gegenwart, D. Stricker, J. N. Hancock, D. van der Marel, I. S. Elfimov, and A. Damascelli, Phys. Rev. Lett. **109**, 266406 (2012).

[63] H. Gretarsson, J. P. Clancy, X. Liu, J. P. Hill, E. Bozin, Y. Singh, S. Manni, P. Gegenwart, J. Kim, A. H. Said, D. Casa, T. Gog, M. H. Upton, H.-S. Kim, J. Yu, V. M. Katukuri, L. Hozoi, J. van den Brink, and Y.-J. Kim, Phys. Rev. Lett. **110**, 076402 (2013).

[64] G. Cao, J. Bolivar, S. McCall, J. E. Crow, and R. P. Guertin, Phys. Rev. B **57**, R11039 (1998).

[65] N. Ashcroft and N. Mermin, *Solid State Physics* (Saunders College, Philadelphia, 1976).

[66] S. J. Moon, M. W. Kim, K. W. Kim, Y. S. Lee, J.-Y. Kim, J.-H. Park, B. J. Kim, S.-J. Oh, S. Nakatsuji, Y. Maeno, I. Nagai, S. I. Ikeda, G. Cao, and T. W. Noh, Phys. Rev. B **74**, 113104 (2006).

[67] S. J. Moon, H. Jin, K. W. Kim, W. S. Choi, Y. S. Lee, J. Yu, G. Cao, A. Sumi, H. Funakubo, C. Bernhard, and T. W. Noh, Phys. Rev. Lett. **101**, 226402 (2008).

[68] Y. Liu, New Journal of Physics **12**, 075001 (2010).

[69] T. Takayama, A. Matsumoto, J. Nuss, A. Yaresko, K. Ishii, M. Yoshida, J. Mizuki, and H. Takagi, ArXiv e-prints (2013), arXiv:1311.2885 .

[70] L. Balents, Nature **464**, 199 (2010).

[71] H. Zhang, K. Haule, and D. Vanderbilt, Phys. Rev. Lett. **111**, 246402 (2013).

[72] Q. Huang, J. Soubeyroux, O. Chmaissem, I. Sora, A. Santoro, R. Cava, J. Krajewski, and W. Peck Jr., Journal of Solid State Chemistry **112**, 355 (1994).

[73] M. K. Crawford, M. A. Subramanian, R. L. Harlow, J. A. Fernandez-Baca, Z. R. Wang, and D. C. Johnston, Phys. Rev. B **49**, 9198 (1994).

[74] F. Ye, S. Chi, B. C. Chakoumakos, J. A. Fernandez-Baca, T. Qi, and G. Cao, Phys. Rev. B **87**, 140406 (2013).

[75] C. Dhital, T. Hogan, Z. Yamani, C. de la Cruz, X. Chen, S. Khadka, Z. Ren, and S. D. Wilson, Phys. Rev. B **87**, 144405 (2013).

[76] S. Chikara, O. Korneta, W. P. Crummett, L. E. DeLong, P. Schlottmann, and G. Cao, Phys. Rev. B **80**, 140407 (2009).

[77] H. Watanabe, T. Shirakawa, and S. Yunoki, Phys. Rev. Lett. **105**, 216410 (2010).

[78] B. H. Kim, G. Khaliullin, and B. I. Min, Phys. Rev. Lett. **109**, 167205 (2012).

[79] Q. Li, G. Cao, S. Okamoto, J. Yi, W. Lin, B. C. Sales, J. Yan, R. Arita, J. KuneÅ¡, A. V. Kozhevnikov, A. G. Eguiluz, M. Imada, Z. Gai, M. Pan, and D. G. Mandrus, Sci. Rep. **3**, (2013).

[80] D. Hsieh, F. Mahmood, D. H. Torchinsky, G. Cao, and N. Gedik, Phys. Rev. B **86**, 035128 (2012).

[81] R. Arita, J. Kuneš, A. V. Kozhevnikov, A. G. Eguiluz, and M. Imada, Phys. Rev. Lett. **108**, 086403 (2012).

[82] J. Dai, E. Calleja, G. Cao, and K. McElroy, ArXiv e-prints (2013), arXiv:1303.3688 .

[83] S. J. Moon, H. Jin, W. S. Choi, J. S. Lee, S. S. A. Seo, J. Yu, G. Cao, T. W. Noh, and Y. S. Lee, Phys. Rev. B **80**, 195110 (2009).

[84] D. J. Evans and S. Ushioda, Phys. Rev. B **9**, 1638 (1974).

[85] E. Kroumova, M. Aroyo, J. Perez-Mato, A. Kirov, C. Capillas, S. Ivantchev, and H. Wondratschek, Phase Transitions **76**, 155 (2003).

[86] L. Pintschovius, J. M. Bassat, P. Odier, F. Gervais, G. Chevrier, W. Reichardt, and F. Gompf, Phys. Rev. B **40**, 2229 (1989).

[87] M. Höppner, Private communications (2014).

[88] M. F. Cetin, P. Lemmens, V. Gnezdilov, D. Wulferding, D. Menzel, T. Takayama, K. Ohashi, and H. Takagi, Phys. Rev. B **85**, 195148 (2012).

[89] P. Y. Yu and M. Cardona, *Fundamentals of Semiconductors: Physics and Materials Properties* (Springer, Berlin, 2005).

[90] J. Nichols, O. B. Korneta, J. Terzic, L. E. De Long, G. Cao, J. W. Brill, and S. S. A. Seo, Applied Physics Letters **103**, 131910 (2013).

[91] T. Shimura, Y. Inaguma, T. Nakamura, M. Itoh, and Y. Morii, Phys. Rev. B **52**, 9143 (1995).

[92] Q. Wang, Y. Cao, J. A. Waugh, S. R. Park, T. F. Qi, O. B. Korneta, G. Cao,

and D. S. Dessau, Phys. Rev. B **87**, 245109 (2013).

[93] T. M. Holden, W. J. L. Buyers, E. C. Svensson, R. A. Cowley, M. T. Hutchings, D. Hukin, and R. W. H. Stevenson, Journal of Physics C: Solid State Physics **4**, 2127 (1971).

[94] J. Wagner and M. Cardona, Phys. Rev. B **32**, 8071 (1985).

[95] M. J. Rice, N. O. Lipari, and S. Strässler, Phys. Rev. Lett. **39**, 1359 (1977).

[96] T.-T. Tang, Y. Zhang, C.-H. Park, B. Geng, C. Girit, Z. Hao, M. C. Martin, A. Zettl, M. F. Crommie, S. G. Louie, Y. R. Shen, and F. Wang, Nat Nano **5**, 32 (2010).

[97] Z. Liu, X. Lu, P. Peng, W. Wu, S.-S. Pei, Q. Yu, and J. Bao, Phys. Rev. B **82**, 155435 (2010).

[98] Z. Li, C. H. Lui, E. Cappelluti, L. Benfatto, K. F. Mak, G. L. Carr, J. Shan, and T. F. Heinz, Phys. Rev. Lett. **108**, 156801 (2012).

[99] C. H. Lui, E. Cappelluti, Z. Li, and T. F. Heinz, Phys. Rev. Lett. **110**, 185504 (2013).

[100] M. J. Lawler, H.-Y. Kee, Y. B. Kim, and A. Vishwanath, Phys. Rev. Lett. **100**, 227201 (2008).

[101] M. J. Lawler, A. Paramekanti, Y. B. Kim, and L. Balents, Phys. Rev. Lett. **101**, 197202 (2008).

[102] Y. Zhou, P. A. Lee, T.-K. Ng, and F.-C. Zhang, Phys. Rev. Lett. **101**, 197201 (2008).

[103] D. Podolsky, A. Paramekanti, Y. B. Kim, and T. Senthil, Phys. Rev. Lett. **102**, 186401 (2009).

[104] T. Micklitz and M. R. Norman, Phys. Rev. B **81**, 174417 (2010).

[105] M. R. Norman and T. Micklitz, Phys. Rev. B **81**, 024428 (2010).

[106] D. Podolsky and Y. B. Kim, Phys. Rev. B **83**, 054401 (2011).

[107] J. Humlíček and C. Bernhard, Thin Solid Films **455–456**, 177 (2004).

[108] O. K. Andersen, Phys. Rev. B **12**, 3060 (1975).

[109] V. N. Antonov, B. N. Harmon, and A. N. Yaresko, *Electronic Structure and Magneto-Optical Properties of Solids* (Kluwer Academic Publishers, Dordrecht, 2004).

[110] D. Menzel, P. Popovich, N. N. Kovaleva, J. Schoenes, K. Doll, and A. V. Boris, Phys. Rev. B **79**, 165111 (2009).

[111] K. Ishizaka, M. S. Bahramy, H. Murakawa, M. Sakano, T. Shimojima, T. Sonobe, K. Koizumi, S. Shin, H. Miyahara, A. Kimura, K. Miyamoto, T. Okuda, H. Namatame, M. Taniguchi, R. Arita, N. Nagaosa, K. Kobayashi, Y. Murakami, R. Kumai, Y. Kaneko, Y. Onose, and Y. Tokura, Nature Materials **10**, 521 (2011).

[112] J. S. Lee, G. A. H. Schober, M. S. Bahramy, H. Murakawa, Y. Onose, R. Arita, N. Nagaosa, and Y. Tokura, Phys. Rev. Lett. **107**, 117401 (2011).

[113] Y. Kamihara, H. Hiramatsu, M. Hirano, R. Kawamura, H. Yanagi, T. Kamiya, and H. Hosono, J. Am. Chem. Soc. **128**, 10012 (2006).

[114] C. Wang, L. Li, S. Chi, Z. Zhu, Z. Ren, Y. Li, Y. Wang, X. Lin, Y. Luo, S. Jiang,

X. Xu, G. Cao, and Z. Xu, EPL (Europhysics Letters) **83**, 67006 (2008).

[115] G. Wu, Y. L. Xie, H. Chen, M. Zhong, R. H. Liu, B. C. Shi, Q. J. Li, X. F. Wang, T. Wu, Y. J. Yan, J. J. Ying, and X. H. Chen, Journal of Physics: Condensed Matter **21**, 142203 (2009).

[116] M. Rotter, M. Tegel, D. Johrendt, I. Schellenberg, W. Hermes, and R. Pöttgen, Phys. Rev. B **78**, 020503 (2008).

[117] D. C. Johnston, Advances in Physics **59**, 803 (2010).

[118] G. R. Stewart, Rev. Mod. Phys. **83**, 1589 (2011).

[119] I. I. Mazin, Nature **464**, 183 (2010).

[120] R. M. Fernandes, A. V. Chubukov, and J. Schmalian, Nat Phys **10**, 97 (2014).

[121] J. Paglione and R. L. Greene, Nat Phys **6**, 645 (2010).

[122] P. C. Canfield and S. L. Bud'ko, Annual Review of Condensed Matter Physics **1**, 27 (2010).

[123] P. Dai, J. Hu, and E. Dagotto, Nat Phys **8**, 709 (2012).

[124] P. J. Hirschfeld, M. M. Korshunov, and I. I. Mazin, Reports on Progress in Physics **74**, 124508 (2011).

[125] D. J. Scalapino, Rev. Mod. Phys. **84**, 1383 (2012).

[126] C. W. Chu, Nat Phys **5**, 787 (2009).

[127] N. Ni, S. Nandi, A. Kreyssig, A. I. Goldman, E. D. Mun, S. L. Bud'ko, and P. C. Canfield, Phys. Rev. B **78**, 014523 (2008).

[128] G.-F. Chen, Z. Li, G. Li, W.-Z. Hu, J. Dong, J. Zhou, X.-D. Zhang, P. Zheng, N.-L. Wang, and J.-L. Luo, Chinese Physics Letters **25**, 3403 (2008).

[129] J. T. Park, D. S. Inosov, A. Yaresko, S. Graser, D. L. Sun, P. Bourges, Y. Sidis, Y. Li, J.-H. Kim, D. Haug, A. Ivanov, K. Hradil, A. Schneidewind, P. Link, E. Faulhaber, I. Glavatskyy, C. T. Lin, B. Keimer, and V. Hinkov, Phys. Rev. B **82**, 134503 (2010).

[130] M. Rotter, M. Tegel, and D. Johrendt, Phys. Rev. Lett. **101**, 107006 (2008).

[131] A. S. Sefat, R. Jin, M. A. McGuire, B. C. Sales, D. J. Singh, and D. Mandrus, Phys. Rev. Lett. **101**, 117004 (2008).

[132] J.-H. Chu, J. G. Analytis, C. Kucharczyk, and I. R. Fisher, Phys. Rev. B **79**, 014506 (2009).

[133] L. J. Li, Y. K. Luo, Q. B. Wang, H. Chen, Z. Ren, Q. Tao, Y. K. Li, X. Lin, M. He, Z. W. Zhu, G. H. Cao, and Z. A. Xu, New Journal of Physics **11**, 025008 (2009).

[134] P. L. Alireza, Y. T. C. Ko, J. Gillett, C. M. Petrone, J. M. Cole, G. G. Lonzarich, and S. E. Sebastian, Journal of Physics: Condensed Matter **21**, 012208 (2009).

[135] E. Colombier, S. L. Bud'ko, N. Ni, and P. C. Canfield, Phys. Rev. B **79**, 224518 (2009).

[136] S. Jiang, H. Xing, G. Xuan, C. Wang, Z. Ren, C. Feng, J. Dai, Z. Xu, and G. Cao, Journal of Physics: Condensed Matter **21**, 382203 (2009).

[137] F. Rullier-Albenque, D. Colson, A. Forget, P. Thuéry, and S. Poissonnet, Phys. Rev. B **81**, 224503 (2010).

[138] A. Thaler, N. Ni, A. Kracher, J. Q. Yan, S. L. Bud'ko, and P. C. Canfield, Phys. Rev. B **82**, 014534 (2010).

[139] S. Avci, O. Chmaissem, D. Y. Chung, S. Rosenkranz, E. A. Goremychkin, J. P. Castellan, I. S. Todorov, J. A. Schlueter, H. Claus, A. Daoud-Aladine, D. D. Khalyavin, M. G. Kanatzidis, and R. Osborn, Phys. Rev. B **85**, 184507 (2012).

[140] Z. Li, R. Zhou, Y. Liu, D. L. Sun, J. Yang, C. T. Lin, and G.-q. Zheng, Phys. Rev. B **86**, 180501 (2012).

[141] K. Hashimoto, K. Cho, T. Shibauchi, S. Kasahara, Y. Mizukami, R. Katsumata, Y. Tsuruhara, T. Terashima, H. Ikeda, M. A. Tanatar, H. Kitano, N. Salovich, R. W. Giannetta, P. Walmsley, A. Carrington, R. Prozorov, and Y. Matsuda, Science **336**, 1554 (2012).

[142] M. J. Eom, S. W. Na, C. Hoch, R. K. Kremer, and J. S. Kim, Phys. Rev. B **85**, 024536 (2012).

[143] D. J. Singh, Phys. Rev. B **78**, 094511 (2008).

[144] T. Shibauchi, A. Carrington, and Y. Matsuda, Annual Review of Condensed Matter Physics **5**, 113 (2014).

[145] S. V. Borisenko, V. B. Zabolotnyy, A. A. Kordyuk, D. V. Evtushinsky, T. K. Kim, E. Carleschi, B. P. Doyle, R. Fittipaldi, M. Cuoco, A. Vecchione, and H. Berger, Journal of Visualized Experiments , e50129 (2012).

[146] A. Damascelli, Z. Hussain, and Z.-X. Shen, Rev. Mod. Phys. **75**, 473 (2003).

[147] S. E. Sebastian, ArXiv e-prints (2012), arXiv:1208.5862 .

[148] C. de la Cruz, Q. Huang, J. W. Lynn, J. Li, W. R. II, J. L. Zarestky, H. A. Mook, G. F. Chen, J. L. Luo, N. L. Wang, and P. Dai, Nature **453**, 899 (2008).

[149] A. I. Goldman, D. N. Argyriou, B. Ouladdiaf, T. Chatterji, A. Kreyssig, S. Nandi, N. Ni, S. L. Bud'ko, P. C. Canfield, and R. J. McQueeney, Phys. Rev. B **78**, 100506 (2008).

[150] Q. Huang, Y. Qiu, W. Bao, M. A. Green, J. W. Lynn, Y. C. Gasparovic, T. Wu, G. Wu, and X. H. Chen, Phys. Rev. Lett. **101**, 257003 (2008).

[151] J. Zhao, W. Ratcliff, J. W. Lynn, G. F. Chen, J. L. Luo, N. L. Wang, J. Hu, and P. Dai, Phys. Rev. B **78**, 140504 (2008).

[152] K. Kaneko, A. Hoser, N. Caroca-Canales, A. Jesche, C. Krellner, O. Stockert, and C. Geibel, Phys. Rev. B **78**, 212502 (2008).

[153] K. Matan, R. Morinaga, K. Iida, and T. J. Sato, Phys. Rev. B **79**, 054526 (2009).

[154] Y. Xiao, Y. Su, R. Mittal, T. Chatterji, T. Hansen, C. M. N. Kumar, S. Matsuishi, H. Hosono, and T. Brueckel, Phys. Rev. B **79**, 060504 (2009).

[155] K. Kitagawa, N. Katayama, K. Ohgushi, M. Yoshida, and M. Takigawa, J. Phys. Soc. Jpn. **77**, 114709 (2008).

[156] K. Kitagawa, N. Katayama, K. Ohgushi, and M. Takigawa, J. Phys. Soc. Jpn. **78**, 063706 (2009).

[157] A. A. Aczel, E. Baggio-Saitovitch, S. L. Budko, P. C. Canfield, J. P. Carlo, G. F. Chen, P. Dai, T. Goko, W. Z. Hu, G. M. Luke, J. L. Luo, N. Ni, D. R. Sanchez-Candela, F. F. Tafti, N. L. Wang, T. J. Williams, W. Yu, and Y. J. Uemura, Phys. Rev. B **78**, 214503 (2008).

[158] A. Jesche, N. Caroca-Canales, H. Rosner, H. Borrmann, A. Ormeci, D. Kasinathan, H. H. Klauss, H. Luetkens, R. Khasanov, A. Amato, A. Hoser, K. Kaneko, C. Krellner, and C. Geibel, Phys. Rev. B **78**, 180504 (2008).

[159] T. Goko, A. A. Aczel, E. Baggio-Saitovitch, S. L. Bud'ko, P. C. Canfield, J. P. Carlo, G. F. Chen, P. Dai, A. C. Hamann, W. Z. Hu, H. Kageyama, G. M. Luke, J. L. Luo, B. Nachumi, N. Ni, D. Reznik, D. R. Sanchez-Candela, A. T. Savici, K. J. Sikes, N. L. Wang, C. R. Wiebe, T. J. Williams, T. Yamamoto, W. Yu, and Y. J. Uemura, Phys. Rev. B **80**, 024508 (2009).

[160] I. I. Mazin, D. J. Singh, M. D. Johannes, and M. H. Du, Phys. Rev. Lett. **101**, 057003 (2008).

[161] D. Singh, Physica C: Superconductivity **469**, 418 (2009).

[162] S. Blundell, *Magnetism in Condensed Matter* (Oxford University Press, 2001).

[163] E. Dagotto, Rev. Mod. Phys. **66**, 763 (1994).

[164] I. Mazin and J. Schmalian, Physica C: Superconductivity **469**, 614 (2009).

[165] E. Fawcett, Rev. Mod. Phys. **60**, 209 (1988).

[166] A. N. Yaresko, G.-Q. Liu, V. N. Antonov, and O. K. Andersen, Phys. Rev. B **79**, 144421 (2009).

[167] Z. P. Yin, K. Haule, and G. Kotliar, Nat Mater **10**, 932 (2011).

[168] J. W. Lynn and P. Dai, Physica C: Superconductivity **469**, 469 (2009).

[169] A. Charnukha, A. Cvitkovic, T. Prokscha, D. Pröpper, N. Ocelic, A. Suter, Z. Salman, E. Morenzoni, J. Deisenhofer, V. Tsurkan, A. Loidl, B. Keimer, and A. V. Boris, Phys. Rev. Lett. **109**, 017003 (2012).

[170] J. P. Carlo, Y. J. Uemura, T. Goko, G. J. MacDougall, J. A. Rodriguez, W. Yu, G. M. Luke, P. Dai, N. Shannon, S. Miyasaka, S. Suzuki, S. Tajima, G. F. Chen, W. Z. Hu, J. L. Luo, and N. L. Wang, Phys. Rev. Lett. **102**, 087001 (2009).

[171] S. V. Borisenko, V. B. Zabolotnyy, D. V. Evtushinsky, T. K. Kim, I. V. Morozov, A. N. Yaresko, A. A. Kordyuk, G. Behr, A. Vasiliev, R. Follath, and B. Büchner, Phys. Rev. Lett. **105**, 067002 (2010).

[172] H. Gretarsson, A. Lupascu, J. Kim, D. Casa, T. Gog, W. Wu, S. R. Julian, Z. J. Xu, J. S. Wen, G. D. Gu, R. H. Yuan, Z. G. Chen, N.-L. Wang, S. Khim, K. H. Kim, M. Ishikado, I. Jarrige, S. Shamoto, J.-H. Chu, I. R. Fisher, and Y.-J. Kim, Phys. Rev. B **84**, 100509 (2011).

[173] W. Z. Hu, J. Dong, G. Li, Z. Li, P. Zheng, G. F. Chen, J. L. Luo, and N. L. Wang, Phys. Rev. Lett. **101**, 257005 (2008).

[174] D. Wu, N. Barišić, P. Kallina, A. Faridian, B. Gorshunov, N. Drichko, L. J. Li, X. Lin, G. H. Cao, Z. A. Xu, N. L. Wang, and M. Dressel, Phys. Rev. B **81**, 100512 (2010).

[175] M. Nakajima, S. Ishida, K. Kihou, Y. Tomioka, T. Ito, Y. Yoshida, C. H. Lee, H. Kito, A. Iyo, H. Eisaki, K. M. Kojima, and S. Uchida, Phys. Rev. B **81**, 104528 (2010).

[176] H. Okamura, K. Shoji, K. Miyata, H. Sugawara, T. Moriwaki, and Y. Ikemoto, J. Phys. Soc. Jpn. **82**, 074720 (2013).

[177] L. Boeri, O. V. Dolgov, and A. A. Golubov, Phys. Rev. Lett. **101**, 026403 (2008).

[178] A. Subedi, L. Zhang, D. J. Singh, and M. H. Du, Phys. Rev. B **78**, 134514 (2008).

[179] R. H. Liu, T. Wu, G. Wu, H. Chen, X. F. Wang, Y. L. Xie, J. J. Ying, Y. J. Yan, Q. J. Li, B. C. Shi, W. S. Chu, Z. Y. Wu, and X. H. Chen, Nature **459**, 64 (2009).

[180] P. M. Shirage, K. Miyazawa, K. Kihou, H. Kito, Y. Yoshida, Y. Tanaka, H. Eisaki, and A. Iyo, Phys. Rev. Lett. **105**, 037004 (2010).

[181] H.-J. Grafe, D. Paar, G. Lang, N. J. Curro, G. Behr, J. Werner, J. Hamann-Borrero, C. Hess, N. Leps, R. Klingeler, and B. Büchner, Phys. Rev. Lett. **101**, 047003 (2008).

[182] K. Matano, Z. A. Ren, X. L. Dong, L. L. Sun, Z. X. Zhao, and G. Zheng, EPL (Europhysics Letters) **83**, 57001 (2008).

[183] F. Ning, K. Ahilan, T. Imai, A. S. Sefat, R. Jin, M. A. McGuire, B. C. Sales, and D. Mandrus, J. Phys. Soc. Jpn. **77**, 103705 (2008).

[184] K. H. Bennemann and J. B. Ketterson, *Superconductivity: Volume 1: Conventional and Unconventional Superconductors* (Springer, 2008).

[185] A. D. Christianson, E. A. Goremychkin, R. Osborn, S. Rosenkranz, M. D. Lumsden, C. D. Malliakas, I. S. Todorov, H. Claus, D. Y. Chung, M. G. Kanatzidis, R. I. Bewley, and T. Guidi, Nature **456**, 930 (2008).

[186] D. S. Inosov, J. T. Park, P. Bourges, D. L. Sun, Y. Sidis, A. Schneidewind, K. Hradil, D. Haug, C. T. Lin, B. Keimer, and V. Hinkov, Nat Phys **6**, 178 (2010).

[187] J. T. Park, G. Friemel, Y. Li, J.-H. Kim, V. Tsurkan, J. Deisenhofer, H.-A. Krug von Nidda, A. Loidl, A. Ivanov, B. Keimer, and D. S. Inosov, Phys. Rev. Lett. **107**, 177005 (2011).

[188] D. S. Inosov, J. T. Park, A. Charnukha, Y. Li, A. V. Boris, B. Keimer, and V. Hinkov, Phys. Rev. B **83**, 214520 (2011).

[189] X. Qiu, S. Y. Zhou, H. Zhang, B. Y. Pan, X. C. Hong, Y. F. Dai, M. J. Eom, J. S. Kim, Z. R. Ye, Y. Zhang, D. L. Feng, and S. Y. Li, Phys. Rev. X **2**, 011010 (2012).

[190] Y. Zhang, Z. R. Ye, Q. Q. Ge, F. Chen, J. Jiang, M. Xu, B. P. Xie, and D. L. Feng, Nat Phys **8**, 371 (2012).

[191] D. V. Evtushinsky, V. B. Zabolotnyy, T. K. Kim, A. A. Kordyuk, A. N. Yaresko, J. Maletz, S. Aswartham, S. Wurmehl, A. V. Boris, D. L. Sun, C. T. Lin, B. Shen, H. H. Wen, A. Varykhalov, R. Follath, B. Büchner, and S. V. Borisenko, Phys. Rev. B **89**, 064514 (2014).

[192] A. Chubukov, Annual Review of Condensed Matter Physics **3**, 57 (2012).

[193] A. A. Golubov and I. I. Mazin, Applied Physics Letters **102**, 032601 (2013).

[194] A. V. Burmistrova and I. A. Devyatov, ArXiv e-prints (2013), arXiv:1312.5930 .

[195] P. C. Canfield, S. L. Bud'ko, N. Ni, J. Q. Yan, and A. Kracher, Phys. Rev. B **80**, 060501 (2009).

[196] S. Kasahara, T. Shibauchi, K. Hashimoto, K. Ikada, S. Tonegawa, R. Okazaki, H. Shishido, H. Ikeda, H. Takeya, K. Hirata, T. Terashima, and Y. Matsuda,

Phys. Rev. B **81**, 184519 (2010).

[197] S. K. Kim, M. S. Torikachvili, E. Colombier, A. Thaler, S. L. Bud'ko, and P. C. Canfield, Phys. Rev. B **84**, 134525 (2011).

[198] M. G. Kim, J. Soh, J. Lang, M. P. M. Dean, A. Thaler, S. L. Bud'ko, P. C. Canfield, E. Bourret-Courchesne, A. Kreyssig, A. I. Goldman, and R. J. Birgeneau, Phys. Rev. B **88**, 014424 (2013).

[199] M. Neupane, P. Richard, Y.-M. Xu, K. Nakayama, T. Sato, T. Takahashi, A. V. Federov, G. Xu, X. Dai, Z. Fang, Z. Wang, G.-F. Chen, N.-L. Wang, H.-H. Wen, and H. Ding, Phys. Rev. B **83**, 094522 (2011).

[200] L. Zhang and D. J. Singh, Phys. Rev. B **79**, 174530 (2009).

[201] N. Xu, T. Qian, P. Richard, Y.-B. Shi, X.-P. Wang, P. Zhang, Y.-B. Huang, Y.-M. Xu, H. Miao, G. Xu, G.-F. Xuan, W.-H. Jiao, Z.-A. Xu, G.-H. Cao, and H. Ding, Phys. Rev. B **86**, 064505 (2012).

[202] R. S. Dhaka, C. Liu, R. M. Fernandes, R. Jiang, C. P. Strehlow, T. Kondo, A. Thaler, J. Schmalian, S. L. Bud'ko, P. C. Canfield, and A. Kaminski, Phys. Rev. Lett. **107**, 267002 (2011).

[203] V. Brouet, F. Rullier-Albenque, M. Marsi, B. Mansart, M. Aichhorn, S. Biermann, J. Faure, L. Perfetti, A. Taleb-Ibrahimi, P. Le Fèvre, F. Bertran, A. Forget, and D. Colson, Phys. Rev. Lett. **105**, 087001 (2010).

[204] H. Shishido, A. F. Bangura, A. I. Coldea, S. Tonegawa, K. Hashimoto, S. Kasahara, P. M. C. Rourke, H. Ikeda, T. Terashima, R. Settai, Y. Ōnuki, D. Vignolles, C. Proust, B. Vignolle, A. McCollam, Y. Matsuda, T. Shibauchi, and A. Carrington, Phys. Rev. Lett. **104**, 057008 (2010).

[205] L. Fang, H. Luo, P. Cheng, Z. Wang, Y. Jia, G. Mu, B. Shen, I. I. Mazin, L. Shan, C. Ren, and H.-H. Wen, Phys. Rev. B **80**, 140508 (2009).

[206] H. Kontani, Reports on Progress in Physics **71**, 026501 (2008).

[207] A. F. Kemper, M. M. Korshunov, T. P. Devereaux, J. N. Fry, H.-P. Cheng, and P. J. Hirschfeld, Phys. Rev. B **83**, 184516 (2011).

[208] Y. Laplace, J. Bobroff, V. Brouet, G. Collin, F. Rullier-Albenque, D. Colson, and A. Forget, Phys. Rev. B **86**, 020510 (2012).

[209] J. Zhao, C. R. Rotundu, K. Marty, M. Matsuda, Y. Zhao, C. Setty, E. Bourret-Courchesne, J. Hu, and R. J. Birgeneau, Phys. Rev. Lett. **110**, 147003 (2013).

[210] D. N. Basov and T. Timusk, Rev. Mod. Phys. **77**, 721 (2005).

[211] D. N. Basov, R. D. Averitt, D. van der Marel, M. Dressel, and K. Haule, Rev. Mod. Phys. **83**, 471 (2011).

[212] A. V. Boris, N. N. Kovaleva, O. V. Dolgov, T. Holden, C. T. Lin, B. Keimer, and C. Bernhard, Science **304**, 708 (2004).

[213] A. Charnukha, O. V. Dolgov, A. A. Golubov, Y. Matiks, D. L. Sun, C. T. Lin, B. Keimer, and A. V. Boris, Phys. Rev. B **84**, 174511 (2011).

[214] M. Nakajima, T. Tanaka, S. Ishida, K. Kihou, C. H. Lee, A. Iyo, T. Kakeshita, H. Eisaki, and S. Uchida, Phys. Rev. B **88**, 094501 (2013).

[215] G. Grimvall, *The Electron-Phonon Interaction in Metals* (North-Holland, Amsterdam, 1981).

[216] J. Neve, B. Sundqvist, and O. Rapp, Phys. Rev. B **28**, 629 (1983).

[217] Z. R. Ye, Y. Zhang, F. Chen, M. Xu, Q. Q. Ge, J. Jiang, B. P. Xie, and D. L. Feng, Phys. Rev. B **86**, 035136 (2012).

[218] D. H. Lu, M. Yi, S.-K. Mo, A. S. Erickson, J. Analytis, J.-H. Chu, D. J. Singh, Z. Hussain, T. H. Geballe, I. R. Fisher, and Z.-X. Shen, Nature **455**, 81 (2008).

[219] M. Yi, D. H. Lu, J. G. Analytis, J.-H. Chu, S.-K. Mo, R.-H. He, R. G. Moore, X. J. Zhou, G. F. Chen, J. L. Luo, N. L. Wang, Z. Hussain, D. J. Singh, I. R. Fisher, and Z.-X. Shen, Phys. Rev. B **80**, 024515 (2009).

[220] H. Liu, G. F. Chen, W. Zhang, L. Zhao, G. Liu, T.-L. Xia, X. Jia, D. Mu, S. Liu, S. He, Y. Peng, J. He, Z. Chen, X. Dong, J. Zhang, G. Wang, Y. Zhu, Z. Xu, C. Chen, and X. J. Zhou, Phys. Rev. Lett. **105**, 027001 (2010).

[221] Y. Xia, D. Qian, L. Wray, D. Hsieh, G. F. Chen, J. L. Luo, N. L. Wang, and M. Z. Hasan, Phys. Rev. Lett. **103**, 037002 (2009).

[222] A. A. Schafgans, S. J. Moon, B. C. Pursley, A. D. LaForge, M. M. Qazilbash, A. S. Sefat, D. Mandrus, K. Haule, G. Kotliar, and D. N. Basov, Phys. Rev. Lett. **108**, 147002 (2012).

[223] L. Stojchevska, P. Kusar, T. Mertelj, V. V. Kabanov, X. Lin, G. H. Cao, Z. A. Xu, and D. Mihailovic, Phys. Rev. B **82**, 012505 (2010).

[224] M. Nakajima, T. Liang, S. Ishida, Y. Tomioka, K. Kihou, C. H. Lee, A. Iyo, H. Eisaki, T. Kakeshita, T. Ito, and S. Uchida, Proceedings of the National Academy of Sciences **108**, 12238 (2011).

[225] M. Nakajima, S. Ishida, Y. Tomioka, K. Kihou, C. H. Lee, A. Iyo, T. Ito, T. Kakeshita, H. Eisaki, and S. Uchida, Phys. Rev. Lett. **109**, 217003 (2012).

[226] P. Marsik, C. N. Wang, M. Rössle, M. Yazdi-Rizi, R. Schuster, K. W. Kim, A. Dubroka, D. Munzar, T. Wolf, X. H. Chen, and C. Bernhard, Phys. Rev. B **88**, 180508 (2013).

[227] L. Harnagea, S. Singh, G. Friemel, N. Leps, D. Bombor, M. Abdel-Hafiez, A. U. B. Wolter, C. Hess, R. Klingeler, G. Behr, S. Wurmehl, and B. Büchner, Phys. Rev. B **83**, 094523 (2011).

[228] S. Ran, S. L. Bud'ko, W. E. Straszheim, J. Soh, M. G. Kim, A. Kreyssig, A. I. Goldman, and P. C. Canfield, Phys. Rev. B **85**, 224528 (2012).

[229] T.-M. Chuang, M. P. Allan, J. Lee, Y. Xie, N. Ni, S. L. Bud'ko, G. S. Boebinger, P. C. Canfield, and J. C. Davis, Science **327**, 181 (2010).

[230] M. P. Allan, T.-M. Chuang, F. Massee, Y. Xie, N. Ni, S. L. Bud'ko, G. S. Boebinger, Q. Wang, D. S. Dessau, P. C. Canfield, M. S. Golden, and J. C. Davis, Nat Phys **9**, 220 (2013).

[231] J.-H. Chu, J. G. Analytis, K. De Greve, P. L. McMahon, Z. Islam, Y. Yamamoto, and I. R. Fisher, Science **329**, 824 (2010).

[232] J.-H. Chu, H.-H. Kuo, J. G. Analytis, and I. R. Fisher, Science **337**, 710 (2012).

[233] S. Ishida, M. Nakajima, T. Liang, K. Kihou, C. H. Lee, A. Iyo, H. Eisaki, T. Kakeshita, Y. Tomioka, T. Ito, and S. Uchida, Phys. Rev. Lett. **110**, 207001 (2013).

[234] M. Nakajima, S. Ishida, K. Kihou, Y. Tomioka, T. Ito, C. Lee, H. Kito, A. Iyo, H. Eisaki, K. Kojima, and S. Uchida, Physica C: Superconductivity **470, Supplement 1**, S326 (2010).

[235] W. Hu, Q. Zhang, and N. Wang, Physica C: Superconductivity **469**, 545 (2009).

[236] D. Wu, N. Barišić, N. Drichko, S. Kaiser, A. Faridian, M. Dressel, S. Jiang, Z. Ren, L. J. Li, G. H. Cao, Z. A. Xu, H. S. Jeevan, and P. Gegenwart, Phys. Rev. B **79**, 155103 (2009).

[237] A. A. Schafgans, B. C. Pursley, A. D. LaForge, A. S. Sefat, D. Mandrus, and D. N. Basov, Phys. Rev. B **84**, 052501 (2011).

[238] B. Cheng, B. F. Hu, R. Y. Chen, G. Xu, P. Zheng, J. L. Luo, and N. L. Wang, Phys. Rev. B **86**, 134503 (2012).

[239] G. Li, W. Z. Hu, J. Dong, Z. Li, P. Zheng, G. F. Chen, J. L. Luo, and N. L. Wang, Phys. Rev. Lett. **101**, 107004 (2008).

[240] B. Gorshunov, D. Wu, A. A. Voronkov, P. Kallina, K. Iida, S. Haindl, F. Kurth, L. Schultz, B. Holzapfel, and M. Dressel, Phys. Rev. B **81**, 060509 (2010).

[241] T. Fischer, A. V. Pronin, J. Wosnitza, K. Iida, F. Kurth, S. Haindl, L. Schultz, B. Holzapfel, and E. Schachinger, Phys. Rev. B **82**, 224507 (2010).

[242] A. Lucarelli, A. Dusza, F. Pfuner, P. Lerch, J. G. Analytis, J.-H. Chu, I. R. Fisher, and L. Degiorgi, New Journal of Physics **12**, 073036 (2010).

[243] J. J. Tu, J. Li, W. Liu, A. Punnoose, Y. Gong, Y. H. Ren, L. J. Li, G. H. Cao, Z. A. Xu, and C. C. Homes, Phys. Rev. B **82**, 174509 (2010).

[244] N. Barišić, D. Wu, M. Dressel, L. J. Li, G. H. Cao, and Z. A. Xu, Phys. Rev. B **82**, 054518 (2010).

[245] D. Wu, G. Chanda, H. S. Jeevan, P. Gegenwart, and M. Dressel, Phys. Rev. B **83**, 100503 (2011).

[246] S. J. Moon, A. A. Schafgans, S. Kasahara, T. Shibauchi, T. Terashima, Y. Matsuda, M. A. Tanatar, R. Prozorov, A. Thaler, P. C. Canfield, A. S. Sefat, D. Mandrus, and D. N. Basov, Phys. Rev. Lett. **109**, 027006 (2012).

[247] M. Nakajima, S. Ishida, T. Tanaka, K. Kihou, Y. Tomioka, T. Saito, C. H. Lee, H. Fukazawa, Y. Kohori, T. Kakeshita, A. Iyo, T. Ito, H. Eisaki, and S. Uchida, ArXiv e-prints (2013), arXiv:1308.6133 .

[248] E. J. Nicol and J. P. Carbotte, Phys. Rev. B **71**, 054501 (2005).

[249] V. G. Kogan, C. Martin, and R. Prozorov, Phys. Rev. B **80**, 014507 (2009).

[250] Y. Ponomarev, S. Kuzmichev, M. Mikheev, M. Sudakova, S. Tchesnokov, T. Shanygina, O. Volkova, A. Vasiliev, and T. Wolf, Journal of Experimental and Theoretical Physics **113**, 459 (2011).

[251] R. Khasanov, M. Bendele, A. Amato, K. Conder, H. Keller, H.-H. Klauss, H. Luetkens, and E. Pomjakushina, Phys. Rev. Lett. **104**, 087004 (2010).

[252] Y. Ponomarev, S. Kuzmichev, T. Kuzmicheva, M. Mikheev, M. Sudakova, S. Tchesnokov, O. Volkova, A. Vasiliev, V. Pudalov, A. Sadakov, A. Usol'tsev, T. Wolf, E. Khlybov, and L. Kulikova, Journal of Superconductivity and Novel Magnetism **26**, 2867 (2013).

[253] G. Sun, D. Sun, M. Konuma, P. Popovich, A. Boris, J. Peng, K.-Y. Choi, P. Lemmens, and C. Lin, Journal of Superconductivity and Novel Magnetism **24**, 1773 (2011).

[254] S. Ran, S. L. Bud'ko, D. K. Pratt, A. Kreyssig, M. G. Kim, M. J. Kramer, D. H. Ryan, W. N. Rowan-Weetaluktuk, Y. Furukawa, B. Roy, A. I. Goldman, and

P. C. Canfield, Phys. Rev. B **83**, 144517 (2011).

[255] F. Hardy, P. Adelmann, T. Wolf, H. v. Löhneysen, and C. Meingast, Phys. Rev. Lett. **102**, 187004 (2009).

[256] O. V. Dolgov and M. L. Kulić, Phys. Rev. B **66**, 134510 (2002).

[257] C. Bernhard, T. Holden, A. V. Boris, N. N. Kovaleva, A. V. Pimenov, J. Humlíček, C. Ulrich, C. T. Lin, and J. L. Tallon, Phys. Rev. B **69**, 052502 (2004).

[258] D. N. Basov, A. V. Puchkov, R. A. Hughes, T. Strach, J. Preston, T. Timusk, D. A. Bonn, R. Liang, and W. N. Hardy, Phys. Rev. B **49**, 12165 (1994).

[259] H. K. Ng, M. Capizzi, G. A. Thomas, R. N. Bhatt, and A. C. Gossard, Phys. Rev. B **33**, 7329 (1986).

[260] A. Gold, S. J. Allen, B. A. Wilson, and D. C. Tsui, Phys. Rev. B **25**, 3519 (1982).

[261] H. F. Jang, G. Cripps, and T. Timusk, Phys. Rev. B **41**, 5152 (1990).

[262] S. J. Moon, A. A. Schafgans, M. A. Tanatar, R. Prozorov, A. Thaler, P. C. Canfield, A. S. Sefat, D. Mandrus, and D. N. Basov, Phys. Rev. Lett. **110**, 097003 (2013).

[263] R. Mittal, S. Rols, M. Zbiri, Y. Su, H. Schober, S. L. Chaplot, M. Johnson, M. Tegel, T. Chatterji, S. Matsuishi, H. Hosono, D. Johrendt, and T. Brueckel, Phys. Rev. B **79**, 144516 (2009).

[264] S.-L. Drechsler, F. Roth, M. Grobosch, R. Schuster, K. Koepernik, H. Rosner, G. Behr, M. Rotter, D. Johrendt, B. Büchner, and M. Knupfer, Physica C: Superconductivity **470, Supplement 1**, S332 (2010).

Acknowledgements

First of all, I want to thank Prof. Bernhard Keimer for taking and supporting me as a doctoral student and giving me the opportunity to freely follow my research projects in his group at the Max-Planck-Institute for Solid State Research in Stuttgart and present my results at different workshops and conferences. I would also like to thank Prof. Tilman Pfau for being the co-reporter on my thesis.

I am very grateful to my direct supervisor Alexander Boris for constant support and many helpful discussions on both physics and experimental issues. He introduced me to the technique of spectroscopic ellipsometry and I benefited a lot from his long experience on optical spectroscopy of many types of correlated electron systems.

Thanks to my colleagues of our optical spectroscopy group for helping hands and lots of discussions: Yulia Matiks, Timofei Larkin, Ayman Akil and in particular to my colleague and friend Aliaksei Charnukha with whom I spent many day and night shifts on beamtimes in Karlsruhe and Brookhaven which resulted in many successful projects – however, implementing a reliable automation of the sample temperature control might have been our most useful (at least healthiest) idea.

Without the high quality single crystals from Tomohiro Takayama and Akiyo Matsumoto from Prof. Hidenori Takagi's group, now in Stuttgart, Prof. Jun Sung Kim and Man Jin Eom from Postech, Korea, the in-house crystal growth service group under supervision of Chengtian Lin and Thomas Wolf from KIT in Karlsruhe, there would not have been anything to explore.

As obvious from this work the rich input from a theoretical point of view can tremendously boost our understanding of experimental results. Thanks to Alexander Yaresko and Marc Höppner for their extensive calculations, fruitful discussions about their outcomes and patiently answering all my questions.

Never touch a running system but sometimes (actually quite often) you have to: thanks to Benjamin Bruha and Heiko Uhlig for quick and straightforward technical support, usually on short notice. Working at synchrotron facilities involves many local contacts: thanks to Yves-Laurent Mathis, Michael Süpfle and Johannes Steinmann for support at the ANKA synchrotron in Karlsruhe and Prof. Andrei Sirenko, Taras Stanislavchuk and Larry Carr for having us at their new ellipsometry setup at the NSLS at the Brookhaven National Laboratory several times.

I would also like to thank the entire Keimer department not only for scientific support but an enjoyable atmosphere and numerous discussions with lots of after lunch coffee and dark chocolate – in particular it was a great pleasure to share the office with Meng Wu and Yi Lu.

I am deeply grateful to my family and friends for their continuous support and encouragement throughout the years.

The final line of this thesis I dedicate to my wife Katrin – my companion and love.